Title
Investigation of Molecular Metal Complexes for Catalytic Nitrogen Evolution Reaction

Author
Jacob, Samuel

Publication Date
2021

UNIVERSITY OF CALIFORNIA

Santa Barbara

Investigation of Molecular Metal Complexes for Catalytic Nitrogen Evolution Reaction

A dissertation submitted in partial satisfaction of the

requirements for the degree Doctor of Philosophy

in Chemistry

by

Samuel Isaac Jacob

Committee in charge:

Professor Gabriel Ménard, Chair

Professor Trevor Hayton

Professor Lior Sepunaru

Professor Mahdi Abu-Omar

December 2021

The dissertation of Samuel Isaac Jacob is approved.

Mahdi Abu-Omar

Lior Sepunaru

Trevor Hayton

Gabriel Ménard, Committee Chair

December 2021

Investigation of Molecular Metal Complexes for Catalytic Nitrogen Evolution Reaction

by

Samuel Isaac Jacob

ACKNOWLEDGEMENTS

First, I would like to thank my supervisor Professor Gabriel Menard. Gab, you let me do whatever I wanted over these years. Even when we disagreed, you still let me pursue what I thought was worth pursuing, although most of the time you were not aware. Your door was always open, and your kindness was valuable. I felt comfortable about voicing my problems with my ADHD with you and while I don't think you were able to fully understand my challenges, there are few people that I can say that about. Thank you.

Going back to my roots, I must whole heartedly acknowledge the graduate students who helped raise me as an undergrad during my time at ASU. Anna Beiler, Diana Khusnutdinova and Brian Wadsworth, I don't know how to properly express how grateful I am to you three for cheering me on and supporting me. The three of you are some of the most important people I've met in my life. Thank you. Next, I would like to acknowledge my friends from Dr. Skibo's organic chemistry class. Mac, Evan, Brandon, Corbin, Gamu, Huang, Matt, and Tony. I love you guys.

I've had the opportunity to meet incredible people during my time at UCSB. Maddy and Anthony, our time together here has been the longest and I'm happy that we were in the same cohort and joined the Gab lab together. Anthony, I will always think fondly of our late nights in the lab. You are the most skilled synthetic chemist I know and an invaluable friend. I look forward to seeing where you get hired as a professor and of course. Maddy, I have always envied your intelligence, humor, and compassion towards others. You were invaluable both as a classmate and lab mate. Someday I hope we will become closer friends. Camden and Tim, you guys are phenomenal and were incredibly supportive as senior lab mates and especially as friends. I hope we can continue our friendship for the years to come.

I would like to specially acknowledge my protegee, Arun Chakraborty. You are possibly the smartest and most genuine person I have ever interacted with. I can only hope that you learned half as much from me as I learned from you. Half of this thesis would not exist if not for you. I'm confident that we will be friends for the rest of our lives. Maxx, thank you for putting up with me all the years we shared a fumehood and I appreciated all our morning conversations before everyone else arrived in lab. Shannon, it has been an absolute pleasure becoming closer friends with you over the years, watching you develop your skills as a chemist, and handling so many leadership responsibilities. Zongheng, you always have a positive attitude and I enjoyed chatting with you at the end of each day. Thank for all the karaoke nights and volleyball. And of course Jiaxiang Chu, I am a truly lucky person to have worked alongside you during your postdoc in our lab. I am glad to have you as a friend.

Thank you to all the facility managers and specialists at UCSB, especially Dr. Guang Wu, Dr. Hongjun, Cabe Fletcher, Adrian Shelor, Richard Bock, and Roger Green. None of this research would have been possible without all of you here. You have my utmost gratitude. I also want to thank the members of committee for all the guidance, discussions, and especially the friendly interactions we shared in the hallways during the past years.

During my time at UCSB I had the opportunity to discover my passion for volleyball. I would like to thank Ljube, Jason, Masa, Tim, Jake, Brad, Zongheng, and Pavel for being wonderful teammates when we played competitively and for fun. I want to thank everyone who played volleyball with me during the COVID lockdown and afterwards. Sorry but there are too many to list off each person by name. The Saturday/Sunday morning and Friday afternoon volleyball games we had was some of the most fun I've had in Santa Barbara. You all allowed me to enjoy my new favorite sport and I'll think about our quality times as I continue to play volleyball the many years ahead of me. I want to give a special acknowledgement to my amazing friend Ljube who was an amazing friend that never stopped supporting me and is someone who I can rely on for anything. You are an amazing person.

I would like to acknowledge my parents. Mom, your insurmountable love, and support has pushed me forward all my life. Dad, it is your love of science and learning that made me want to pursue the life of a scientist. I would like to acknowledge my late professor and first mentor, Dr. Edward Bernard Skibo. It was after my candidacy here at UCSB that I finally learned that Dr. Skibo did his postdoctoral studies here at UCSB with T.C. Bruice. Thank you for making learning fun for me and I'm glad we could share a similar experience. Rest in peace Dr. Skibo.

And finally, I would like to acknowledge mi amor, Ana Parejo. Your love and support during these last few months made the difficult process of writing my thesis a truly great experience. I love you and I look forward to the many adventures ahead of us.

Samuel Isaac Jacob

Santa Barbara, CA · (480) 201-9998 · sijacob36@gmail.com
https://www.linkedin.com/in/samuel-jacob-33b7471b7/

Education

Ph.D. in Chemistry | University of California, Santa Barbara (UCSB) 2021
B.S. in Biochemistry, Magna cum laude | Arizona State University (ASU) 2016

Publications

1. **Jacob, S. I.**; Douair, I.; Wu, G.; Maron, L.; Ménard, G.* "A Tetranuclear Nickel Cluster Isolated in Multiple High-Valent States." *Chem. Commun.*, **2020**. 56, 8182-8185.
2. Khusnutdinova, D.; Beiler, A. M.; Wadsworth, B. L.; **Jacob, S. I.**; Moore, G. F.* "Metalloporphyrin-modified semiconductors for solar fuel production." *Chem. Sci.* **2017**, 8, 253-259.
3. Wadsworth, B. L.; Beiler, A. M.; Khusnutdinova, D.; **Jacob, S. I**; Moore, G. F.* "Electrocatalytic and Optical Properties of Cobaloxime Catalysts Immobilized at a Surface-Grafted Polymer Interface." *ACS Catal.* **2016**, 6, 8048-8057.
4. Beiler, A. M.; Khusnutdinova, D.; **Jacob, S. I.**; Moore, G.F.* "Chemistry at the Interface: PolymerFunctionalized GaP Semiconductors for Solar Hydrogen Production." *Ind. Eng. Chem. Res.*, **2016**, 55, 5306- 5314.
5. Beiler, A. M.; Khusnutdinova, D.; **Jacob, S. I.**; Moore, G.F.* "Solar Hydrogen Production Using Molecular Catalysts Immobilized on Gallium Phosphide." *ACS Appl. Mater. Interfaces*, **2016**, 8, 10038-10047.

Presentations

1. **Jacob, S. I.**; Ménard, G.* "Taming a High-Valent Tetra-Nickel Cluster for Catalytic Electrochemical Ammonia Oxidation." *The Chemical Student Seminar Series.* University of California, Santa Barbara. November 2019. (Oral presentation).
2. **Jacob, S. I.**; Ménard, G.* "Taming a High-Valent Tetra-Nickel Cluster for Small Molecule Reactivity." *ACS National Meeting and Expo.* San Diego, CA. Nov 2019. (Oral presentation).
3. **Jacob, S. I.**; Ménard, G.* "Taming a High-Valent Tetranuclear Nickel Cluster." *The UC Chemical Symposium.* Lake Arrowhead Conference Center. March 2019. (Poster presentation). ***Winner of Best Poster***
4. **Jacob, S. I.**; Ménard, G.* "Synthesis and Characterization of a Tetra-Nickel Cluster Capable of Stabilizing Four Nickel(III) Centers." *Southern California Organometallics Seminar.* University of Southern California. February 2019. (Oral presentation).

5. **Jacob, S. I.**; Ménard, G.* "Moving Towards Bimetallic Ammonia Oxidation: Pacman Eating up the Progress." *Southern California Organometallics Seminar*. University of California, Los Angeles. May 2018. (Oral presentation).

Teaching Experience

- Teaching Assistant –
  - Analytical/Inorganic Chemistry Laboratories 2017-2018, 2021
  - General Chemistry Laboratories 2016-2017

Honors/Awards

Chair's Fellowship	2021
Dalton Transactions Award for **Best Poster**	2019
Robert H. DeWolfe Distinguished Teaching Award	2019
Doctoral Student Travel Grant	2019
Mellichamp Academic Initiative in Sustainability Fellowship	2019
Outstanding Service to the Department Award (x2)	2016-2017
Student Affiliated ACS Organic Achievement Award	2015
Undergraduate Student Enrichment Program	2015

Outreach

Science Career Outreach Project Experiment (SCOPE) Aug 2016 – 2021

- SCOPE is an outreach program with the purpose of raising enthusiasm in science for high school students, informing them of the opportunities in studying science in graduate school, and improving diversity in the STEM fields.

ABSTRACT

Investigation of Molecular Metal Complexes for Catalytic Nitrogen Evolution Reaction

by

Samuel Isaac Jacob

With the growing threat of climate change, it is important that we rapidly transition from fossil fuels to renewable energy use. Renewable energy technologies have developed considerably making them cost competitive with fossil fuels; however, the key issue inhibiting our transition is storage. The United States has a 261 GW generation capacity from renewables, but only an energy storage capacity of 24.2 GW. Renewables, such as solar and wind, are intermittent, therefore, we cannot fully rely on renewables until we develop new technologies for storage.

Ammonia (NH_3) is a promising storage medium for excess electricity generated from renewables. Instead of curtailing renewable energy plants during peak hours to prevent grid overload, the excess electricity can be used to electrolyze water to produce H_2 which can then be used to in the Haber Bosch process to produce NH_3. NH_3 meets the standards set by the United States Department of Energy for hydrogen storage and can be utilized in a direct ammonia fuel cell (DAFC) to generate electricity. However, the oxidation of NH_3 to N_2, nitrogen evolution reaction (NER), is kinetically challenging and incurs large overpotentials

under ambient conditions. Developing robust catalysts to mediate the NER are therefore needed.

Herein, we report a series of high-valent tetranuclear nickel clusters isolated from the chemical oxidation of an all Ni(II) ([Ni_4]) neutral cluster. Electrochemical analysis of [Ni_4] reveals three reversible sequential oxidations at 0.248 V ($1e^-$), 0.678 V ($1e^-$), and 0.991 V ($2e^-$) vs. Fc^+/Fc corresponding to mono-, di-, and tetra-oxidized species, $[Ni_4]^+$,$[Ni_4]^{2+}$, $[Ni_4]^{4+}$, respectively. Using spectroscopic, crystallographic, magnetometric, and computational techniques, we assign the primary loci of oxidations to the Ni centers in each case, thus resulting in the isolation of the first tetranuclear all-Ni(III) cluster,$[Ni_4]^{4+}$. The $[Ni_4]^{4+}$ contains the most high-valent nickel atoms to be reported in a molecule to be crystallographically characterized. Preliminary studies indicate the [Ni_4] and its derivatives are promising candidates for investigating electrocatalytic NER and is described in this thesis.

Additionally, we describe a transition from studying NER molecular catalysts in organic solvents to water. For smaller devices, aqueous DAFC show promise for industrial viability with volumetric energy densities comparable to or larger than compressed H_2 and ~2000x higher than in organic solvents. Ruthenium Bipyridinedicarboxylate (RuBda) complexes are renowned for catalyzing water oxidation at rapid rates (~300 s^{-1}) and were recently reported to catalyze NER in acetonitrile at sluggish rates (~0.5 s^{-1}). We report a RuBda derivative capable of catalyzing the NER electrochemically in water achieving high faradaic efficiencies (>84%) and several turnovers. Under aqueous conditions, the complex exhibits the highest TOF (~4130 s^{-1}) to be reported for a NER electrocatalyst and displays impressive stability in realistic commercial concentrations of NH_3 (14,300 equivalents excess) without

any indication of decomposition. Our kinetic analyses suggest that the catalyst operates via a unimolecular mechanism which is highly applicable for commercially viable fuel cells.

TABLE OF CONTENTS

LIST OF FIGURES

LIST OF SCHEMES

LIST OF TABLES

Chapter 1

Introduction

1.1 Storing Renewable Energy in Ammonia

1.1.1 Complications with energy storage

With growing complications due to climate change, it is important that we transition from fossil fuels to renewable energy with haste. Fossil fuels are easily utilized when necessary to meet energy demand while renewables are intermittent e.g., solar and wind, which complicates the transition. In 2020, 60% of the electricity generated in the United States was the result of fossil fuels while only 20% originated from renewables.[1] Currently, it is projected that 47% and 42% of the electricity generated in the United States will originate from fossil fuels and renewables respectively.[1] The 22% increase in renewables is an improvement, however, only a 13% decrease on fossil fuel electricity generation does not meet the Paris Agreement target to prevent global temperatures from surpassing pre-industrial levels by 1.5°C, for which we need to curtail emissions by 7.6% per year from 2020 to 2030.[2]

To increase the reliability and production of electricity generated from renewables, we need to store excess electricity generated during off-peak hours to be used during times and/or in locations where renewable resources are scarce. In 2020, the United States had an energy storage capacity of 24.2 GW while it had a 261 GW generation capacity from renewables. Energy storage in the form of electricity is limited to pumped hydro storage (95%) and batteries (~5%). Pumped hydro and batteries have been studied and utilized for several decades; however, the last pump hydro facility was installed in 2012 and currently there are no additional pump hydro plant plans in development. The United States energy storage capacity is far from achieving the energy generation capacity of renewables, yet energy storage capacity hasn't changed significantly for almost a decade.[3] Therefore, it is pertinent that we shift our focus towards different carbon-neutral energy storage with haste and efficiency.

1.1.2 Shifting towards a hydrogen fuel economy

If well optimized, the hydrogen (H_2) fuel economy is a viable candidate to replace our current fossil fuel economy as it would substantially decrease carbon-containing greenhouse gas (GHG) emissions. Hydrogen generated from water electrolysis can be carbon-neutral, however, the reaction to produce O_2 from water is thermodynamically challenging and energy intensive. Instead of curtailing renewable energy plants during off-peak hours, they can be left running and the excess electricity generated can be used for water electrolysis. The hydrogen generated from water electrolysis can then be utilized in a hydrogen fuel cell to generate electricity on demand. The fuel cell operates by oxidizing H_2 at the anode to protons (H^+) and reducing O_2 to H_2O at the cathode utilizing the protons supplied from the adjacent anodic reaction with a thermodynamic cell potential of 1.23 V.

Storage is a key issue inhibiting our transition to a hydrogen fuel economy. Hydrogen is the smallest diatomic molecule and will readily leak from various storage containers.[4] Storage of hydrogen by compression or condensation do little to relieve this burden as the compression of hydrogen at room temperature requires a pressure of 750 bars or 150 bars if the temperature is reduced to -196°C.[4] Instead of storing hydrogen in its diatomic state, we can instead use hydrogen generated from water electrolysis in the Haber Bosch process to effectively store it in the form of ammonia.[5]

1.1.3 Storing hydrogen in ammonia

The United States Department of Energy (DOE) has specified hydrogen storage parameters for gravimetric energy density (GED) and volumetric energy density (VED) targets to be reached by 2020, 2025, and the ultimate target values for a long-term optimized energy system. The 2020 and 2025 GED and VED targets are 5.4 MJ/kg, 6.5 MJ/kg, 3.6 MJ/L, and 4.7 MJ/L respectively while the ultimate targets are 7.9 MJ/kg and 6.1 MJ/L. Ammonia is the most hydrogen dense molecule aside from hydrogen itself and it can be liquified at 20°C with pressure of 8 bar.[6] Liquid ammonia has GED of 18.6 MJ/kg and VED of 11.4 MJ/L while compressed hydrogen has a GED of 120.2 MJ/kg and VED of 2.2 MJ/L. While it suffers a significant loss in GED compared to hydrogen itself, ammonia exceeds the VED of hydrogen and surpasses the ultimate targets set by the DOE.

Because of its utilization as fertilizer, the infrastructure for the physical storage and international transportation of ammonia are already optimized. The electrolysis of ammonia offers its utility to produce hydrogen on-site or for use in a direct ammonia fuel cell (DAFC), both of which are attractive technologies.[4, 6-10] The cracking of ammonia to hydrogen takes advantage of current hydrogen fuel cell technology which can access a higher cell potential than a DAFC. However, ammonia is cheaper than hydrogen on a source-to-tank basis.[11] A DAFC bypasses the need to install ammonia cracking units at fuel stations and obviates the safety concerns associated with hydrogen.[4] The ideal scenario is to utilize both technologies where they are best applicable.

1.2 Direct Ammonia Fuel Cells (DAFCs)

1.2.1 Solid-oxide fuel cells

Ammonia fed Solid-oxide fuel cells (SOFC) are highly efficient technologies for generating power.[4, 6] The type of membrane used in the system dictates the type of SOFC, such as the oxygen anion conducting membrane (SOFC-O) and the proton conducting membrane (SOFC-H). Regardless of the membrane type, SOFCs are operated at high temperatures ranging from 500-1000°C to increase the reactivity of the anodic catalyst to efficiently crack NH_3 into N_2 and H_2. For SOFC-Os, the cathode reduces O_2 to oxygen anions (O^{2-}) which travels across the anion exchange membrane. At the anode, the H_2 produced from cracking NH_3 reacts with O^{2-} to produce H_2O (equations 1 and 2).

$$anode\ reaction: H_2 + O^{2-} \rightarrow H_2O + 2e^- \quad (1)$$

$$cathode\ reaction: O_2 + 4e^- \rightarrow 2O^{2-} \quad (2)$$

For SOFC-Hs, the H_2 generated at the anode is further oxidized into protons (H^+) that travel across the proton exchange membrane to react with O_2 at the cathode to produce H_2O (equations 3 and 4).

$$anode\ reaction: H_2 + O^{2-} \rightarrow H_2O + 2e^- \quad (3)$$

$$cathode\ reaction: O_2 + 4e^- \rightarrow 2O^{2-} \quad (4)$$

The generation of H_2O at the anode is deleterious in SOFC-Os due to formation of NOx, a toxic greenhouse gas, and steam, which leads to corrosion of metal piping, causing them to lose traction.[4, 6] The high temperatures required for both types of SOFCs inhibits the technology from being utilized in smaller devices such as vehicles. Despite this aspect, SOFC-Hs are considered to be the most promising ammonia fuel cell technology.[6]

1.2.2 Alkaline Ammonia Fuel Cells

Alkaline Ammonia Fuel Cells (AAFC) operate at considerably lower temperatures than that of SOFCs and been utilized in systems relating to vehicles and energy storage.[6] The typical systems utilize a potassium hydroxide (KOH) electrolyte in aqueous solutions or exclude water from the system and operate at temperatures between 200-450°C using molten NaOH/KOH electrolyte.[6] Recently, an AAFC was reported to reach a peak power density of 135 mW cm^{-2} while maintaining impressive stability.[11] Either an anion exchange (AEM) or cation exchange membrane (CEM) can be used in an AAFC, which dictates the reactions performed at both the anode and cathode (equations 5-8).[6]

$$AEM\ AAFC\ anode\ reaction: 2NH_3 + 6OH^- \rightarrow N_2 + 6H_2O + 6e^- \quad (5)$$

$$AEM\ AAFC\ cathode\ reaction: \frac{3}{2}O_2 + 3H_2O + 6e^- \rightarrow 6OH^- \quad (6)$$

$$CEM\ AAFC\ anode\ reaction: 8NH_3 \rightarrow N_2 + 6{NH_4}^+ + 6e^- \quad (7)$$

$$CEM\ AAFC\ cathode\ reaction: O_2 + 4{NH_4}^+ + 4e^- \rightarrow 2H_2O + 4NH_3 \quad (8)$$

While SOFCs currently exhibit the highest power output over any kind of DAFCs, AAFCs are likely to be the type of DAFC that would be commercialized in devices for public use.[6] As such, investigations of molecular catalysts to operate under more ambient conditions should be designed to catalyze reactions involved in either AEM or CEM AAFCs.

1.3 Investigating Nitrogen Evolution Reaction with Molecular Catalysts

The oxidative conversion of NH_3 to N_2 is an energetically uphill reaction that suffers large overpotentials due the kinetics associated with the 6e$^-$ and 6H$^+$ transformation. Currently, the top performing DAFCs utilize catalysts, mostly nickel based, requiring high temperatures (~400-800°C) to increase their reactivity for the reaction.[6] Reactivity with lower overpotentials at ambient conditions can be achieved with platinum based electrodes, however, the cost and formation of inert platinum-nitrides at the surface complicates their viability.[6, 12, 13] Further complicating the matter is reaction selectivity for the clean conversion of NH_3 to N_2. Such that heterogeneous catalysts can produce nitrogen oxide (NOx) species which are deleterious for their existence as a greenhouse gas and toxicity but can also lead to surface poisoning of the solid catalyst.[6, 7, 14, 15] Molecular catalysts offer frameworks that can be more easily tuned for reactivity than heterogeneous catalysts making them promising platforms for addressing these issues of kinetics, selectivity, and catalyst poisoning.

While multi-electron reactions like water oxidation[16-20] and nitrogen reduction[21-23] are well studied and optimized, studies on ammonia oxidation reaction are lacking.[24] However, NH_3 oxidation molecular catalysts capable of producing N_2 have gained attention and several catalysts have been reported in recent years utilizing a various methods such as chemical catalysis[25, 26], H-atom abstracting agents[27, 28], and electrochemical catalysis[26, 29-33]. While examples of N_2 formation from NH_3 using methods like chemical catalysis and H-atom abstracting agents are informative, they do not have applications to be used in a fuel cell. With the breadth of work done on studying the effective lowering of N-H BDFEs and routes for N-N bond formations,[24, 34-40] further studies on electrochemical catalysts are most important for moving forward towards viable technologies. Recently, a diruthenium complex was reported to catalyze the oxidation of NH_3 to N_2 at -0.255 V vs. Fc^+/Fc, making it the first thermodynamic viable molecular catalyst for a DAFC.[33]

1.4 Thermodynamic and Practical Considerations for Studying Nitrogen Evolution Reaction

1.4.1 Preliminary Thermodynamic Considerations

Liquid NH_3 boasts a large volumetric energy density (VED, 11.4 MJ/L) making it the ideal solvent for DAFCs. However, with DAFCs emerging as relatively new technologies for energy storage, the immediate utilization of liquid NH_3 in certain devices, e.g., vehicles, may be challenging. For such technologies, it is more ideal to operate DAFCs in smaller devices with NH_3 diluted in a solvent. The VED of liquid NH_3 is substantially larger than both compressed and liquid H_2, however, diluting NH_3 will decrease the VED. Therefore, for a diluted NH_3 solution utilized in a DAFC to be relevant, the VED must be comparable to that of compressed H_2 and meet the United States DOE standards for H_2 storage (*vide-supra*). The two solvents we discuss in this section are water and acetonitrile (MeCN). MeCN is the most common solvent used to study NER molecular electrocatalysts, however, our analysis indicates that water is the most viable solvent for a DAFC with diluted NH_3.

1.4.2 Thermodynamic and Practical Considerations of Water and Acetonitrile

The volumetric energy density of a diluted DAFC operated under ambient conditions is determined from the free energy of formation rather than the enthalpy of formation. For water, the ΔG_f° of NH_3 in water is reported ($\Delta G_f{}^{\circ}\ \mathrm{NH}_{3(aq)} = -26.57\ \frac{kJ}{mol}$) in the CRC handbook, but it can be derived from the N_2/NH_3 reduction potential in water using reported values.[41] The VED of an aqueous and organic DAFC can be determined from the gravimetric energy density (GED). The calculations are provided below.

Determination of ΔG_{rxn}°

$$N_{2(g)}/NH_{3(aq)} = 0.0917\ V\ at\ pH\ 0$$

$$\Delta G_f{}^{\circ}\ 2\mathrm{NH}_{3(aq)} = -nFE^{\circ}$$

$$\Delta G_f{}^{\circ}\ 2\mathrm{NH}_{3(aq)} = -6 \cdot 96485\frac{C}{mol} \cdot 0.0918\frac{J}{C}$$

$$\Delta G_f{}^{\circ}\ 2\mathrm{NH}_{3(aq)} = -53.14\frac{kJ}{mol}$$

$$\Delta G_f{}^{\circ}\ \mathrm{NH}_{3(aq)} = -26.57\frac{kJ}{mol}$$

$$Full\ Reaction{:}\ \frac{3}{2}O_2 + 2NH_3 \rightarrow N_2 + 3H_2O$$

$$\Delta G_{rxn}{}^{\circ} = \left(\Delta G_f{}^{\circ}\mathrm{N}_{2(g)} + 3\Delta G_f{}^{\circ}H_2O_{(liq)}\right) - (\frac{3}{2}\Delta G_f{}^{\circ}O_{2(g)} + 2\Delta G_f{}^{\circ}\ \mathrm{NH}_{3(aq)})$$

$$\Delta G_{rxn}{}^{\circ} = \left(0\frac{kJ}{mol} + 3 \cdot -237.14\frac{kJ}{mol}\right) - (\frac{3}{2} \cdot 0\frac{kJ}{mol} + 2 \cdot -26.57\frac{kJ}{mol})$$

$$\Delta G_{rxn}{}^{\circ} = -658.27\frac{kJ}{mol}\ for\ 2\ mol\ of\ NH_3$$

$$\Delta G_{rxn}{}^{\circ} = -329.14\frac{kJ}{mol}\ for\ 1\ mol\ of\ NH_3$$

The accurate GED of $NH_{3(aq)}$ can be determined by using the commercial weight percentage of aqueous NH_3 solutions (30% w/w)

$$GED\ NH_{3(aq)} = 329.14\frac{kJ}{mol} \cdot \frac{mol}{17\ g} \cdot \frac{1000g}{kg} \cdot \frac{MJ}{1000kJ}$$

$$GED\ NH_{3(aq)} = 19.36\frac{MJ}{kg} \quad (assuming\ 100\%\ w/w)$$

$$GED\ NH_{3(aq)} = 19.36\frac{MJ}{kg} \cdot 30\%\ (correcting\ for\ commercial\ concentrations)$$

$$GED\ NH_{3(aq)} = 5.81\frac{MJ}{kg}\ for\ 30\%\ w/w\ solutions$$

The VED of a 30% $NH_{3(aq)}$ solution can be determined from its known density 0.892 kg/L

$$VED\ NH_{3(aq)} = 5.81\frac{MJ}{kg} \cdot 0.892\frac{kg}{L}$$

$$VED\ NH_{3(aq)} = 5.18\frac{MJ}{L}$$

Using reported values, we can also derive the VED of $NH_{3(MeCN)}$ using the same methods above. The reported solubility of NH_3 in MeCN under ambient conditions is 2 M.[41] However, the density of this solution is not reported. Therefore, for our calculations we will assume that the density of a 2 M $NH_{3(MeCN)}$ solution is equivalent to the density of pure MeCN at room temperature (0.786 kg/L). If the density of NH_3 solutions in MeCN follows the same trend as aqueous solutions then the aforementioned assumption of the density will overestimate the VED and provide a more competitive comparison. The calculations for MeCN solutions utilize potentials referenced to ferrocene for both NH_3 and H_2O and do not need any corrections.

Determination of $\Delta G_{rxn}°$ for $NH_{3(MeCN)}$

$$N_{2(g)}/NH_{3(MeCN)}\ = 0.035\ V\ at\ pk_a\ 0$$

$$\Delta G_f°\ 2\mathrm{NH}_{3(MeCN)} = -nFE°$$

$$\Delta G_f°\ 2\mathrm{NH}_{3(MeCN)} = -6 \cdot 96485\frac{C}{mol} \cdot 0.035\frac{J}{C}$$

$$\Delta G_f°\ 2\mathrm{NH}_{3(MeCN)} = -20.26\frac{kJ}{mol}$$

$$\Delta G_f°\ \mathrm{NH}_{3(aq)} = -10.13\frac{kJ}{mol}$$

The free energy of formation of H_2O in MeCN is not as well available, therefore, we calculate it as follows using reported values[42]:

Determination of $\Delta G_{rxn}°$ for $NH_{3(MeCN)}$

$$O_{2(g)}/H_2O_{(MeCN)} \ = 1.21\ V\ at\ pk_a \ = 0$$

$$\Delta G_f°\ 2H_2O_{(MeCN)} = -nFE°$$

$$\Delta G_f°\ 2H_2O_{(MeCN)} = -4 \cdot 96485\frac{C}{mol} \cdot 1.21\frac{J}{C}$$

$$\Delta G_f°\ 2H_2O_{(MeCN)} = -466.99\frac{kJ}{mol}$$

$$\Delta G_f°\ H_2O_{(MeCN)} = -233.49\frac{kJ}{mol}$$

$$Full\ Reaction\colon \frac{3}{2}O_{2(g)} + 2NH_{3(MeCN)} \rightarrow N_{2(g)} + 3H_2O_{(MeCN)}$$

$$\Delta G_{rxn}° = \left(\Delta G_f°\mathrm{N}_{2(g)} + 3\Delta G_f°H_2O_{(MeCN)}\right) - (\frac{3}{2}\Delta G_f°O_{2(g)} + 2\Delta G_f°\ \mathrm{NH}_{3(MeCN)})$$

$$\Delta G_{rxn}° = \left(0\frac{kJ}{mol} + 3 \cdot -233.49\frac{kJ}{mol}\right) - (\frac{3}{2} \cdot 0\frac{kJ}{mol} + 2 \cdot -10.13\frac{kJ}{mol})$$

$$\Delta G_{rxn}° = -680.21\frac{kJ}{mol}\ for\ 2\ mol\ of\ NH_{3(MeCN)}$$

$$\Delta G_{rxn}° = -340.11\frac{kJ}{mol}\ for\ 1\ mol\ of\ NH_{3(MeCN)}$$

The GED of $NH_{3(MeCN)}$ can be determined by using the weight percentage of MeCN NH_3 solutions. We calculate this using the assumed density of a 2 M solution as 0.786 kg/L.

$$\frac{2\ mol_{\ NH_3}}{L_{MeCN}} \cdot \frac{1\ L_{MeCN}}{786\ g_{MeCN}} = 2.54x10^{-3}\frac{mol_{NH_3}}{g_{MeCN}}$$

$$2.54x10^{-3}\frac{mol_{NH_3}}{g_{MeCN}} \cdot \frac{g_{NH_3}}{17\ mol_{NH_3}} = 0.15x10^{-3}\frac{g_{NH_3}}{g_{MeCN}} = 0.015\%\ w/w$$

$$GED\ NH_{3(MeCN)} = \ 340.11\frac{kJ}{mol}\cdot\frac{mol}{17\ g}\cdot\frac{1000g}{kg}\cdot\frac{MJ}{1000kJ}$$

$$GED\ NH_{3(MeCN)} = 20.01\frac{MJ}{kg} \quad (assuming\ 100\%\ w/w)$$

$$GED\ NH_{3(MeCN)} = 20.01\frac{MJ}{kg}\ \cdot 0.015\%\ (correcting\ for\ experimental\ concentrations)$$

$$GED\ NH_{3(aq)} = 0.30\frac{MJ}{kg}\ for\ 0.015\%\ w/w\ solutions$$

The VED of a 0.015% w/w $NH_{3(MeCN)}$ solution can be determined from its assumed density 0.786 kg/L.

$$VED\ NH_{3(MeCN)} = 0.30\frac{MJ}{kg}\cdot 0.786\frac{kg}{L}$$

$$VED\ NH_{3(aq)} = 0.24\frac{MJ}{L}$$

1.4.3 Transitioning Investigations from Organic to Aqueous Conditions

From the calculations, the VED of commercial aqueous NH_3 solutions is 5.18 MJ/L while the VED of experimental acetonitrile NH_3 solutions is 0.24 MJ/L. Therefore, unless an organic solvent is utilized that has a significantly higher NH_3 solubility, organic DAFCs will never be commercialized. However, the VED of aqueous DAFCs are competitive with compressed H_2, and therefore have commercial viability. Aqueous NH_3 is considerably less toxic than anhydrous NH_3 and is non-flammable, further strengthening its prospects as a fuel. Several aqueous NH_3 fuel cells have been reported with respectable cell potentials and peak power densities operating between 25-120°C.[6, 11, 43] The major concern of aqueous NH_3 fuel cells is the production NO_x species at the anode.[6] As such, an ideal catalyst for the aqueous NER from NH_3 should ideally favor the NER over the formation of NO_x species. As such, researchers should shift their studies on molecular catalysts from organic media and focus on investigating molecular catalysts that can be used under commercially viable conditions.

1.5 Scope of thesis

As will be described in this thesis, we sought to investigate the prospects of homogeneous NH_3 oxidation catalysis to produce N_2. For this, we screened a variety of mono- and polynuclear metal complexes for their viability to catalyze the kinetically challenging $6e^-$ oxidation reaction. The research led to the isolation of a novel tetranuclear nickel cluster ($[Ni_4]$) which exhibited rare redox characteristics. By carefully controlling the stoichiometry and identity of the oxidants used to treat the cluster, we could crystallographically characterize the mono-, di-, and tetra-oxidized products of $[Ni_4]$. The tetraoxidized $[Ni_4]$ was the first fully high valent tetranuclear nickel cluster and the second molecule to containing Ni(III)-Ni(III) bonds to be reported (Chapter 2). Along with its rich redox properties, we performed preliminary experiments which suggested that $[Ni_4]$ could perform as an electrocatalyst for oxidizing NH_3 to N_2. To investigate the extent for which we could influence its redox properties for reactivity, we synthesized analogs of the $[Ni_4]$ by modifying the ligand substituents. Modification of the ligand structure had varied effects on the redox properties depending on the identity of ligand functionalization. For reactivity, we demonstrated that methylation of the $[Ni_4]$ adjusts the onset potential for catalytic NH_3 oxidation cathodically (Chapter 3). Finally, after analyzing the various molecular catalysts for NER reported in the last two years, we investigated how we could improve the conditions for which NER molecular catalysts could be studied. Such that the conditions used to investigate molecular catalysts would be viable for practical applications. As described in Chapter 1 of this thesis, we determined that organic DAFCs lack viability however, aqueous DAFC have VEDs competitive with H_2 fuel cells. We screened reported NER molecular catalysts and found that a Ruthenium Bipyridinedicarboxylate (RuBda) analog was capable of catalyzing NER under aqueous conditions under commercialized conditions. Under these conditions we also showed that its reactivity was superior to that of its performance in organic solvent.

In Chapters 2-4, all compounds were prepared and characterized by the author except for Density Functional Theory (DFT) analysis by Laurent Maron and coworkers at Université de Toulouse. In Chapters 2 and 3, all electrochemical experiments were performed by the author. In Chapter 4, the majority of the electrochemical experiments were performed by the author with some assistance from Arun Chakraborty. In Chapter 4, all GC-TCD results were made possible by Arun Chakraborty and data collection responsibilities were shared between Arun Chakraborty and the Author.

At the time of this writing, Chapter 2 has been published. Portions of Chapter 3 and all of Chapter 4 are in preparation for publication.

Chapter 2: Jacob, S. I.; Douair, I.; Wu, G.; Maron, L.; Menard, G., *Chem Commun* **2020,** *56* (59), 8182-8185.

Chapter 3: Manuscript in preparation

Chapter 4: Manuscript in preparation

1.6 References

1. Electricity. Administration, U. S. E. I., Ed. 2021.
2. UNEP, U. D. P., Emissions Gap Report 2020. Programme, U. E., Ed. 2020.
3. . Most pumped storage electricity generators in the U.S. were built in the 1970s *U.S. Energy Information Administration* [Online], 2019. https://www.eia.gov/todayinenergy/detail.php?id=41833#.
4. Adli, N. M.; Zhang, H.; Mukherjee, S.; Wu, G., Review—Ammonia Oxidation Electrocatalysis for Hydrogen Generation and Fuel Cells. *Journal of The Electrochemical Society* **2018,** *165* (15), J3130-J3147.
5. Service, R. F., Ammonia—a renewable fuel made from sun, air, and water—could power the globe without carbon. *Science* **2018**.
6. Jeerh, G.; Zhang, M.; Tao, S., Recent progress in ammonia fuel cells and their potential applications. *Journal of Materials Chemistry A* **2021,** *9* (2), 727-752.
7. Li, Y.; Pillai, H. S.; Wang, T.; Hwang, S.; Zhao, Y.; Qiao, Z.; Mu, Q.; Karakalos, S.; Chen, M.; Yang, J.; Su, D.; Xin, H.; Yan, Y.; Wu, G., High-performance ammonia oxidation catalysts for anion-exchange membrane direct ammonia fuel cells. *Energy & Environmental Science* **2021,** *14* (3), 1449-1460.
8. Rees, N. V.; Compton, R. G., Carbon-free energy: a review of ammonia- and hydrazine-based electrochemical fuel cells. *Energy & Environmental Science* **2011,** *4* (4).
9. Afif, A.; Radenahmad, N.; Cheok, Q.; Shams, S.; Kim, J. H.; Azad, A. K., Ammonia-fed fuel cells: a comprehensive review. *Renewable and Sustainable Energy Reviews* **2016,** *60*, 822-835.

10. Lan, R.; Tao, S., Ammonia as a Suitable Fuel for Fuel Cells. *Frontiers in Energy Research* **2014,** *2*.

11. Zhao, Y.; Setzler, B. P.; Wang, J.; Nash, J.; Wang, T.; Xu, B.; Yan, Y., An Efficient Direct Ammonia Fuel Cell for Affordable Carbon-Neutral Transportation. *Joule* **2019,** *3* (10), 2472-2484.

12. Little, D. J.; Smith, I. I. I. M. R.; Hamann, T. W., Electrolysis of liquid ammonia for hydrogen generation. *Energy & Environmental Science* **2015,** *8* (9), 2775-2781.

13. Kim, H.; Yang, W.; Lee, W. H.; Han, M. H.; Moon, J.; Jeon, C.; Kim, D.; Ji, S. G.; Chae, K. H.; Lee, K.-S.; Seo, J.; Oh, H.-S.; Kim, H.; Choi, C. H., Operando Stability of Platinum Electrocatalysts in Ammonia Oxidation Reactions. *ACS Catalysis* **2020,** *10* (19), 11674-11684.

14. Candido, L.; Gomes, J. A. C. P., Evaluation of anode materials for the electro-oxidation of ammonia and ammonium ions. *Materials Chemistry and Physics* **2011,** *129* (3), 1146-1151.

15. Valera-Medina, A.; Amer-Hatem, F.; Azad, A. K.; Dedoussi, I. C.; de Joannon, M.; Fernandes, R. X.; Glarborg, P.; Hashemi, H.; He, X.; Mashruk, S.; McGowan, J.; Mounaim-Rouselle, C.; Ortiz-Prado, A.; Ortiz-Valera, A.; Rossetti, I.; Shu, B.; Yehia, M.; Xiao, H.; Costa, M., Review on Ammonia as a Potential Fuel: From Synthesis to Economics. *Energy & Fuels* **2021,** *35* (9), 6964-7029.

16. Okamura, M.; Masaoka, S., Design of mononuclear ruthenium catalysts for low-overpotential water oxidation. *Chem Asian J* **2015,** *10* (2), 306-15.

17. Zhang, B.; Sun, L., Artificial photosynthesis: opportunities and challenges of molecular catalysts. *Chem Soc Rev* **2019,** *48* (7), 2216-2264.

18. Matheu, R.; Ertem, M. Z.; Gimbert-Surinach, C.; Sala, X.; Llobet, A., Seven Coordinated Molecular Ruthenium-Water Oxidation Catalysts: A Coordination Chemistry Journey. *Chem Rev* **2019,** *119* (6), 3453-3471.

19. Das, B.; Rahaman, A.; Shatskiy, A.; Verho, O.; Karkas, M. D.; Akermark, B., The Impact of Ligand Carboxylates on Electrocatalyzed Water Oxidation. *Acc Chem Res* **2021,** *54* (17), 3326-3337.

20. Kondo, M.; Tatewaki, H.; Masaoka, S., Design of molecular water oxidation catalysts with earth-abundant metal ions. *Chem Soc Rev* **2021,** *50* (12), 6790-6831.

21. Chalkley, M. J.; Drover, M. W.; Peters, J. C., Catalytic N2-to-NH3 (or -N2H4) Conversion by Well-Defined Molecular Coordination Complexes. *Chem Rev* **2020,** *120* (12), 5582-5636.

22. Chalkley, M. J.; Peters, J. C., Relating N-H Bond Strengths to the Overpotential for Catalytic Nitrogen Fixation. *Eur J Inorg Chem* **2020,** *2020* (15-16), 1353-1357.

23. Tanabe, Y.; Nishibayashi, Y., Comprehensive insights into synthetic nitrogen fixation assisted by molecular catalysts under ambient or mild conditions. *Chem Soc Rev* **2021,** *50* (8), 5201-5242.

24. Dunn, P. L.; Cook, B. J.; Johnson, S. I.; Appel, A. M.; Bullock, R. M., Oxidation of Ammonia with Molecular Complexes. *J Am Chem Soc* **2020,** *142* (42), 17845-17858.

25. Nakajima, K.; Toda, H.; Sakata, K.; Nishibayashi, Y., Ruthenium-catalysed oxidative conversion of ammonia into dinitrogen. *Nat Chem* **2019,** *11* (8), 702-709.

26. Toda, H.; Kuroki, K.; Kanega, R.; Kuriyama, S.; Nakajima, K.; Himeda, Y.; Sakata, K.; Nishibayashi, Y., Manganese-Catalyzed Ammonia Oxidation into Dinitrogen under Chemical or Electrochemical Conditions*. *Chempluschem* **2021**.

27. Bhattacharya, P.; Heiden, Z. M.; Chambers, G. M.; Johnson, S. I.; Bullock, R. M.; Mock, M. T., Catalytic Ammonia Oxidation to Dinitrogen by Hydrogen Atom Abstraction. *Angew Chem Int Ed Engl* **2019,** *58* (34), 11618-11624.

28. Dunn, P. L.; Johnson, S. I.; Kaminsky, W.; Bullock, R. M., Diversion of Catalytic C-N Bond Formation to Catalytic Oxidation of NH3 through Modification of the Hydrogen Atom Abstractor. *J Am Chem Soc* **2020,** *142* (7), 3361-3365.

29. Zott, M. D.; Garrido-Barros, P.; Peters, J. C., Electrocatalytic Ammonia Oxidation Mediated by a Polypyridyl Iron Catalyst. *ACS Catalysis* **2019,** *9* (11), 10101-10108.

30. Habibzadeh, F.; Miller, S. L.; Hamann, T. W.; Smith, M. R., 3rd, Homogeneous electrocatalytic oxidation of ammonia to N2 under mild conditions. *Proc Natl Acad Sci U S A* **2019,** *116* (8), 2849-2853.

31. Zott, M. D.; Peters, J. C., Enhanced Ammonia Oxidation Catalysis by a Low-Spin Iron Complex Featuring Cis Coordination Sites. *J Am Chem Soc* **2021,** *143* (20), 7612-7616.

32. Holub, J.; Vereshchuk, N.; Sanchez-Baygual, F. J.; Gil-Sepulcre, M.; Benet-Buchholz, J.; Llobet, A., Synthesis, Structure, and Ammonia Oxidation Catalytic Activity of Ru-NH3 Complexes Containing Multidentate Polypyridyl Ligands. *Inorg Chem* **2021,** *60* (18), 13929-13940.

33. Trenerry, M. J.; Wallen, C. M.; Brown, T. R.; Park, S. V.; Berry, J. F., Spontaneous N2 formation by a diruthenium complex enables electrocatalytic and aerobic oxidation of ammonia. *Nat Chem* **2021**.

34. <Collman et al. - 1991 - concni i ~ Toward a Dinitrogen Electroreduction Catalyst Complex of a Ruthenium Cofacial Diporphyrin.pdf>.

35. <Collman et al. - 1992 - James P. Collman, James E. Hutchison, Matthew.pdf>.

36. Gutsulyak, D. V.; Piers, W. E.; Borau-Garcia, J.; Parvez, M., Activation of water, ammonia, and other small molecules by PC(carbene)P nickel pincer complexes. *J Am Chem Soc* **2013,** *135* (32), 11776-9.

37. Bezdek, M. J.; Guo, S.; Chirik, P. J., Coordination-induced weakening of ammonia, water, and hydrazine X-H bonds in a molybdenum complex. *Science* **2016,** *354* (6313), 730-733.

38. Bhattacharya, P.; Heiden, Z. M.; Wiedner, E. S.; Raugei, S.; Piro, N. A.; Kassel, W. S.; Bullock, R. M.; Mock, M. T., Ammonia Oxidation by Abstraction of Three Hydrogen Atoms from a Mo-NH3 Complex. *J Am Chem Soc* **2017,** *139* (8), 2916-2919.

39. Keener, M.; Peterson, M.; Hernandez Sanchez, R.; Oswald, V. F.; Wu, G.; Menard, G., Towards Catalytic Ammonia Oxidation to Dinitrogen: A Synthetic Cycle by Using a Simple Manganese Complex. *Chemistry* **2017,** *23* (48), 11479-11484.

40. Nurdin, L.; Yang, Y.; Neate, P. G. N.; Piers, W. E.; Maron, L.; Neidig, M. L.; Lin, J. B.; Gelfand, B. S., Activation of ammonia and hydrazine by electron rich

Fe(ii) complexes supported by a dianionic pentadentate ligand platform through a common terminal Fe(iii) amido intermediate. *Chem Sci* **2020,** *12* (6), 2231-2241.

41. Lindley, B. M.; Appel, A. M.; Krogh-Jespersen, K.; Mayer, J. M.; Miller, A. J. M., Evaluating the Thermodynamics of Electrocatalytic N2 Reduction in Acetonitrile. *ACS Energy Letters* **2016,** *1* (4), 698-704.

42. Pegis, M. L.; Roberts, J. A.; Wasylenko, D. J.; Mader, E. A.; Appel, A. M.; Mayer, J. M., Standard Reduction Potentials for Oxygen and Carbon Dioxide Couples in Acetonitrile and N,N-Dimethylformamide. *Inorg Chem* **2015,** *54* (24), 11883-8.

43. Cinti, G.; Discepoli, G.; Sisani, E.; Desideri, U., SOFC operating with ammonia: Stack test and system analysis. *International Journal of Hydrogen Energy* **2016,** *41* (31), 13583-13590.

Chapter 2

A Tetranuclear Nickel Cluster Isolated in Multiple High-Valent States

2.1 Introduction

Isolated high-valent nickel complexes (Ni^{III}, Ni^{IV}) are relatively rare,[1-6] yet are frequently invoked in mechanistic studies involving reductive elimination steps, particularly in C–C and C–heteroatom bond forming chemistry.[7-10] Bimetallic complexes with formally high-valent cores, $[Ni_2]^{n+}$ ($n > 4$), have been shown to engage in hydroxylation chemistry, as well as C–heteroatom and N–N bond forming reactions.[11-14] Co-facial, high-valent (Ni(III)) cores ($[Ni_2]^{6+}$) are also proposed to stabilize reactive intermediates through metal-metal bonding interactions,[14] similar to more extensively studied heavier $[Pd_2]$ congeners.[15, 16] Co-facial bimetallics have also been extensively studied by Cotton and others[17] using the familiar C_4-symmetric paddlewheel geometries, including in mixed-valent ($[Ni_2]^{5+}$) and all high-valent ($[Ni_2]^{6+}$) cores, providing significant fundamental insights into Ni–Ni bonding interactions.[18, 19] While multinuclear Ni complexes ($[Ni_x]$; $x > 2$) are well known[20-24] – with some isolated in partial higher-valent states[25-28] – to the best of our knowledge, only a few are isolated in all Ni(III) states,[29, 30] and none are tetranuclear. Tethering multiple high-valent centers together may open the door to mediating multi-electron transformations, and may further shed light on core metal-metal bonding interactions in such expanded motifs. Herein, we describe the synthesis and characterization of a tetranuclear $[Ni_4]^{8+}$ cluster with an orthogonal double paddlewheel core, as well as several oxidized forms, including what we assign as the first all Ni(III) tetranuclear cluster. Spectroscopic, crystallographic, and computational studies support the primarily metal-based increasing Ni(III) states in the tetranuclear core upon sequential oxidations.

2.2 Results and Discussion

In order to target higher nuclearity complexes, we modified a known, dinucleating, xanthene-bridged bis-salen ligand[31] by exposing its precursor, 5,5’-(9,9-dimethylxanthene-4,5-diyl)bis(salicylaldehyde), to an excess (10×) of 1,2-diaminobenzene in ethanol under reflux. The product ligand **2.1** was cleanly generated in 84% isolated yield following workup and now features two tridentate pockets, making it more amenable to cluster formation. Metalation of **2.1** with 2 equiv of $Ni(OAc)_2 \cdot 4H_2O$ afforded the tetranuclear complex, L_2Ni_4 (**2.2**), in 50% isolated yield following workup (Scheme 1).

Scheme 2.1. (*i*) [NO][PF_6] (0.9 equiv), DCM, r.t., 4 h; (*ii*) [(2,4-$Br_2C_6H_3)_3N$][$B(C_6F_5)_4$] (2.1 equiv), DCM, r.t., 15 min; (*iii*) [(2,4-$Br_2C_6H_3)_3N$][$B(C_6F_5)_4$] (10 equiv), DCM, r.t., 10 min. Ni-Ni bonding is indicated by bolded green lines.

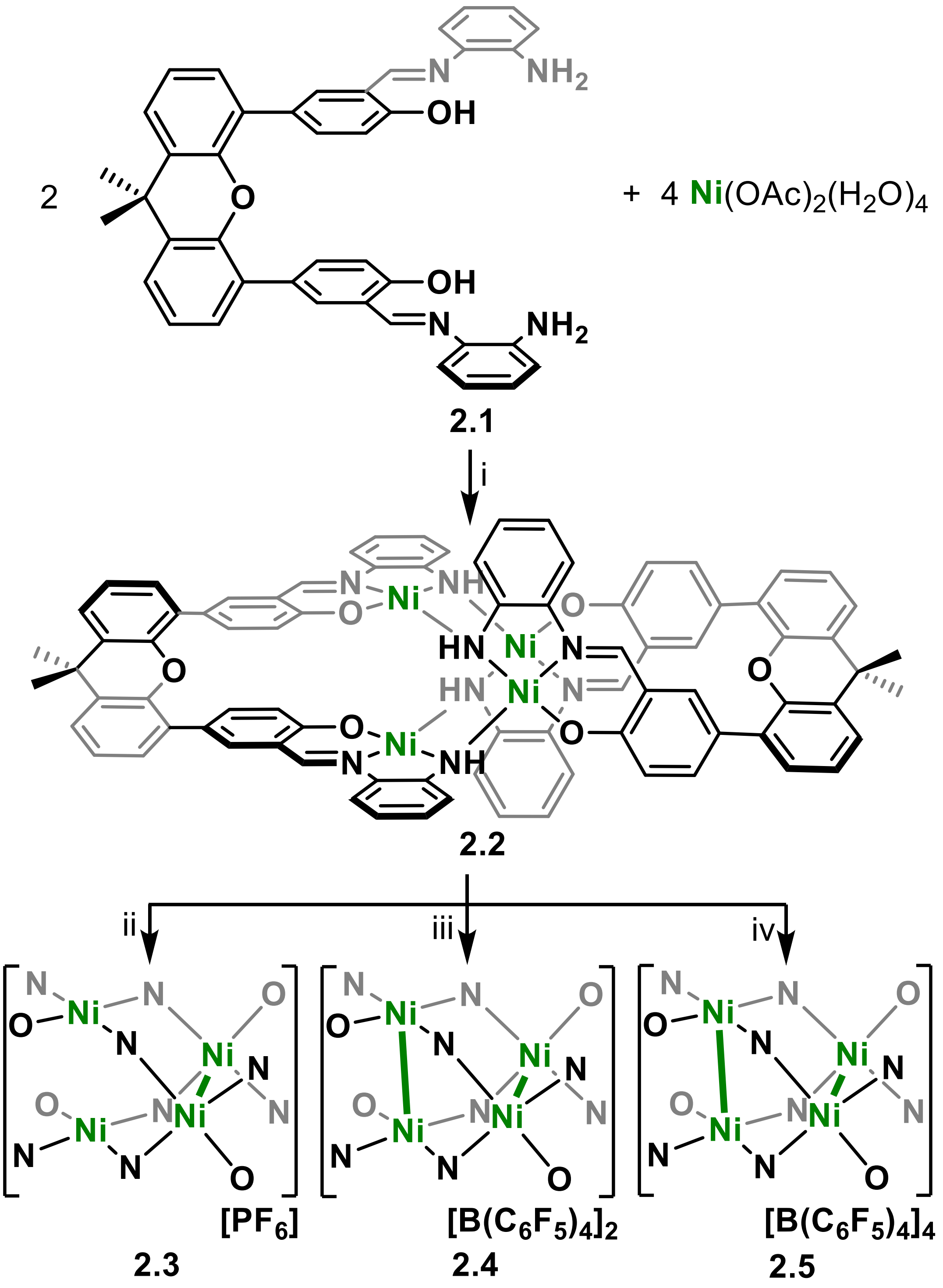

The red, diamagnetic, air stable complex was readily characterized by ^{1}H NMR spectroscopy and MALDI mass spectrometry. Red single crystals suitable for X-ray diffraction (XRD) studies were grown by vapor diffusion of hexanes into a concentrated dichloromethane (DCM) solution. The solid-state molecular structure revealed four Ni centers in square planar geometries with the fourth coordination sites filled by amine donating groups from adjacent ligands (Figure 2.1). The tetranuclear core features co-facial Ni1–Ni2 and Ni3–Ni4 distances of 2.8662(19) Å and 2.886(2) Å, respectively, and adopts an orthogonal double paddlewheel structure (Figure 2.1, Table 2.1). The transverse Ni–Ni distances (ex. Ni_1–Ni_3) are longer and average 3.33 Å.

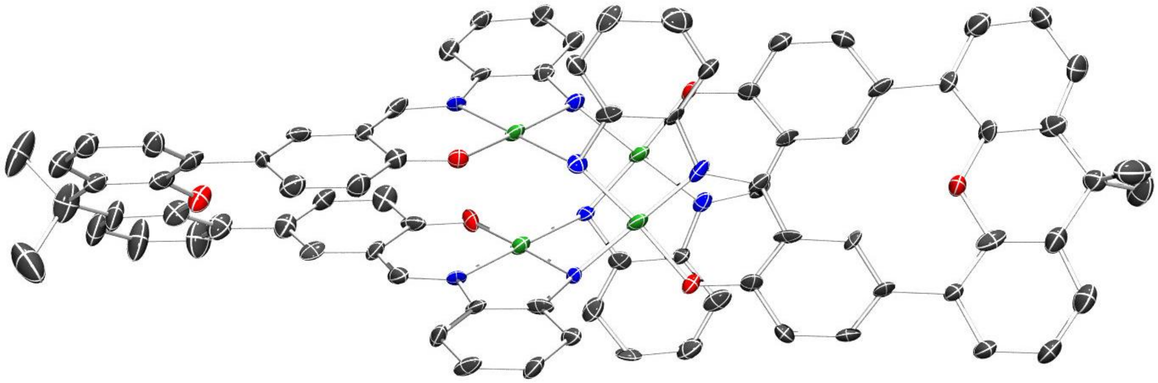

Figure 2.1. Solid state molecular structure of **2.2**. Solid green bond represents long Ni–Ni bond. Hydrogen atoms and co-crystallized solvent molecules are removed for clarity (C, black; N, blue; O, red; Ni, green).

Table 2.1. Ni–Ni and Ni–mean plane distances obtained from single-crystal XRD studies.

		2.2	**2.3**	**2.4**	**2.5**
Ni–Ni distance (Å)	Ni1–Ni2	2.8662(19)	2.889(2)	2.7095(18)	2.686(3)
	Ni3–Ni4	2.886(2)	2.640(2)	2.6284(18)	2.668(3)
	Avg	2.876	2.765	2.669	2.677
	Δ[a]	0.020	0.249	0.081	0.018
Ni–mean plane distance (Å)[b]	Ni1	0.065	0.090	0.114	0.123
	Ni2	0.055	0.073	0.139	0.123
	Ni3	0.080	0.158	0.140	0.143
	Ni4	0.064	0.117	0.131	0.133
	Avg	0.066	0.110	0.131	0.133

[a] Difference between measured Ni1–Ni2 and Ni3–Ni4 distances. [b] The method for these measurements are illustrated in Figure 2.4.

Cyclic voltammetry (CV) of **2.2** in DCM revealed three reversible oxidation events at $E_{1/2}$ values of 0.248, 0.656, and 0.932 V versus the ferrocene/ferrocenium (Fc/Fc$^+$) redox couple (Figure 2.2) in approximate 1:1:2 e$^-$ events, respectively, as determined by relative integrations of the oxidative curves. Chemical isolation of the mono-oxidized product was performed by treatment of **2.2** with an equivalent of [NO][PF$_6$] to yield [L$_2$Ni$_4$][PF$_6$] (**2.3**) (Scheme 2.1). Single crystals suitable for XRD studies were obtained by layering hexanes on a concentrated DCM solution of **2.3** at -40 °C. The solid-state structure revealed a significantly contracted Ni3–Ni4 distance of 2.640(2) Å, and a relatively unperturbed Ni1–Ni2 distance of

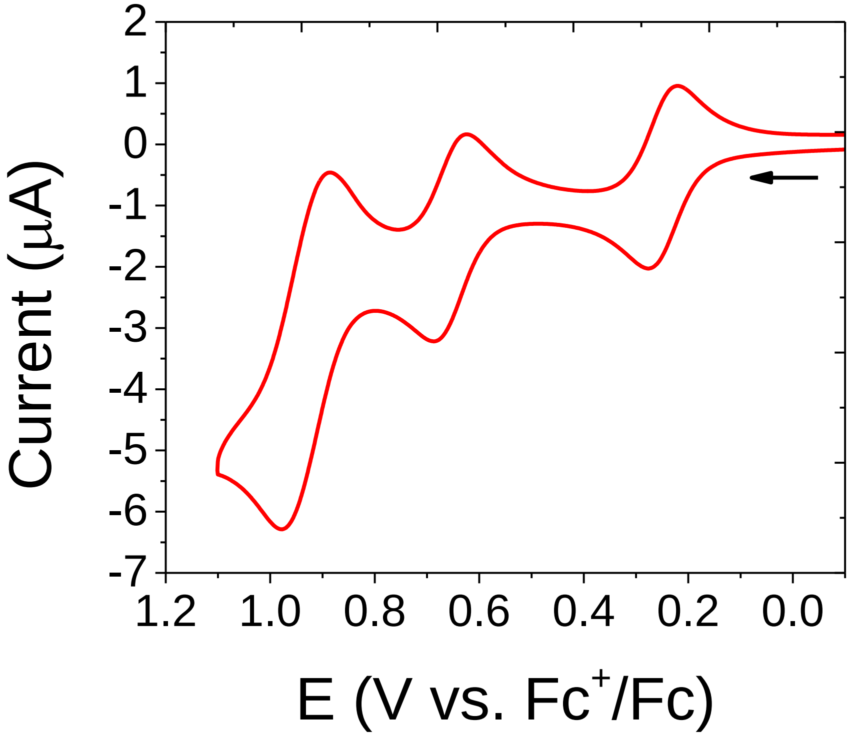

Figure 2.2. CV of **2.2** in DCM at a 10 mV/s scan rate (0.43 mM of **2.2**, 0.1 M [Bu$_4$N][PF$_6$] supporting electrolyte, glassy carbon working electrode, Pt wire counter electrode, and Ag wire pseudo-reference electrode).

2.889(2) Å, identical within error to the Ni3–Ni4 bond in **2.2** (Figure 2.3, Table 2.1). Corresponding protrusions of the Ni centers relative to their respective mean tridentate ligand planes (excluding bridging donor atom from an adjacent ligand) are consistent with the bond length contraction (Table 1, Figure 2.4).

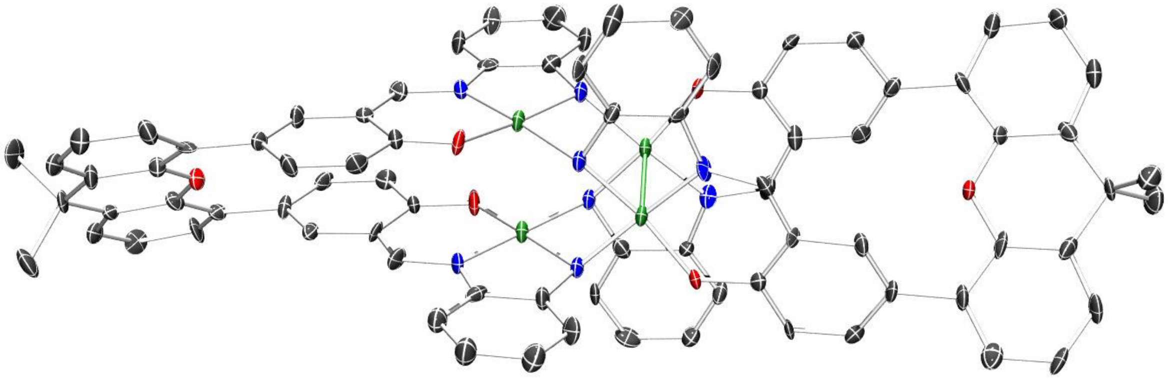

Figure 2.3. Solid state molecular structure of **2.3**. Solid green bond represents long Ni–Ni bond. Hydrogen atoms, co-crystallized solvent molecules, and the counteranion are removed for clarity (C, black; N, blue; O, red; Ni, green).

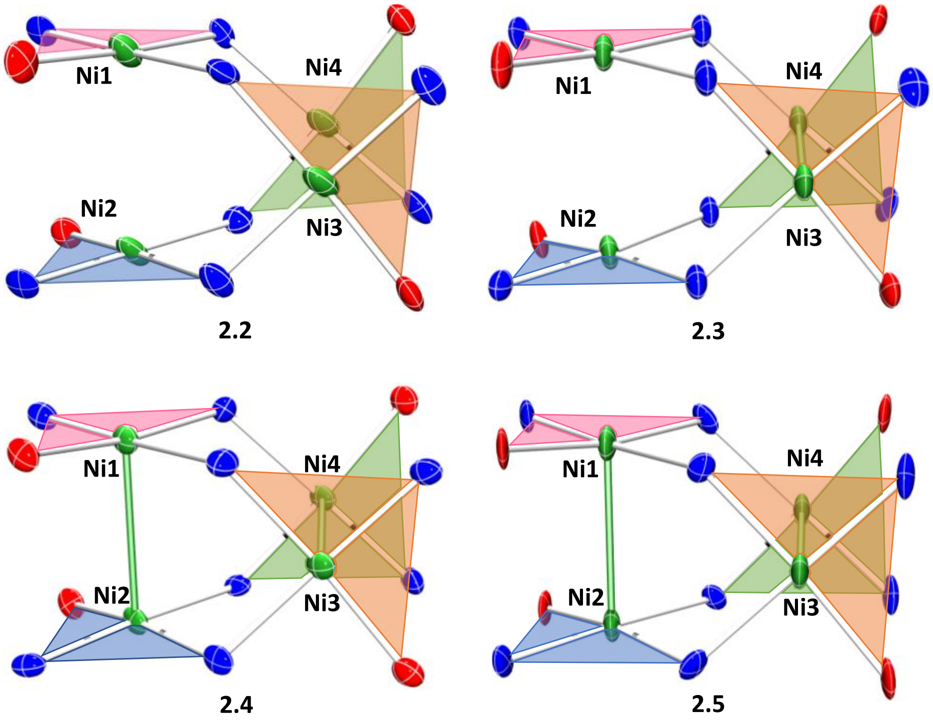

Figure 2.4. Drawn-in ligand planes for **2.2**, **2.3**, **2.4**, and **2.5** tetranuclear cores.

The significant shortening of the Ni3–Ni4 distance is consistent with the formation of a long, formal half bond expected from the removal of a single e^- from an *e*-symmetric σ* orbital located along the Ni3–Ni4 vector (Figure 2.5),[18, 19, 32] using a simplified D_{2d}-symmetric tetranuclear model and ignoring extensive ligand π mixing. An overall spin of ½, determined by the Evans method, further confirmed this assignment.[33] In addition, analysis of **2.3** by EPR spectroscopy in DCM at 100 K revealed a rhombic spectrum with significant g tensor anisotropy modeled as: $g_x = 2.01$, $g_y = 2.22$, $g_z = 2.32$, and $g_{av} = 2.18$ (Figure 2.6), consistent with previously reported Ni-centered oxidation events.[3, 4, 19]

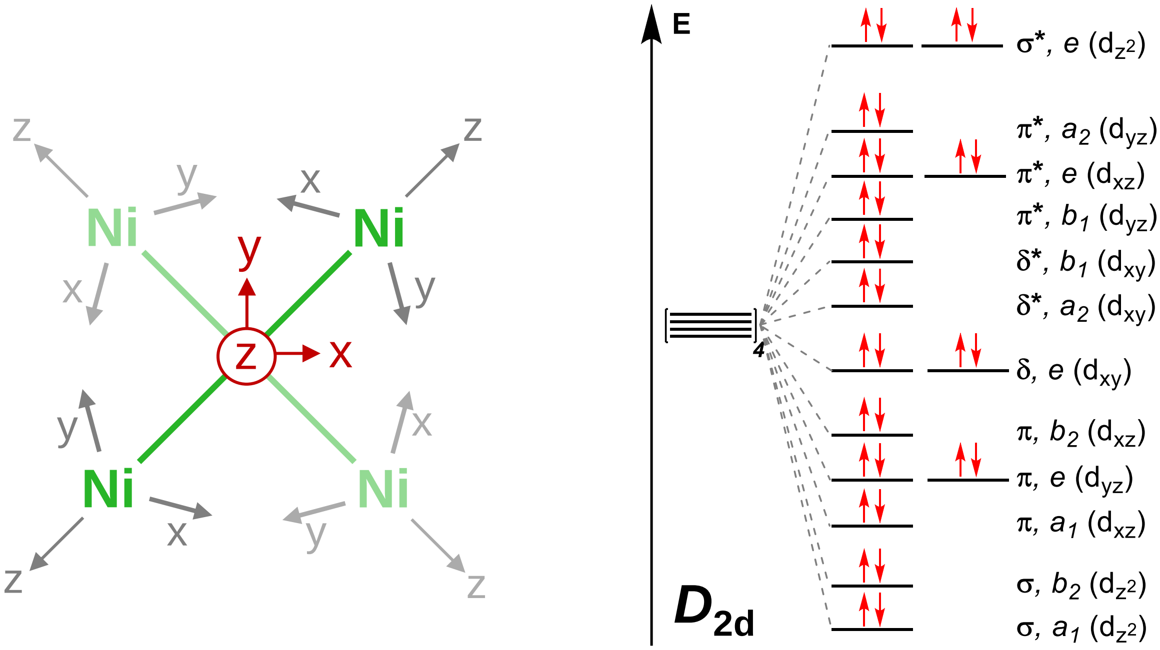

Figure 2.5. Partial d-orbital splitting diagram for a D_{2d} tetrametallic core, ignoring ligand π interactions.

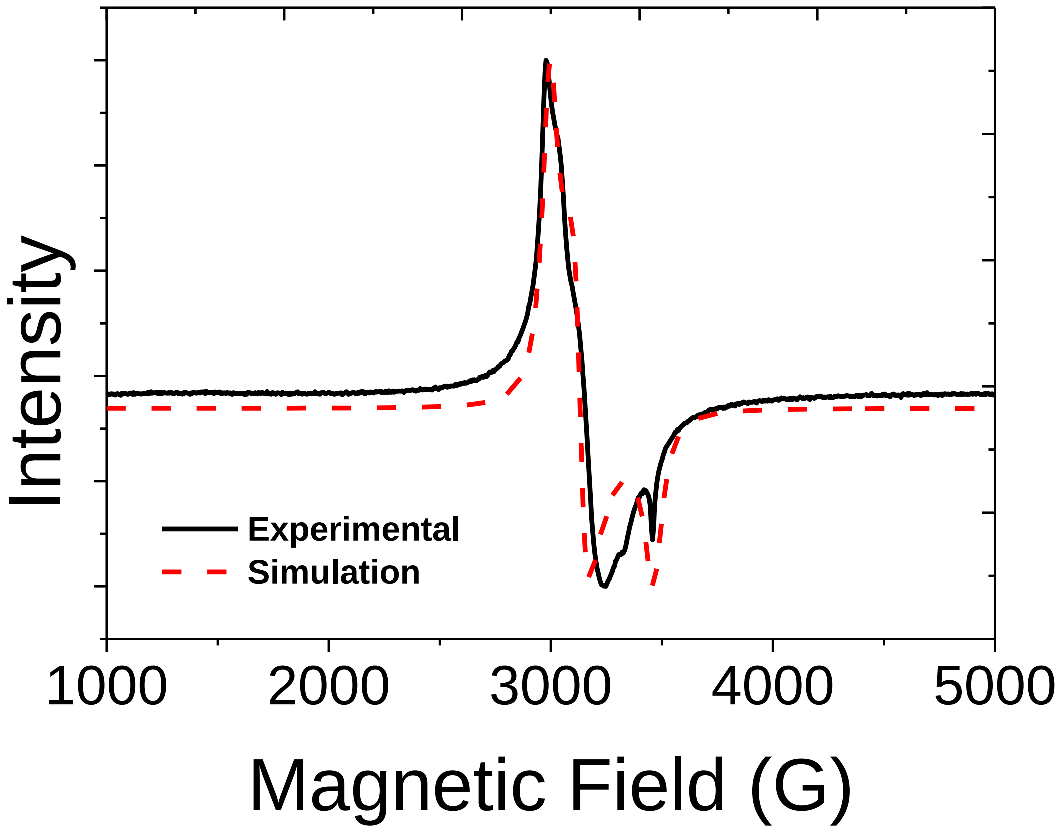

Figure 2.6. Experimental (black trace) and simulated (red trace) EPR spectrum of **2.3** in DCM at 100 K. Simulation gave following g-values: $g_x = 2.01$, $g_y = 2.22$, $g_z = 2.32$, and $g_{av} = 2.18$.

While the UV-Vis absorption spectrum of **2.3** is similar to **2.2**, a distinct absorption in the NIR at 1300 nm (ε = 3277 M^{-1} cm^{-1}) is observed for **2.3** (Figure 2.7) which we tentatively assign as a charge transfer band (based on its high ε),[19, 34] likely a ligand-to-metal charge transfer (LMCT) due to the oxidized Ni center. A comproportionation constant (K_c) of ~ 2 × 10^7, obtained from the difference in the first two $E_{1/2}$ values,[35] supports a Robin-Day Class III fully delocalized system, with resulting Ni3(2.5)–Ni4(2.5) oxidation states in **2.3** (oxidation states in parentheses).

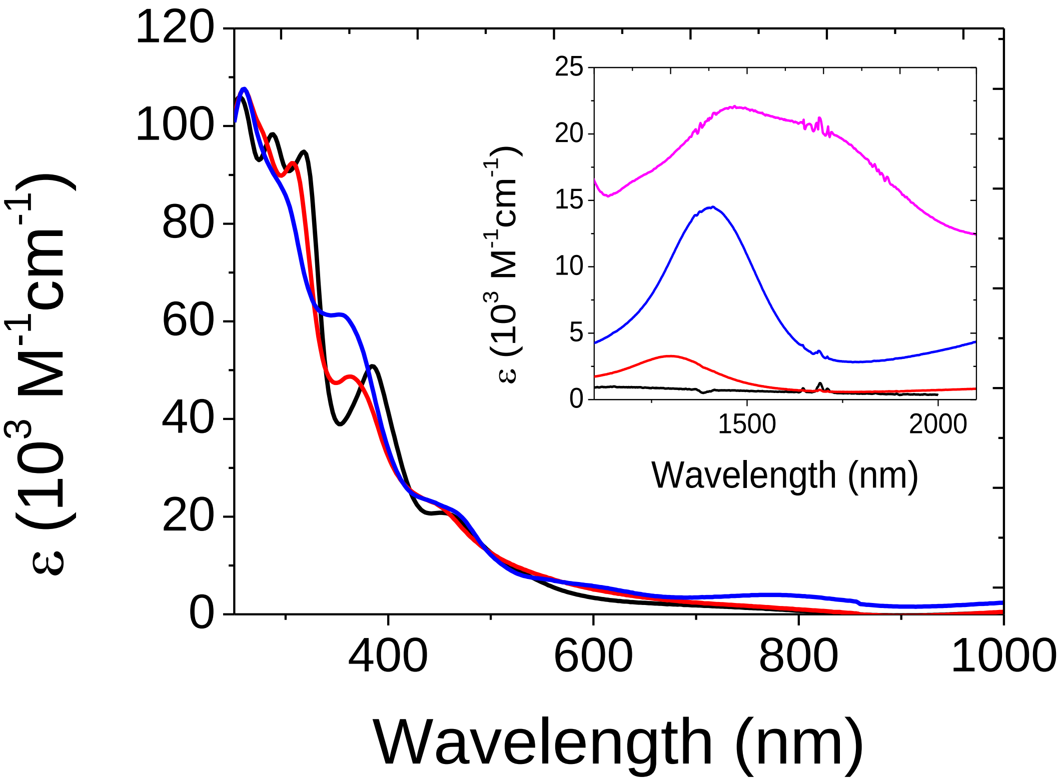

Figure 2.7. UV-visible spectrum of **2.2** (0.068 mM, black trace), **2.3** (0.088 mM, red trace), **2.4** (0.089 mM, blue trace) in DCM. Inset: NIR spectrum of **2.2** (0.115 mM, black trace), **2.3** (0.396 mM, red trace), **2.4** (0.216 mM, blue trace), and *in-situ* generated **2.5** (0.426 mM, pink trace) in DCM. The **2.5** complex was generated by treating **2.2** to 10 equiv of [(2,4-$C_6H_3Br_2)_3N][B(C_6F_5)_4]$. The **2.5** UV-Vis is omitted due to the strong absorptions of the oxidant ([(2,4-$C_6H_3Br_2)_3N][B(C_6F_5)_4]$) saturating the detector.

The di-oxidized product was obtained by treating **2.2** with two equivalents of the ammoniumyl oxidant, [(2, 4-$Br_2C_6H_3)_3N][B(C_6F_5)_4]$ to yield $[L_2Ni_4][B(C_6F_5)_4]_2$ (**2.4**; Scheme 2.1).[36] Single crystals suitable for XRD studies were obtained by layering hexanes on a concentrated DCM solution of **2.4** at -40 °C (Figure 2.8). The solid-state structure revealed contracted Ni1–Ni2

(2.7095(18) Å) and Ni3–Ni4 (2.6284(18) Å) distances with

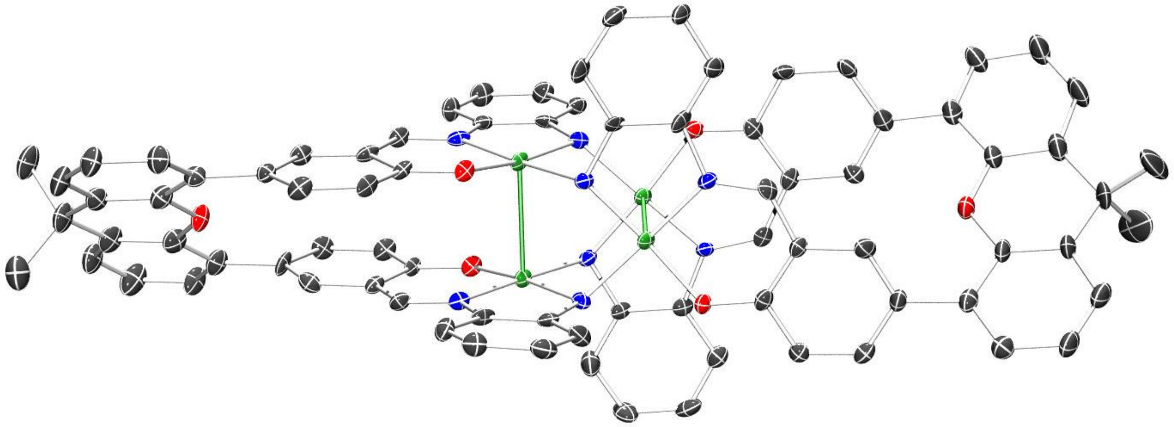

Figure 2.8. Solid-state molecular structure of **2.4**. Solid green bond represents long Ni–Ni bond. Hydrogen atoms, co-crystallized solvent molecules, and counteranions are removed for clarity (C, black; N, blue; O, red; Ni, green).

corresponding protrusions of the Ni centers from the mean tridentate ligand planes (Table 1, Figures 2.4 and 2.8). These observed contractions are consistent with the removal of an electron from each of the *e*-degenerate σ* orbitals, with each being localized at the separate Ni1–Ni2 and Ni3–Ni4 vectors, forming two Ni(II)-Ni(III) linkages with formal half-bonds in each (Figure 2.5). The resulting expected *S* = 1 spin state was confirmed by magnetic measurements of **2.4** performed by SQUID magnetometry (Figure 2.9A and B). For this measurement, a purity check for ferromagnetic impurities was performed by measuring the magnetic moment against the change in magnetic field at 10 K (Figure 2.9A). Magnetic

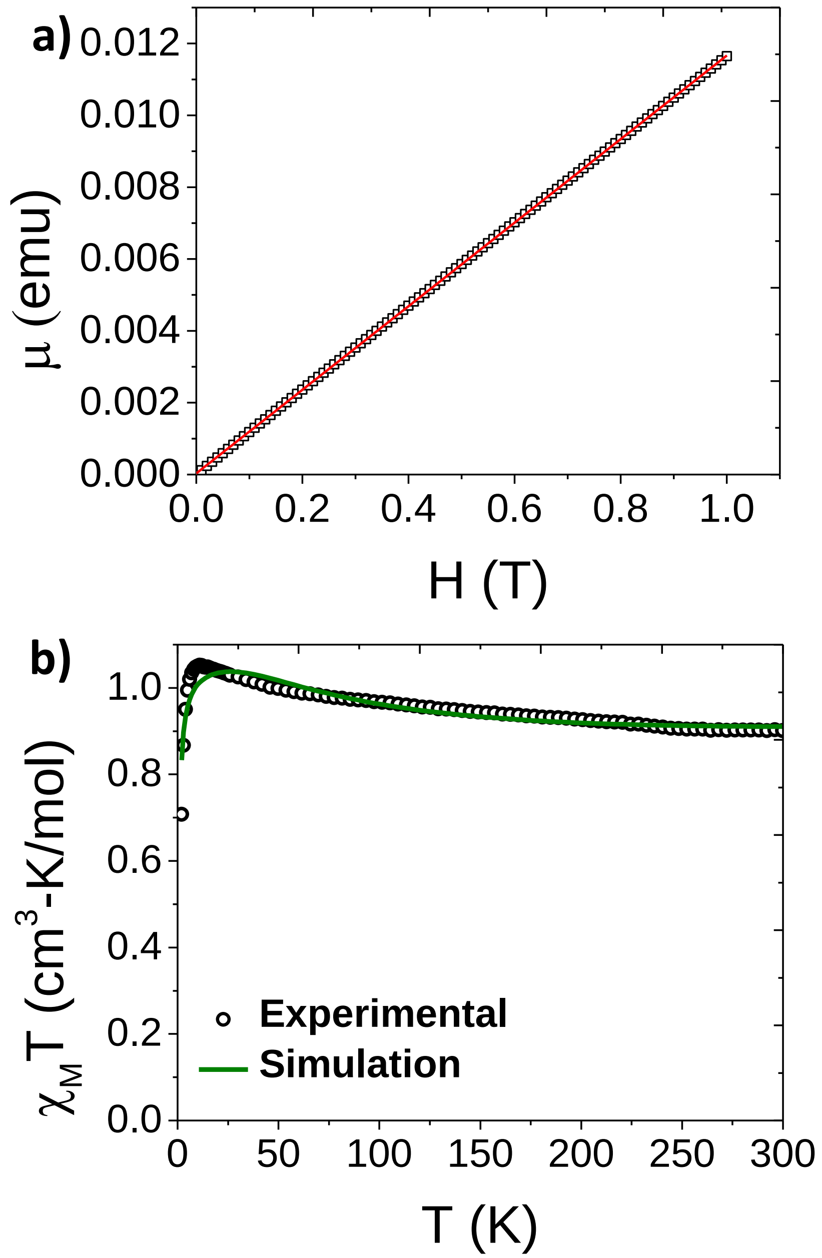

Figure 2.9. (a) Magnetic moment vs magnetic field at 10 K for **2.4** used to check for ferromagnetic impurities. (b) Molar magnetic susceptibility ($\chi_M T$) versus T measurements for bulk crystalline **2.4** collected from 2 to 300 K (black circles) under a static 0.1 T field. The green trace represents the simulated fit with parameters: *g*-value = 2.06; J_{12} = 36.2 cm^{-1}, D = 2.16 cm^{-1}, E = 0.70 cm^{-1}, TIP = 177x10^{-6} cm^{-3}mol^{-1}, and zJ = -0.135 cm^{-1}.

susceptibility (χ_MT) measurements for **2.4** were collected at variable temperatures (2−300 K) and revealed a plateauing average χ_MT value of 0.95 in the 50-300 K range, consistent with an S = 1 manifold approximated by the general formula, $\chi_M T = [\sum S_i(S_i + 1)]/2$ (Figure 2.9B). A magnetic exchange value (*J*) of 36.2 $\mathrm{cm^{-1}}$ was obtained by fitting the data from 2-300 K and confirmed that significant ferromagnetic coupling between Ni centers is present, possibly due to super exchange through the bridging nitrogen atoms. This degree of magnetic exchange in polynuclear high-valent Ni species via super exchange is not unprecedented and even greater magnitudes have been reported.[30] The absorption spectrum revealed a red-shifted LMCT absorbance at 1410 nm (ε = 14,574 $\mathrm{M^{-1}cm^{-1}}$) in the NIR, the intensity of which is over four times as intense as the one in **2.3** (Figure 2.7). Lastly, a K_c value of ~ 2 x 10^5, obtained from the difference in the two highest $E_{1/2}$ values,[35] suggests a more localized electronic structure consistent with a Robin-Day Class II system.

The isolation of the tetra-oxidized species was achieved by treating **2.2** to 10 equiv of $[(2,4\text{-}Br_2C_6H_3)_3N][B(C_6F_5)_4]$ to yield $[L_2Ni_4][B(C_6F_5)_4]_4$ (**2.5**; Scheme 1). Single crystals suitable for XRD studies were obtained by layering hexanes on a concentrated DCM solution of **2.5** at -40 °C (Figure 2.10). Similar to **2.4**, both Ni–Ni distances are contracted relative to **2.2**, and concurrent protrusions of the Ni centers from the mean ligand tridentate planes are observed (Table 1, Figures 2.4 and 2.10). However, these effects are less pronounced than in the dicationic **2.4**, and we attribute this distinction to the increased electrostatic repulsion between cationic metal centers in **2.5** relative to **2.4**.[17, 37] Attempts to obtain magnetic measurements of **2.5** were hampered by its extreme instability (*vide infra*). Nonetheless, the ^{1}H NMR spectrum of *in situ*-generated **2.5** revealed a paramagnetic species, likely arising from thermal population of a higher spin state (Figure 2.5). The absorption spectrum of *in* *situ*-generated **2.5** revealed an intense (ε = 22099 M^{-1} cm^{-1}) red-shifted LMCT band in the NIR at 1468 nm along with a significant shoulder centered at 1662 nm (ε = 20751 $M^{-1}cm^{-1}$), significantly more intense than those observed for **2.3** and **2.4** (Figure 2.7).

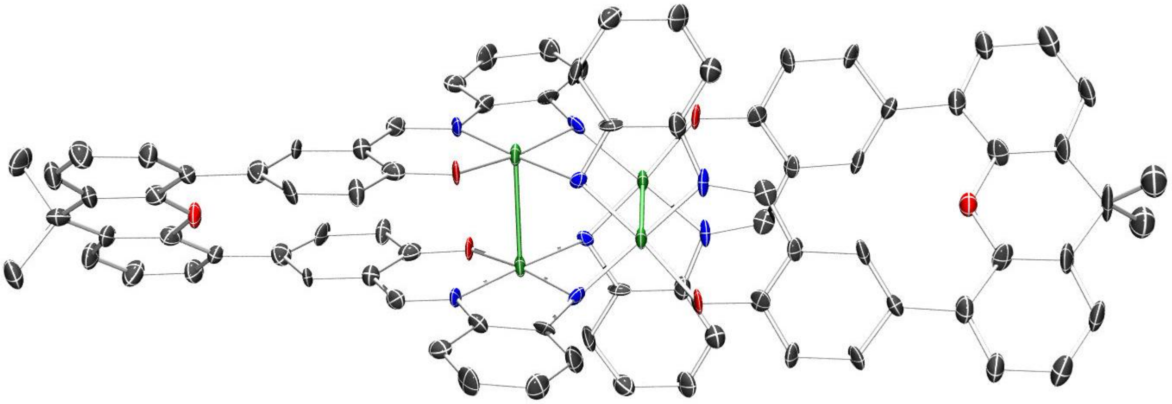

Figure 2.10. Solid-state molecular structure of **2.5**. Solid green bond represents long Ni–Ni bond. Hydrogen atoms, co-crystallized solvent molecules, and counteranions are removed for clarity (C, black; N, blue; O, red; Ni, green;). The unit cell consists of a half-fragment of **2.5** and two full $[B(C_6F_5)_4]^-$ fragments. The former is grown for clarity.

Due to its highly reactive nature, **2.5** readily decomposes to **2.4** during and after the reaction workup thereby complicating a thorough characterization. Therefore, we performed DFT calculations in order to shed light on its electronic structure and determine the locus of oxidation. Calculations were first performed on the neutral **2.2** species at the B3PW91 level of theory to validate the computational method. The optimized structure (Figure 2.11A) is in good agreement with the experimental one with the Ni–Ni distances reproduced to within 0.05 Å for the singlet spin state (all Ni(II)). Wiberg Bond Indexes (WBI) are found to be very small for the Ni–Ni interactions (0.08). In order to get insight into the locus of oxidation of **2.2**, the frontier orbitals were scrutinized. As can be seen (Figure 2.12), the HOMO (364) and HOMO-1(363) are mainly antibonding (σ*) Ni–Ni interactions (Figure 2.5), whereas the HOMO-2 (362) is mainly located on the ligand. Therefore, one would expect the first four oxidations to remove electrons from the HOMO and HOMO-1 which mainly occur at the Ni centers. Removing electrons from these two orbitals would lead to a decrease of the Ni–Ni antibonding interaction and a concurrent decrease in the Ni–Ni bond distance, as observed experimentally. In order to verify this assumption, calculations were performed on the $[Ni_4]^{4+}$ species, **2.5**. The optimized structure has a quintet spin state – confirming the observed

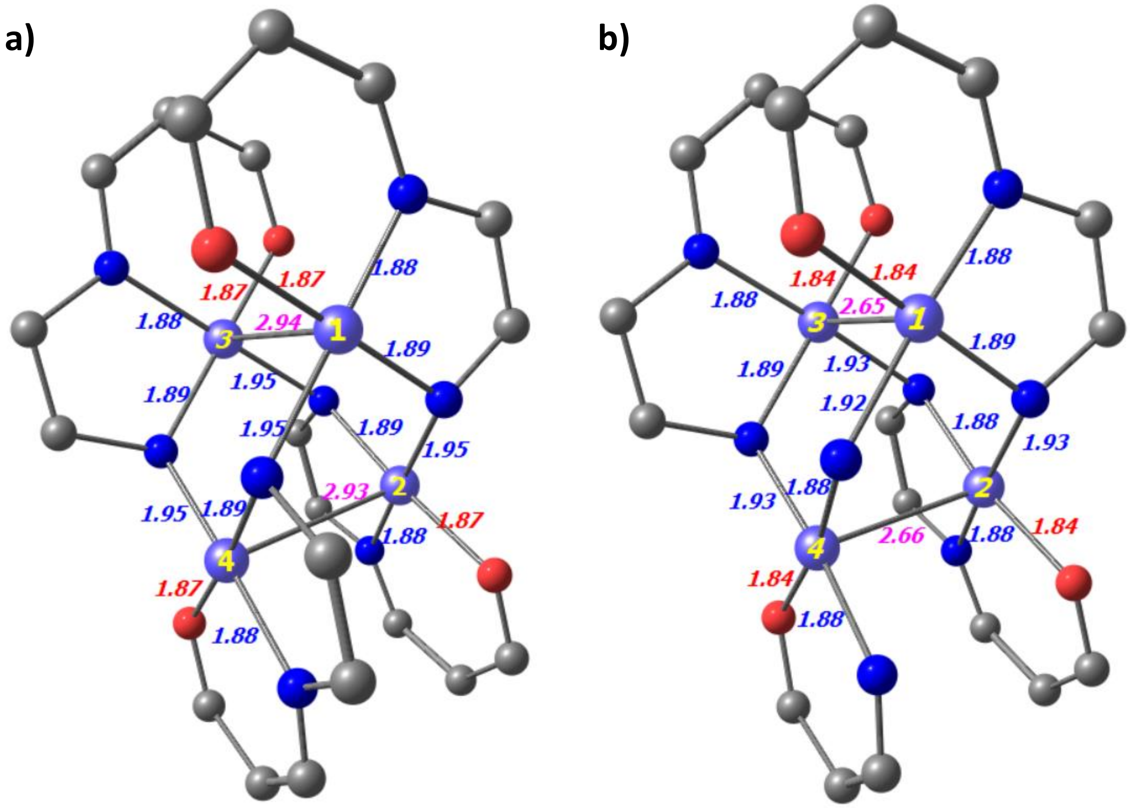

Figure 2.11. (a) Optimized structure of the **2.2** neutral species. (b) Optimized structure of the **2.5** species.

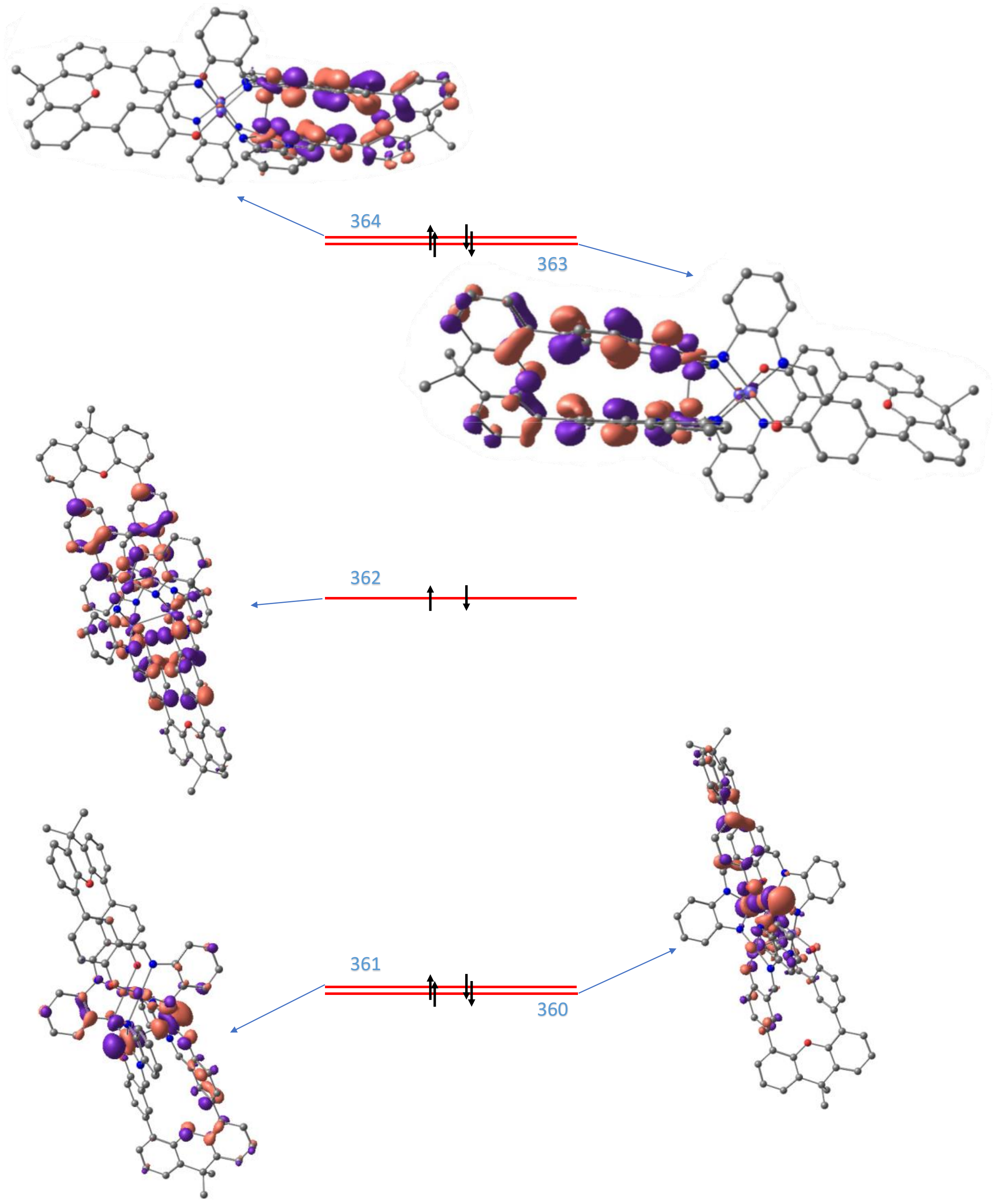

Figure 2.12. Simplified Frontier orbital diagram of the **2.2** complex.

paramagnetic nature of **2.5** (*vide supra*) – and is in good agreement with the experimental structure with the Ni–Ni distances reproduced to within 0.02 Å, roughly 0.2 Å shorter than in **2.2**. This is further highlighted by the increase of the WBI of the Ni–Ni interactions (0.2) indicating a stronger interaction. In order to assess the oxidation state of the Ni centers, the unpaired spin density was plotted (Figure 2.13). As can be seen, the unpaired spin density is primarily located on the Ni centers, with some contribution from the oxygen on the ligand, thus supporting our assignment as an all high-valent (all Ni(III)) multinuclear cluster in **2.5**.

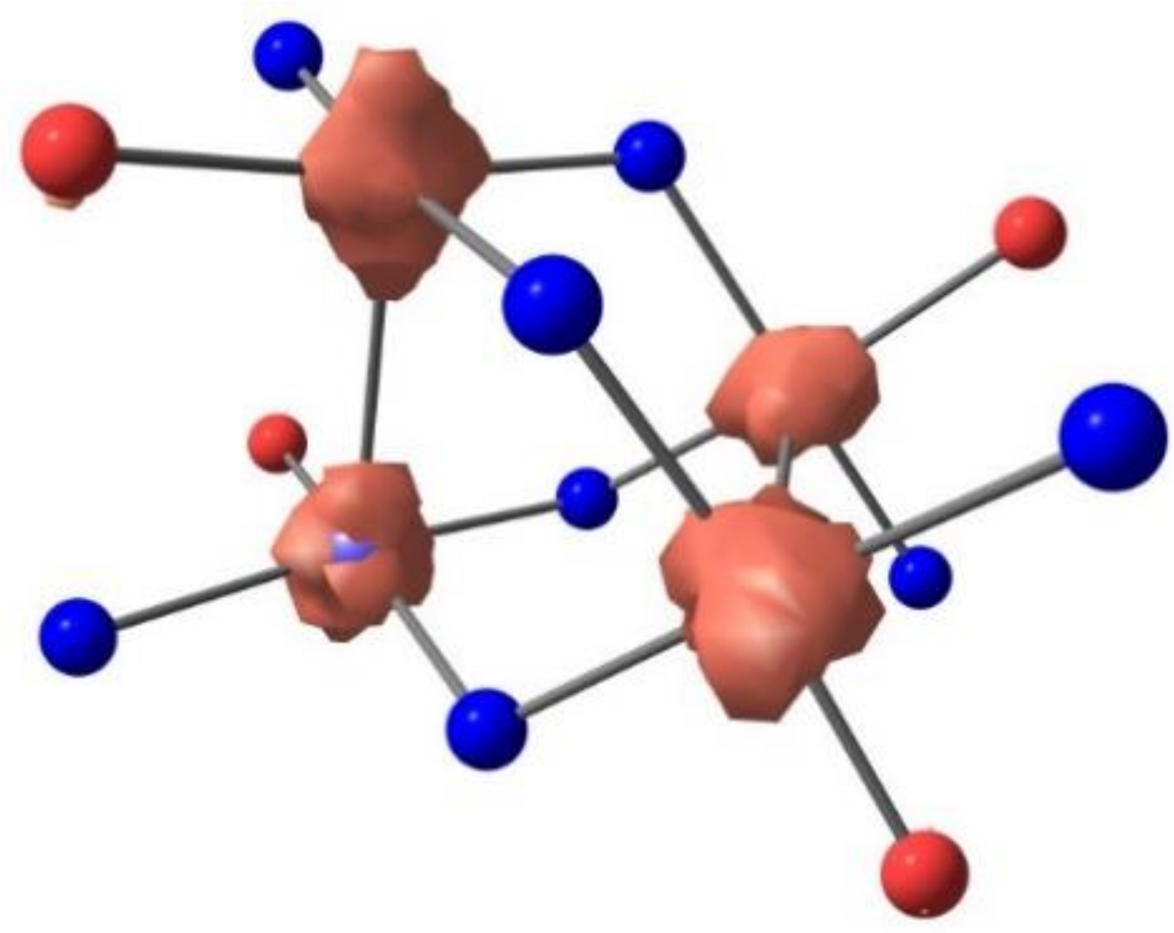

Figure 2.13. Unpaired spin density plot for **2.5**. The isocontour value is set to the default (0.03).

We would lastly like to acknowledge that o-phenylenediamine and Schiff base (*i.e.*, salen) derivatives are known redox-active ligands and experience distinct site-specific alterations in bond lengths at either Ni–N/O bonds, or within the ligand multiple bonds upon oxidation.[38-41] A thorough analysis of the bond lengths in the neutral **2.2**, as well as oxidized complexes **2.3-2.5**, revealed a general shortening of the Ni–E (E = N, O) bonds upon oxidation – expected from metal-based oxidations[3, 19] – but no discernable bond change patterns within the ligand π framework expected from ligand-based oxidation (Table 2.2, Figures 2.14-2.17 in appendix). With this, and together with our combined experimental and theoretical results above, we propose that **2.2** undergoes primarily metal-based oxidation events.

Table 2.2. Average bond lengths of immediate redox active ligand sites and Ni coordination sphere.

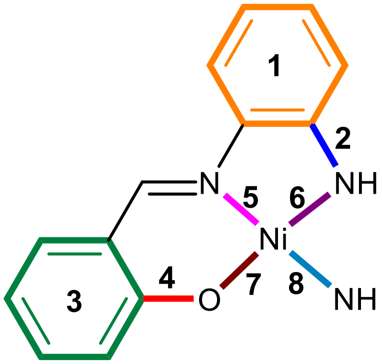

Compounds	**Average Bond Lengths (Å)**							
	Site 1	Site 2	Site 3	Site 4	Site 5	Site 6	Site 7	Site 8
2.2	1.395	1.455	1.404	1.309	1.876	1.896	1.854	1.949
2.3	1.379	1.436	1.397	1.328	1.867	1.890	1.841	1.926
2.4	1.383	1.438	1.438	1.296	1.866	1.884	1.830	1.912
2.5	1.385	1.444	1.405	1.307	1.867	1.878	1.836	1.921

2.3 Summary

In conclusion, a novel tetranuclear Ni species isolated in multiple high-valent states, including an all Ni(III) state, is reported and supported by spectroscopic, crystallographic, magnetometric, and computational data. In the following chapter, we explore potential applications of this cluster and its derivatives in mediating multi-electron transformations at small molecules of energy importance.

2.4 Experimental

2.4.1 General Considerations

Techniques and Reagents. All manipulations were performed under an atmosphere of dry N_2 by means of standard Schlenk or glovebox techniques (MBRAUN UNIlab Pro SP Eco equipped with a −40 °C freezer), unless stated otherwise. Hexanes and DCM (Fisher) were dried using an MBRAUN-Solvent Purification System and stored over activated 4 Å molecular sieves for 2 days prior to use. 1,1,2,2-Tetrachloroethane (TCE; Fisher) was degassed over 4 freeze-pump-thaw cycles and stored over 4 Å molecular sieves for 2 days prior to use. $Ni(OAc)_2{\bullet}4H_2O$, Acetone, Acetonitrile, and $[NO][PF_6]$ were all purchased from Fisher and used as received. Deuterated solvents were purchased from Cambridge Isotope Laboratories, then degassed, and stored over 4 Å molecular sieves for at least 2 days prior to use. Celite was dried by heating above 250 °C under dynamic vacuum for at least 48 h prior to use. 5,5'-(9,9-Dimethylxanthene-4,5-diyl)bis(salicylaldehyde)[31] and $[(2,4\text{-}C_6H_3Br_2)_3N][B(C_6F_5)_4]$[36] were prepared according to literature procedures.

Spectroscopic Measurements. NMR spectra were obtained on Agilent Technologies 400 and 600 MHz spectrometers, and referenced to residual solvent or externally (^{19}F, $CFCl_3$). Chemical shifts (δ) are recorded in ppm, and the coupling constants are in Hz. Elemental analyses (C, H, N) were recorded at the University of California, Berkeley using a PerkinElmer 2400 Series II combustion analyzer. UV−vis−NIR spectroscopy was performed using a Perkin Elmer Lambda 750 UV/VIS spectrometer with 1 mm quartz cuvettes with a teflon seal and 1 cm IR quartz cuvettes with a screwcap top. Perpendicular-mode X-band EPR spectra were collected on a Bruker EMX EPR Spectrometer equipped with an Oxford ESR

900 liquid nitrogen cryostat. Data acquisition was collected at 100K in frozen DCM. EPR data was simulated using the program PHI.[42]

Magnetic Measurements. Solution magnetic moment determinations were performed by the Evans method using 1,2-difluorobenzene as residual solvent.[33] Solid-state magnetic measurements were collected using a Quantum Design MPMS SQUID magnetometer in the RSO mode. The sample was prepared in the glovebox. Magnetic susceptibility data was corrected for diamagnetism of the sample, estimated using Pascal's constants.[43] $\chi_M T$ data was fit using the exchange Hamiltonian, $\widehat{H}_{ex} = -2\sum_{i=1}^{ns-1}\sum_{j=i+1}^{ns} J_{ij}\, S_i S_j$, where J_{ij} are the exchange coupling constants of spins i and j, and ns is the number of spins. SQUID data was fit using the program PHI.[42]

Electrochemical Measurements. Cyclic voltammetry was performed on a CH Instruments 630E electrochemical analysis potentiostat, equipped with a 3 mm diameter glassy carbon working electrode, a Ag wire pseudo-reference electrode, and a Pt wire counter electrode in a conventional three-electrode cell. TCE was used as the solvent for electrochemical measurements with [Bu$_4$N][PF$_6$] (0.1 M) as the supporting electrolyte. The glassy carbon working electrode was cleaned prior to each experiment by polishing with 1, 0.3, and 0.05 mm alumina (CH Instruments) in descending order, followed by a water and acetone solvent rinse and finally sonication in acetone for 2 min. The potential of the pseudo-reference was referenced to the Fc/Fc$^+$ redox couple.

2.4.2 Syntheses

LH_4. A 50 mL round bottom flask was charged with 5,5'-(9,9-Dimethylxanthene-4,5-diyl)bis(salicylaldehyde)[31] (400 mg, 0.8879 mmol), *o*-phenylenediamine (960.2 mg, 8.879 mmol), and ethanol (25 mL). The reaction was refluxed for 4 hours open to atmosphere. After a few minutes the reactants went into solution and formed a deep orange color. Eventually, yellow precipitates were formed. After reflux, the reaction was allowed to cool to room temperature and was filtered. The yellow product was washed with 200 mL of ethanol and dried under vacuum. Yield: 470 mg (83.9%). NMR: ^{1}H NMR (400 MHz, $CDCl_3$): δ 13.28 (s, 2H, OH), 8.05 (s, 2H, HC=N), 7.43 (dd, J = 8 Hz, 4 Hz, 2H), 7.23 (dd, J = 12 Hz, 4 Hz, 2H), 7.17-7.06 (m, 8H), 6.86-6.79 (m, 8H), 4.51 (s, 4H, NH), 1.74 (s, 6H, Me). $^{13}C\{^1H\}$ NMR (101 MHz, $(CD_3)_2CO$): δ 162.47, 160.38, 148.18, 143.32, 135.73, 135.39, 133.49, 131.61, 130.16, 129.16, 128.90, 128.69, 126.00, 124.08, 120.03, 119.34, 118.18, 116.94, 116.39, 35.40, 32.35. MS (ESI(+), MeCN) *m/z*: $[M + H]^+$ 631.3.

L_2Ni_4 ($[Ni_4]$). To a 50 mL round bottom flask was added a magnetic stir bar, **LH_4** (592 mg, 0.9386 mmol), $Ni(OAc)_2 \cdot 4H_2O$ (477 mg, 1.9169 mmol), and 25 mL of ethanol. The reaction was refluxed for 5 hrs. Upon heating, the powders went into solution and the color changed into a deep red where red precipitates eventually form. After reflux, the reaction was removed from heat and allowed to cool to room temperature. The reaction was filtered over a fine frit. The red solids were washed with ethanol until the washings were colorless. Next the crude product was washed with water (2 x 10 mL), acetone (5 x 10 mL), and acetonitrile (5 x 10 mL). The red product was dried under high vacuum at 100 °C overnight before bringing into the glovebox. Yield: 349.1 mg (50%). X-ray quality crystals were grown by vapor diffusion of hexanes into a concentrated DCM solution of the product at room temperature. NMR. ^{1}H NMR (600 MHz, $CDCl_3$): δ. 8.80 (d, *J* = 6 Hz, 4H), 7.44-7.38 (m, 8H), 7.33 (s, 4H), 7.29 (s, 4H), 7.26-7.20 (m, 12H), 7.18-7.08 (m, 8H), 6.48 (d, *J* = 12, 4H), 1.75 (s, 12H), 1.40 (s, 4H, NH). $^{13}C\{^1H\}$ NMR (101 MHz, $(CD_3)_2CO$): δ 162.26, 152.02, 150.73, 147.09, 145.08, 136.47, 134.56, 130.49, 129.53, 128.19, 127.70, 127.43, 125.10, 123.77, 123.39, 121.64, 114.70, 34.67, 33.19, 30.16, 25.59. UV-vis [DCM, λ_{max}/nm, (ε/M^{-1} cm^{-1})]: 451 (20,779), 384 (50,754), 318 (94,775), 287 (98,306), 256 (105,915). MS (MALDI) *m/z*: 1484.342. Anal. Calcd. for $C_{82}H_{60}N_8Ni_4O_6$: C, 66.18; H, 4.06; N, 7.53. Found: C, 66.34; H, 3.83; N, 7.14.

$[L_2Ni_4][PF_6]$ ($[Ni_4]^+$). In the glovebox, a 20 mL scintillation vial was charged with 1 equiv of **$[Ni_4]$** (50.5 mg, 0.0339 mmol) and 2 mL of DCM. The slurry was frozen in the glovebox coldwell. To the frozen slurry was added 0.9 equiv of $NOPF_6$ (5.3 mg, 0.0303 mmol) slurried in 1 mL of DCM. The reaction vial was placed back in the coldwell to freeze again. The frozen reaction was placed on the stir plate to thaw and stirred at glovebox temperature for 4 hours at which point the reaction color had turned brown. The reaction was dried under vacuum. The reaction vial was washed with benzene over a celite plug eluting a red solution of unreacted **$[Ni_4]$**. Once the benzene washes were colorless, the plug was washed with DCM until the washings were colorless. The DCM was removed under vacuum to provide **$[Ni_4]^+$**. X-ray quality crystals were grown by vapor diffusion of hexanes over a concentrated DCM solution of the product in a -40 °C freezer. Yield: 46.4 mg (93.7 %). NMR. ^{1}H NMR (400 MHz, CD_2Cl_2) Note: resonances are broadened and paramagnetically shifted and integrations are therefore not assigned: δ 16.66 (s), 10.76 (d, *J* = 8 Hz), 10.12 (s), 8.73 (t, *J* = 8 Hz), 7.02 (d, *J* = 8 Hz), 4.70 (s), 3.85 (s), 3.21 (d, *J* = 8 Hz), 2.65 (d, *J* = 8 Hz), 1.86 (s), -4.69 (s), -

10.85 (s). ^{19}F NMR (376 MHz, CD_2Cl_2): δ -72.17 (d, J = 707.1 Hz). ^{31}P NMR (162 MHz, CD_2Cl_2): Silent. UV-Vis-NIR [DCM, λ_{max}/nm, (ε/M^{-1} cm^{-1})]: 1,300 (3,277), 436 sh (20,874), 363 (48,683), 306 (92,419), 278 sh (98,565) 260 (107,499). Anal. Calcd. for $C_{82}H_{60}F_6N_8Ni_4O_6P{\bullet}CH_2Cl_2$: C, 58.02; H, 3.64; N, 6.52. Found: C, 57.88; H, 3.62; N, 6.23.

$[L_2Ni_4][B(C_6F_5)_4]_2$ ($[Ni_4]^{2+}$). In the glovebox, a 20 mL scintillation vial was charged with **[Ni_4]** (50.6 mg, 0.0340 mmol) and 3 mL of DCM. The slurry was frozen in the glovebox coldwell. $[(2,4\text{-}Br_2C_6H_3)_3N][B(C_6F_5)_4]$ (95.2 mg, 0.0681 mmol) was added to the frozen slurry along with 1 mL of DCM to aid with the transfer. The reaction vial was placed back in the Coldwell to freeze again. Once frozen, the reaction was placed on the stir plate to thaw and stirred at glovebox temperature for 15 minutes. The reaction color turned dark brown. The solution was concentrated to 2 mL under vacuum and the product was crashed out of solution with 10 mL of hexanes and filtered over a celite plug. The plug was washed with 15 mL of benzene followed by 5 mL of hexanes. The product was eluted with DCM and dried under vacuum to yield 90.1 mg (93.1 %). X-ray quality crystals were grown by layering a concentrated DCM solution with hexanes in a -40 °C freezer. NMR. ^{1}H NMR (400 MHz, CD_2Cl_2) Note: resonances are broadened and paramagnetically shifted and integrations are therefore not assigned: δ 35.59, 21.09 7.87, 6.64 br, 4.21, 2.21, 1.80, -3.47, -15.32, -29.84, -80.66 br. ^{19}F NMR (376 MHz, CD_2Cl_2): δ 132.89 (bs, 16F), 163.01 (t, J = 18.8 Hz, 8F) , 166.70 (bs, 16F). UV-Vis-NIR [DCM, λ_{max}/nm, (ε/M^{-1} cm^{-1})]: 1410 (14,514), 778 (5,046), 542 sh (7,313), 454 (22,093), 352 (61,381), 294 sh (88,237), 260 (107,624). Anal. Calcd. for $C_{130}H_{60}B_2F_{40}N_8Ni_4O_6$: C, 54.86; H, 2.12; N, 3.94. Found: C, 54.89; H, 2.4; N, 4.08.

[L_2Ni_4][$B(C_6F_5)_4$]$_4$ ([Ni_4]$^{4+}$). In the glovebox, a 20 mL scintillation vial was charged with **[Ni_4] (**32 mg, 0.0215 mmol) and 3 mL of DCM. The slurry was frozen in the glovebox coldwell. To the frozen slurry was added [(2,4-$C_6H_3Br_2$)$_3$N][$B(C_6F_5)_4$] (292 mg, 0.2089 mmol) of as a solid and 1 mL of DCM was used to help transfer residual powder. The reaction vial was placed back in the coldwell to freeze. The frozen reaction was placed on the stir plate to thaw and stirred at glovebox temperature for 5 minutes. The solution color turned black. The solvent was removed under vacuum. The crude product was washed with benzene over a celite plug until the washings were colorless (~30 mL). Once the washings were colorless, the plug was washed with another 10 mL of benzene to ensure removal of the N(2,4-$C_6H_3Br_2$)$_3$ byproduct. The plug was subsequently washed with 5 mL of hexanes. The product was eluted with DCM and dried under vacuum to yield 77.3 mg (85.5%). X-ray quality crystals were grown by layering a concentrated DCM solution of the product with hexanes in a -40 °C freezer. NMR. ^{1}H NMR (400 MHz, CD_2Cl_2) Note: resonances are broadened and paramagnetically shifted and integrations are therefore not assigned: δ 18.25 br, 16.49 br, 14.36, 12.91, 10.26, 9.76, 8.08, 4.86, 4.21, 4.10, 3.00, 2.68, 2.00, 1.91, 1.89, 1.87, 1.85, 1.84, 1.74, 1.72, 1.43, -2.31, -3.61, -13.02 br, -15.59 br, -35.53 br. ^{19}F NMR (376 MHz, CD_2Cl_2): δ 132.58 (bs, 32F), 162.7 (bs, 16F), 165.82 (bs, 32F). Vis-NIR [DCM, λ_{max}/nm, (ε/M^{-1} cm^{-1})]: 1,468 (22,099), 1662 sh (20,751).

2.4.3 Computational Details

All calculations were carried out at the DFT level of theory using the hybrid functional B3PW91[44, 45] with the Gaussian 09[46] suite of programs. The Ni atom was represented with a Stuttgart-Dresden relativistic effective core potential associated with its adapted basis set.[47-

[49] All other atoms (C, H, O, N) were described with a 6-31G (d,p), double –ζ quality basis set. Geometry optimizations were computed without any symmetry constraints. The enthalpy energy was computed at T = 298 K in the gas phase. Natural Bonding Orbital (NBO) analyses were also conducted.[50, 51]

2.5 Appendix

2.4.1 Bond Lengths of Structures

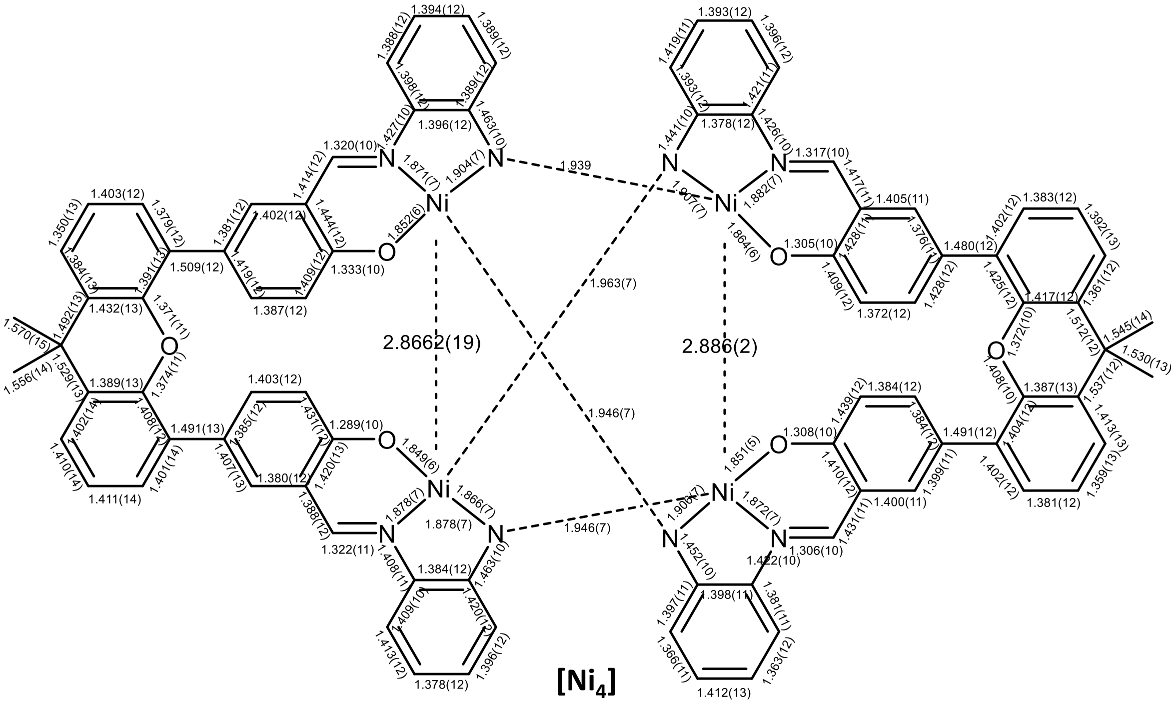

[Ni4]

Figure 2.14. Bond lengths for complex **2.2**.

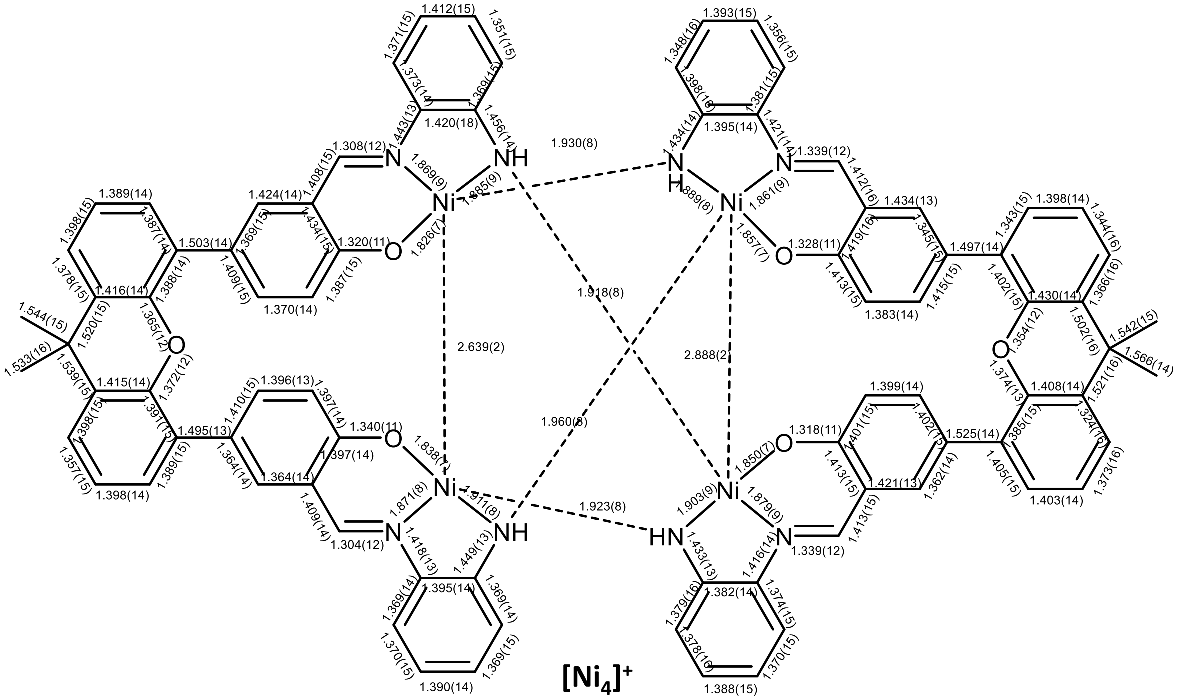

Figure 2.15. Bond lengths for complex **2.3**.

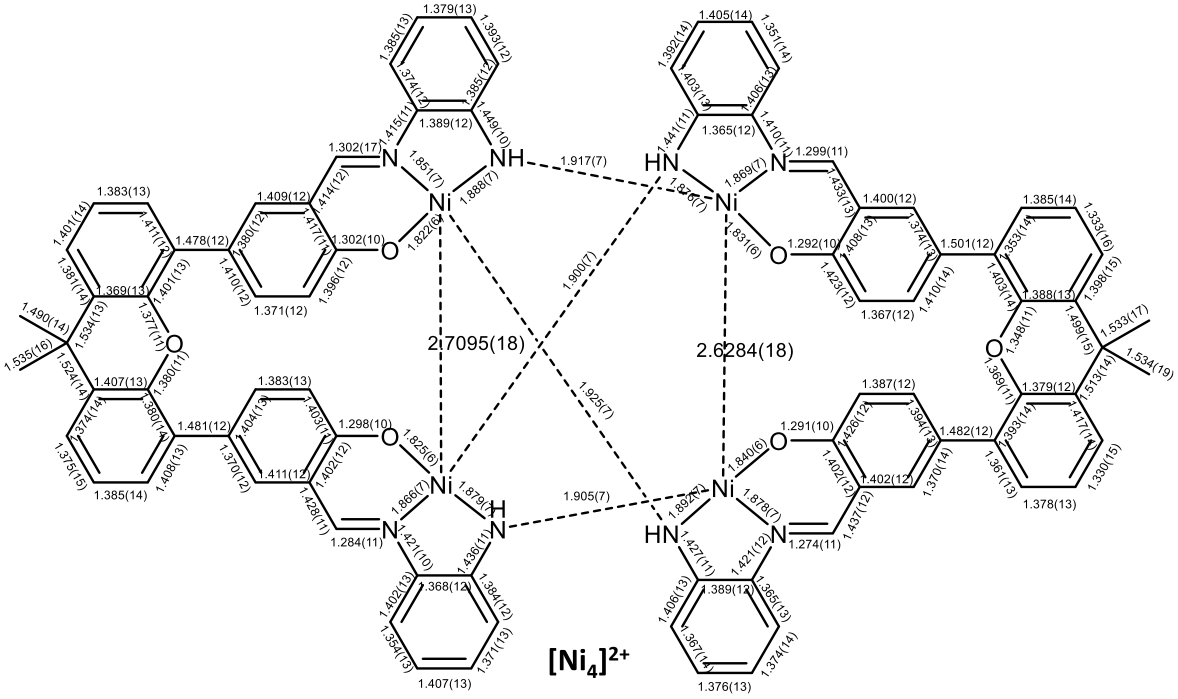

Figure 2.16. Bond lengths for complex **2.4**.

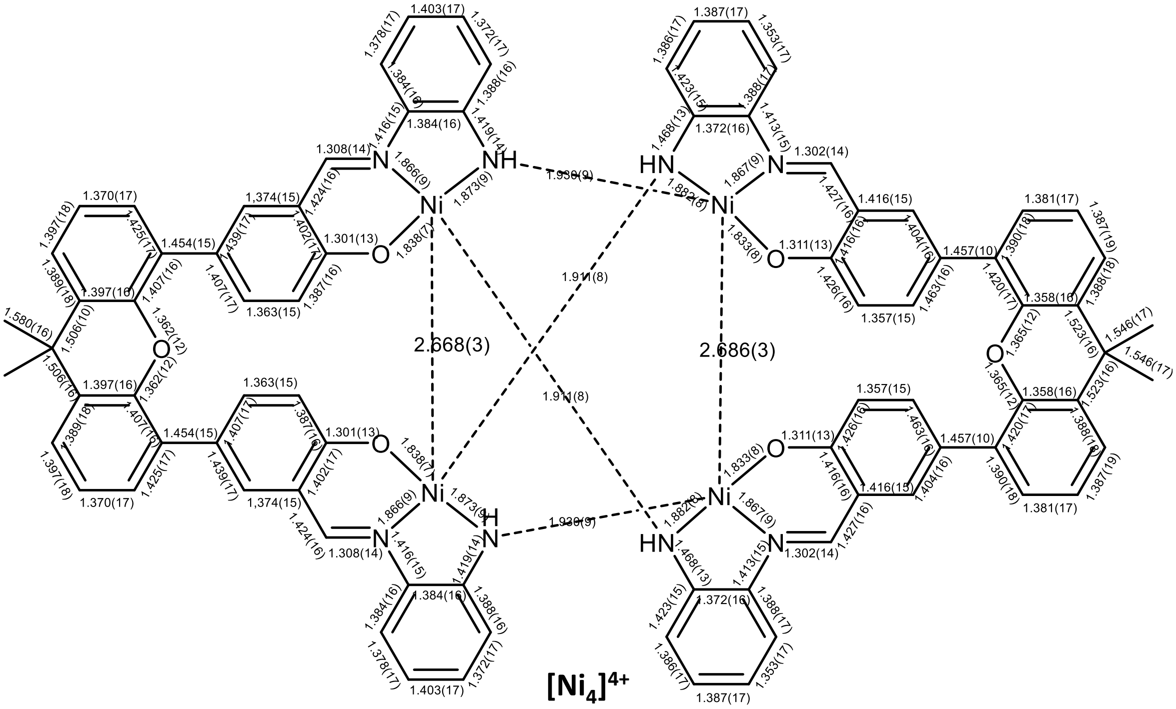

$[Ni_4]^{4+}$

Figure 2.17. Bond lengths for complex **2.5**.

2.6 References

1. Collins, T. J.; Nichols, T. R.; Uffelman, E. S., A square-planar nickel(III) complex of an innocent ligand system. *J. Am. Chem. Soc.* **1991,** *113* (12), 4708-4709.

2. Alonso, P. J.; Arauzo, A. B.; García-Monforte, M. A.; Martín, A.; Menjón, B.; Rillo, C.; Tomás, M., Homoleptic Organoderivatives of High-Valent Nickel(III). *Chem. Eur. J.* **2009,** *15* (41), 11020-11030.

3. Cao, T.-P.-A.; Nocton, G.; Ricard, L.; Le Goff, X. F.; Auffrant, A., A Tetracoordinated Phosphasalen Nickel(III) Complex. *Angew. Chem. Int. Ed.* **2013,** *53* (5), 1368–1372.

4. Eckshtain-Levi, M.; Orio, M.; Lavi, R.; Benisvy, L., Nickel(iii) complexes of di-amidato-di-phenolato ligands: effect of H-bonding. *Dalton Trans.* **2013,** *42* (37), 13323-13326.

5. Kouno, M.; Yoshinari, N.; Kuwamura, N.; Yamagami, K.; Sekiyama, A.; Okumura, M.; Konno, T., Valence Interconversion of Octahedral Nickel(II/III/IV) Centers. *Angew. Chem. Int. Ed.* **2017,** *56* (44), 13762-13766.

6. Iluc, V. M.; Miller, A. J. M.; Anderson, J. S.; Monreal, M. J.; Mehn, M. P.; Hillhouse, G. L., Synthesis and Characterization of Three-Coordinate Ni(III)-Imide Complexes. *J. Am. Chem. Soc.* **2011,** *133* (33), 13055-13063.

7. Rosen, B. M.; Quasdorf, K. W.; Wilson, D. A.; Zhang, N.; Resmerita, A.-M.; Garg, N. K.; Percec, V., Nickel-Catalyzed Cross-Couplings Involving Carbon−Oxygen Bonds. *Chem. Rev.* **2010,** *111* (3), 1346-1416.

8. Tasker, S. Z.; Standley, E. A.; Jamison, T. F., Recent advances in homogeneous nickel catalysis. *Nature* **2014,** *509*, 299.

9. Camasso, N. M.; Sanford, M. S., Design, synthesis, and carbon-heteroatom coupling reactions of organometallic nickel(IV) complexes. *Science* **2015,** *347* (6227), 1218-1220.

10. Zhou, W.; Schultz, J. W.; Rath, N. P.; Mirica, L. M., Aromatic Methoxylation and Hydroxylation by Organometallic High-Valent Nickel Complexes. *J. Am. Chem. Soc.* **2015,** *137* (24), 7604-7607.

11. Shiren, K.; Ogo, S.; Fujinami, S.; Hayashi, H.; Suzuki, M.; Uehara, A.; Watanabe, Y.; Moro-oka, Y., Synthesis, Structures, and Properties of Bis(μ-oxo)nickel(III) and Bis(μ-superoxo)nickel(II) Complexes: An Unusual Conversion

of a NiIII2(μ-O)2 Core into a NiII2(μ-OO)2 Core by H2O2 and Oxygenation of Ligand. *J. Am. Chem. Soc.* **2000,** *122* (2), 254-262.

12. Honda, K.; Cho, J.; Matsumoto, T.; Roh, J.; Furutachi, H.; Tosha, T.; Kubo, M.; Fujinami, S.; Ogura, T.; Kitagawa, T.; Suzuki, M., Oxidation Reactivity of Bis(μ-oxo) Dinickel(III) Complexes: Arene Hydroxylation of the Supporting Ligand. *Angew. Chem. Int. Ed.* **2009,** *48* (18), 3304-3307.
13. Diccianni, J. B.; Hu, C.; Diao, T., N−N Bond Forming Reductive Elimination via a Mixed-Valent Nickel(II)–Nickel(III) Intermediate. *Angew. Chem. Int. Ed.* **2016,** *55* (26), 7534-7538.
14. Diccianni, J. B.; Hu, C.; Diao, T., Binuclear, High-Valent Nickel Complexes: Ni−Ni Bonds in Aryl–Halogen Bond Formation. *Angew. Chem.* **2017,** *129* (13), 3689-3693.
15. Powers, D. C.; Ritter, T., Bimetallic Redox Synergy in Oxidative Palladium Catalysis. *Acc. Chem. Res.* **2012,** *45* (6), 840-850.
16. Powers, D. C.; Ritter, T., Bimetallic Pd(III) complexes in palladium-catalysed carbon–heteroatom bond formation. *Nat. Chem.* **2009,** *1* (4), 302-309.
17. Cotton, F. A.; Murillo, C. A.; Walton, R. A., *Multiple Bonds Between Metal Atoms*. 3rd ed.; Springer Science and Business Media Inc.: New York, NY, 2005.
18. Cotton, F. A.; Matusz, M.; Poli, R.; Feng, X., Dinuclear formamidinato complexes of nickel and palladium. *J. Am. Chem. Soc.* **1988,** *110* (4), 1144-1154.
19. Berry, J. F.; Bothe, E.; Cotton, F. A.; Ibragimov, S. A.; Murillo, C. A.; Villagrán, D.; Wang, X., Metal−Metal Bonding in Mixed Valence Ni25+ Complexes and Spectroscopic Evidence for a Ni26+ Species. *Inorg. Chem.* **2006,** *45* (11), 4396-4406.

20. Davidson, J. L.; Green, M.; Stone, F. G. A.; Welch, A. J., Formation of tetra- and trinuclear cluster complexes from tetracarbonylnickel and hexafluorobut-2-yne. Molecular structures of tris(hexafluorobut-2-yne)tetracarbonyltetranickel and cyclooctatetraene(hexafluorobut-2-yne)tricarbonyltrinickel. *J. Am. Chem. Soc.* **1975,** *97* (26), 7490-7492.

21. Efthymiou, C. G.; Raptopoulou, C. P.; Terzis, A.; Boča, R.; Korabic, M.; Mrozinski, J.; Perlepes, S. P.; Bakalbassis, E. G., A Systematic Exploration of Nickel(II)/Acetate/Di-2-pyridyl Ketone Chemistry: Neutral and Cationic Tetranuclear Clusters, and a Novel Mononuclear Complex. *Eur. J. Inorg. Chem.* **2006,** *2006* (11), 2236-2252.

22. Fondo, M.; Ocampo, N.; García-Deibe, A. M.; Vicente, R.; Corbella, M.; Bermejo, M. R.; Sanmartín, J., Self-Assembly of a Tetranuclear Ni4 Cluster with an S = 4 Ground State: The First 3d Metal Cluster Bearing a μ4-η2:η2-O,O Carbonate Ligand. *Inorg. Chem.* **2006,** *45* (1), 255-262.

23. Cotton, F. A.; Murillo, C. A.; Wang, Q., A tetranuclear nickel(II) cluster: bis[[mu]3-2,6-bis(methylamino)pyridine(2-)-[kappa]4N2:N1,N6:N6]bis[[mu]3-2,6-bis(methylamino)pyridine(1-)-[kappa]3N1:N2:N2]dichloridotetranickel(II). *Acta Cryatallogr. E* **2007,** *63* (7), m1905.

24. Lemes, M. A.; Brunet, G.; Pialat, A.; Ungur, L.; Korobkov, I.; Murugesu, M., Strong ferromagnetic exchange coupling in a {NiII4} cluster mediated through an air-stable tetrazine-based radical anion. *Chem. Commun.* **2017,** *53* (62), 8660-8663.

25. Berry, J. F.; Cotton, F. A.; Daniels, L. M.; Murillo, C. A., A Trinickel Dipyridylamido Complex with Metal−Metal Bonding Interaction: Prelude to

Polynickel Molecular Wires and Devices? *J. Am. Chem. Soc.* **2002,** *124* (13), 3212-3213.

26. North, T. E.; Thoden, J. B.; Spencer, B.; Dahl, L. F., Experimental/theoretical studies of the paramagnetic 52/53-electron triangular metal [Ni3(.eta.5-C5H5)3(.mu.3-S)2]n series (n = 1+, 0) containing weak metal-metal bonding interactions: Fenske-Hall MO analysis of the trimetal-antibonding frontier orbitals involved in the reversible redox-generated change in nickel-sulfur Ni3S2 core geometry. *Organometallics* **1993,** *12* (4), 1299-1313.

27. Huang, G.-C.; Hua, S.-A.; Liu, I. P.-C.; Chien, C.-H.; Kuo, J.-H.; Lee, G.-H.; Peng, S.-M., Further studies of [Ni4(DAniDANy)4] (DAniDANy2−=N,N’-bis-p-anisyl-2,7-diamido-1,8-naphthyridine) and its one-electron oxidation product: Metal-metal sigma bonding in Ni49+ complex. *Comptes Rendus Chimie* **2012,** *15* (2), 159-162.

28. Berry, J. F.; Cotton, F. A.; Lei, P.; Lu, T.; Murillo, C. A., Additional Steps toward Molecular Scale Wires: Further Study of Ni510/11+ Chains Embraced by Polypyridylamide Ligands. *Inorg. Chem.* **2003,** *42* (11), 3534-3539.

29. Lee, C.-M.; Chiou, T.-W.; Chen, H.-H.; Chiang, C.-Y.; Kuo, T.-S.; Liaw, W.-F., Mononuclear Ni(II)-Thiolate Complexes with Pendant Thiol and Dinuclear Ni(III/II)-Thiolate Complexes with Ni···Ni Interaction Regulated by the Oxidation Levels of Nickels and the Coordinated Ligands. *Inorg. Chem.* **2007,** *46* (21), 8913-8923.

30. Beissel, T.; Birkelbach, F.; Bill, E.; Glaser, T.; Kesting, F.; Krebs, C.; Weyhermüller, T.; Wieghardt, K.; Butzlaff, C.; Trautwein, A. X., Exchange and

Double-Exchange Phenomena in Linear Homo- and Heterotrinuclear Nickel(II,III,IV) Complexes Containing Six μ2-Phenolato or μ2-Thiophenolato Bridging Ligands. *J. Am. Chem. Soc.* **1996,** *118* (49), 12376-12390.

31. Hirotsu, M.; Ohno, N.; Nakajima, T.; Kushibe, C.; Ueno, K.; Kinoshita, I., Synthesis and characterization of xanthene-bridged Schiff-base dimanganese(iii) complexes: bimetallic catalysts for asymmetric oxidation of sulfides. *Dalton Trans.* **2010,** *39* (1), 139-148.

32. Berry, J. F., Two-Center/Three-Electron Sigma Half-Bonds in Main Group and Transition Metal Chemistry. *Acc. Chem. Res.* **2016,** *49* (1), 27-34.

33. Evans, D. F., 400. The determination of the paramagnetic susceptibility of substances in solution by nuclear magnetic resonance. *J. Chem. Soc.* **1959,** (0), 2003-2005.

34. Mustieles Marín, I.; Cheisson, T.; Singh-Chauhan, R.; Herrero, C.; Cordier, M.; Clavaguéra, C.; Nocton, G.; Auffrant, A., Electronic Structures of Mono-Oxidized Copper and Nickel Phosphasalen Complexes. *Chem. Eur. J.* **2017,** *23* (71), 17940-17953.

35. Zanello, P., *Inorganic Electrochemistry: Theory, Practice and Application*. The Royal Society of Chemistry: Cambridge, UK, 2003.

36. Lam, K.; Geiger, W. E., Anodic Oxidation of Disulfides: Detection and Reactions of Disulfide Radical Cations. *J. Org. Chem.* **2013,** *78* (16), 8020-8027.

37. Cotton, F. A.; Daniels, L. M.; Feng, X.; Maloney, D. J.; Matonic, J. H.; Murilio, C. A., The use of CoCl2(amidine)2 compounds in the synthesis of tetragonal lantern dicobalt compounds: synthesis, structures and theoretical studies of Co2(DPhF)4 and

the oxidized species [Co2(DPhBz)4]+ (DPhF = N,N′-diphenylformamidinate, DPhBz = N,N′-diphenylbenzamidinate). *Inorg. Chim. Acta* **1997,** *256* (2), 291-301.

38. Chaudhuri, P.; Verani, C. N.; Bill, E.; Bothe, E.; Weyhermüller, T.; Wieghardt, K., Electronic Structure of Bis(o-iminobenzosemiquinonato)metal Complexes (Cu, Ni, Pd). The Art of Establishing Physical Oxidation States in Transition-Metal Complexes Containing Radical Ligands. *J. Am. Chem. Soc.* **2001,** *123* (10), 2213-2223.

39. Bill, E.; Bothe, E.; Chaudhuri, P.; Chlopek, K.; Herebian, D.; Kokatam, S.; Ray, K.; Weyhermüller, T.; Neese, F.; Wieghardt, K., Molecular and Electronic Structure of Four- and Five-Coordinate Cobalt Complexes Containing Two o-Phenylenediamine- or Two o-Aminophenol-Type Ligands at Various Oxidation Levels: An Experimental, Density Functional, and Correlated ab initio Study. *Chem. Eur. J.* **2005,** *11* (1), 204-224.

40. Storr, T.; Wasinger, E. C.; Pratt, R. C.; Stack, T. D. P., The Geometric and Electronic Structure of a One-Electron-Oxidized Nickel(II) Bis(salicylidene)diamine Complex. *Angew. Chem. Int. Ed.* **2007,** *46* (27), 5198-5201.

41. Clarke, R. M.; Jeen, T.; Rigo, S.; Thompson, J. R.; Kaake, L. G.; Thomas, F.; Storr, T., Exploiting exciton coupling of ligand radical intervalence charge transfer transitions to tune NIR absorption. *Chem. Sci.* **2018,** *9* (6), 1610-1620.

42. Chilton, N. F.; Anderson, R. P.; Turner, L. D.; Soncini, A.; Murray, K. S., PHI: A powerful new program for the analysis of anisotropic monomeric and exchange-coupled polynuclear d- and f-block complexes. *J. Comput. Chem.* **2013,** *34* (13), 1164-1175.

43. Bain, G. A.; Berry, J. F., Diamagnetic Corrections and Pascal's Constants. *J. Chem. Educ.* **2008,** *85* (4), 532-536.

44. Becke, A. D., Density-functional thermochemistry. III. The role of exact exchange. *J. Chem. Phys.* **1993,** *98* (7), 5648-5652.

45. Burke, K.; Perdew, J. P.; Wang, Y., In *Electronic Density Functional Theory: Recent Progress and New Directions*, Dobson, J. F.; Vignale, G.; Das, M. P., Eds. Plenum: New York, 1998.

46. *Gaussian 09*; *Revision D.01*; Frisch, M. J.; Trucks, G. W.; Schlegel, H. B.; Scuseria, G. E.; Robb, M. A.; Cheeseman, J. R.; Scalmani, G.; Barone, V.; Mennucci, B.; Petersson, G. A.; Nakatsuji, H.; Caricato, M.; Li, X.; Hratchian, H. P.; Izmaylov, A. F.; Bloino, J.; Zheng, G.; Sonnengerg, J. L.; Hada, M.; Ehara, M.; Toyota, K.; Fukuda, R.; Hasegawa, J.; Ishida, M.; Nakajima, T.; Honda, Y.; Kitao, O.; Nakai, H.; Vreven, T.; Montgomery Jr, J. A.; Peralta, J. E.; Ogliaro, F.; Bearpark, M.; Heyd, J. J.; Brothers, E.; Kudin, K. N.; Staroverov, V. N.; Keith, T.; Kobayashi, R.; Normand, J.; Raghavachari, K.; Rendell, A.; Burant, J. C.; Iyengar, S. S.; Tomasi, J.; Cossi, M.; Rega, N.; Millam, N. J.; Klene, M.; Knox, J. E.; Cross, J. B.; Bakken, V.; Adamo, C.; Jaramillo, J.; Gomperts, R.; Stratmann, R. E.; Yazyev, O.; Austin, A. J.; Cammi, R.; Pomelli, C.; Ochterski, J. W.; Martin, R. L.; Morokuma, K.; Zakrzewski, V. G.; Voth, G. A.; Salvador, P.; Dannenberg, J. J.; Dapprich, S.; Daniels, A. D.; Farkas, Ö.; Foresman, J. B.; Ortiz, J. V.; Cioslowski, J.; Fox, D. J., Gaussian, Inc., Wallingford CT, 2010.

47. Cao, X.; Dolg, M., Segmented contraction scheme for small-core actinide pseudopotential basis sets. *J. Mol. Struct. THEOCHEM* **2004,** *673* (1), 203-209.

48. Küchle, W.; Dolg, M.; Stoll, H.; Preuss, H., Energy-adjusted pseudopotentials for the actinides. Parameter sets and test calculations for thorium and thorium monoxide. *J. Chem. Phys.* **1994,** *100* (10), 7535-7542.

49. Cao, X.; Dolg, M.; Stoll, H., Valence basis sets for relativistic energy-consistent small-core actinide pseudopotentials. *J. Chem. Phys.* **2003,** *118* (2), 487-496.

50. Weinhold, F., In *Encyclopedia of Computational Chemistry*, Schleyer, P. v. R., Ed. JohnWiley & Sons: Chichester, 1998; p 1972.

51. Reed, A. E.; Curtiss, L. A.; Weinhold, F., Intermolecular interactions from a natural bond orbital, donor-acceptor viewpoint. *Chem. Rev.* **1988,** *88* (6), 899-926.

Chapter 3

The Synthesis, Characterization, Electrochemistry, and Reactivity of a Series of Tetranuclear Nickel Clusters

3.1 Introduction

High-valent nickel complexes are rare and multi-metallics (# of Ni ≥ 2) are even more uncommon. Only a handful of polynuclear high-valent nickel complexes have been reported with crystallographic evidence. To the best of our knowledge there are currently 9 examples of polynuclear nickel complexes containing at least one high-valent nickel center.[1-9] Even more scarce are polynuclear complexes containing a Ni(III)–Ni(III) bond, for which there are currently two examples including our previous report (Chapter 2).[4, 9] Previously we reported a tetranuclear nickel cluster (Scheme 3.1) that could be oxidized to a formal tetra-Ni(III) state.[9] A suite of characterization including electrochemistry, absorbance spectroscopy, SQUID magnetometry, and DFT calculations supported metal localized oxidation with minor ligand contribution in the all Ni(III) state. The Ni_4 cluster was unusual such that the ligand framework contains Schiff base and phenoxide chelation sites which are known to be redox active for salen and salphen nickel complexes. As such we were interested in perturbing the redox properties of the nickel cluster by modifying the o-phenylenediamine motifs with varying electron donating groups (EDG) and electron withdrawing groups (EWG). In tandem, we also studied the reactivity of the cluster's higher valent states for the oxidation of ammonia and water.

Heterogeneous nickel catalysts have been extensively studied for splitting NH_3 to N_2 and H_2 at high temperature and pressure.[10, 11] Nickel complexes have also been shown to be capable of oxidizing H_2O to O_2 and performing PCET reactions with small molecules, including ammonia.[12-20] Performing a $6e^-$ oxidation reaction of NH_3 at a single nickel site at a reasonable overpotential is challenging; however, we reasoned that the tetranuclear cluster could provide an interesting oxidative response in the presence of NH_3.

3.2 Results and Discussion

3.2.1 Synthesis and Structural Characterization

In Chapter 2, we discussed the synthesis and structural characterization of **3.1** (Scheme 3.1, Table 3.1). Following similar procedures, we synthesized novel pacman ligands and Ni_4 analogs with varying ligand substitutions (Scheme 3.1). Ligand $^{Me}LH_4$ was synthesized by refluxing 5,5'-(9,9-

Scheme 2. Synthesis of Ni_4 clusters with varying functional groups.

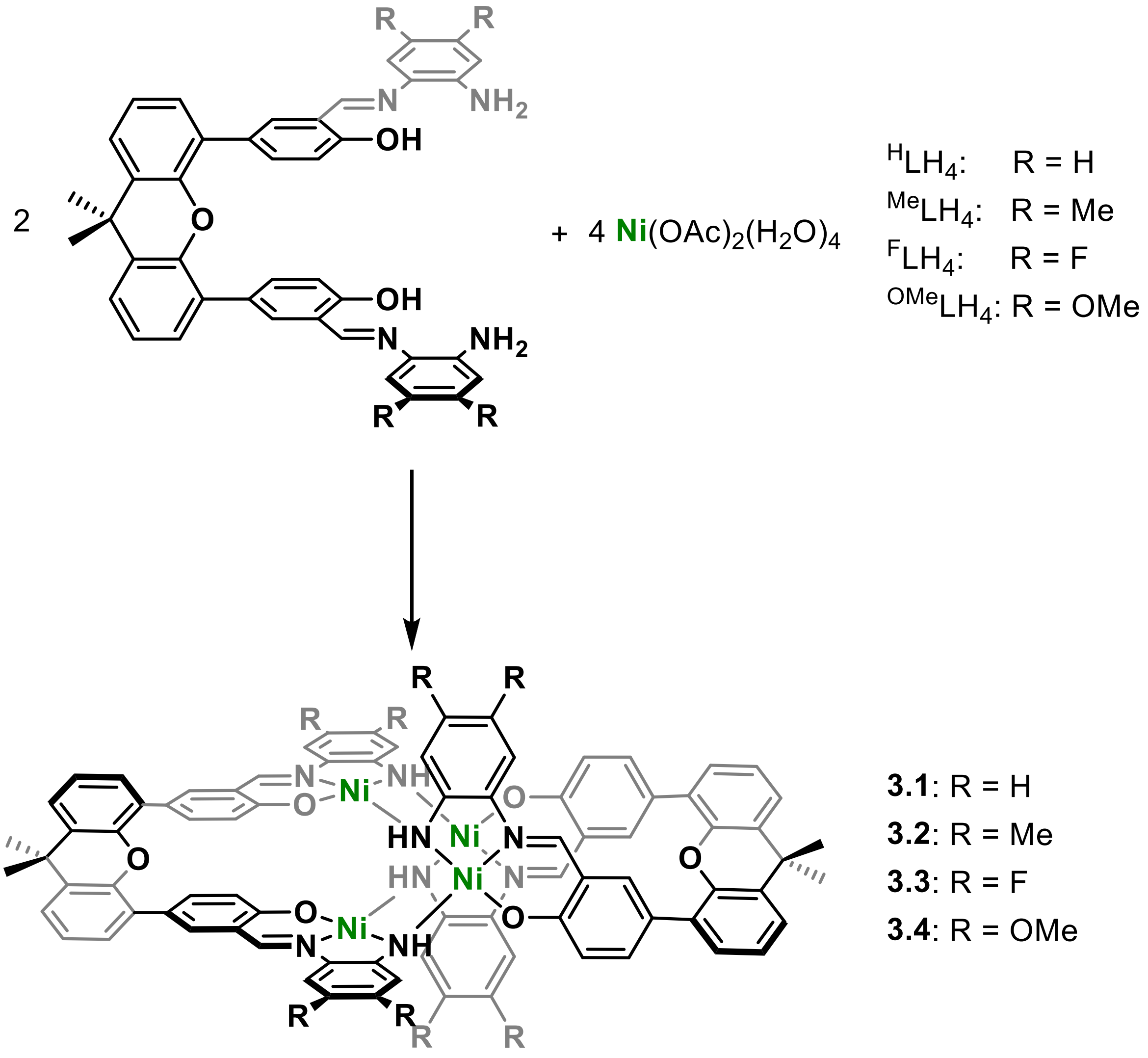

dimethylxanthene-4,5-diyl)bis(salicylaldehyde) with 10 equivalents of 4,5-dimethyl-1,2-diaminobenzene in ethanol overnight open to air (Scheme 3.1). An orange product precipitated from the reaction mixture and was isolated in 91% yield after purification. Refluxing $^{Me}LH_4$ in ethanol with 2 equivalents of $Ni(OAc)_2•4H_2O$ overnight provided the red product **3.2** in 53% yield after purification (Scheme 3.1). Similar to **3.1**, compound **3.2** displayed expected diamagnetic resonances in the NMR spectrum. X-ray quality crystals were grown by vapor diffusion of hexanes into a concentrated DCM solution at room temperature. The structural features of **3.2** were similar to that of **3.1** with Ni1–Ni2 and Ni3–Ni4 distances of 2.853(2) Ã and 2.862(4) Ã respectively (Figure 3.1, Table 3.1).

Table 3.1. Ni–Ni and Ni–mean plane distances obtained from single-crystal XRD studies

	Ni–Ni distance (Å)			**Ni–mean plane distance (Å)**[a]					**Xanthene Angle (°)**
	Ni1–Ni2	Ni3–Ni4	Avg	Ni1	Ni2	Ni3	Ni4	Avg	
3.1	2.8662(19)	2.886(2)	2.876	0.065	0.055	0.080	0.064	0.066	176.3
3.2	2.853(2)	2.862(4)	2.858	0.087	0.051	0.069	0.053	0.065	165.1
3.3	2.8403(19)	2.8602(19)	2.8503	0.077	0.062	0.101	0.064	0.076	147.5
3.4	2.8232(15)	2.8686(14)	2.8459	0.113	0.095	0.083	0.073	0.091	172.8
3.1^{2+}	2.7095(18)	2.6284(18)	2.6689	0.114	0.139	0.140	0.131	0.131	166.4
3.2^{2+}	2.715(2)	2.652(2)	2.684	0.120	0.079	0.106	0.133	0.110	158.5

[a]Method for measure the Ni–mean plane distance is described in Chapter 2. [b]Method for measuring the xanthene angle bend is illustrated in Figure 3.4.

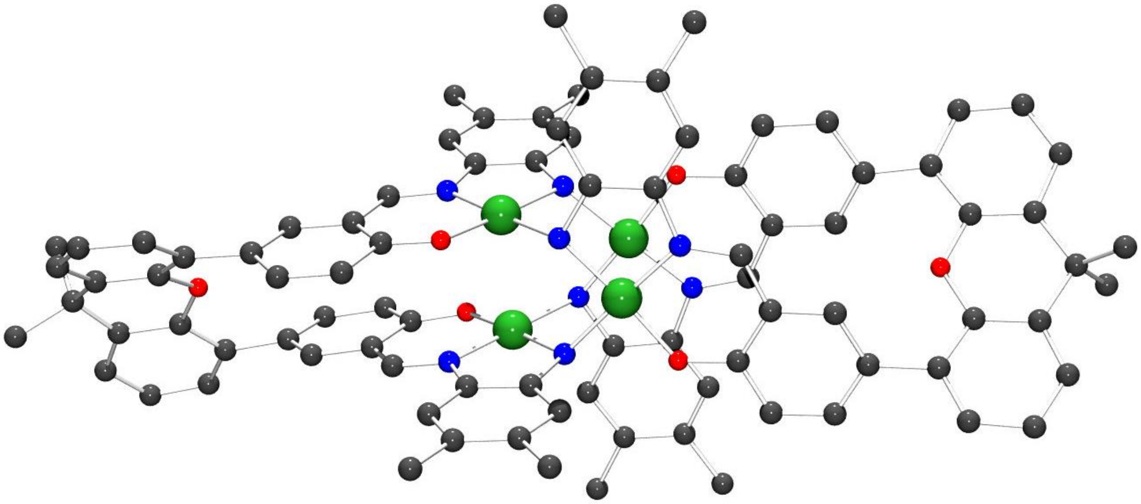

Figure 3.1. Solid-state molecular structure of **3.2**. Hydrogen atoms and co-crystallized solvent molecules were removed for clarity (C, black; N, blue; O, red; Ni, green).

Ligand $^{\mathbf{F}}\mathbf{LH_4}$ was synthesized by refluxing 5,5'-(9,9-dimethylxanthene-4,5-diyl)bis(salicylaldehyde) with 10 equivalents of 4,5-difluoro-1,2-diaminobenzene in ethanol overnight open to air (Scheme 3.1). A green product precipitated from the reaction mixture and was isolated in 66% yield after purification. Reflux of $^{\mathbf{F}}\mathbf{LH_4}$ in ethanol with 2 equivalents of $Ni(OAc)_2{\bullet}4H_2O$ overnight provided the red product **3.3** in 50% yield after purification (Scheme 3.1). Compound **3.3** displayed expected diamagnetic resonances in the NMR spectrum. X-ray quality crystals were grown by vapor diffusion of hexanes into a concentrated benzene solution at room temperature. The solid state structure of **3.3** features Ni1–Ni2 and Ni3–Ni4 distances of 2.8403(19) Ã and 2.8602(19) Ã respectively (Figure 3.2, Table 3.1).

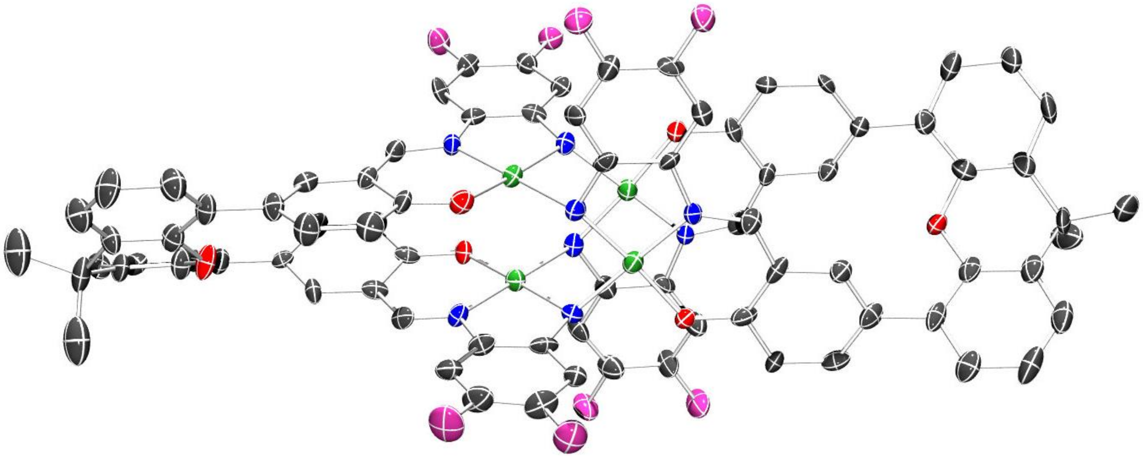

Figure 3.2. Solid state molecular structure of **3.3**. Hydrogen atoms and co-crystallized solvent molecules were removed for clarity (C, black; N, blue; O, red; Ni, green; F, violet-red).

Ligand $^{\mathbf{OMe}}\mathbf{LH_4}$ was synthesized by stirring 5,5’-(9,9-dimethylxanthene-4,5-diyl)bis(salicylaldehyde) with 10 equivalents of 4,5-dimethoxy-1,2-diaminobenzene in ethanol overnight under nitrogen (Scheme 3.1). A yellow product precipitated from the reaction mixture and was isolated in 72% yield after purification. Reflux of $^{\mathbf{OMe}}\mathbf{LH_4}$ in ethanol with 2 equivalents of $Ni(OAc)_2$•$4H_2O$ overnight provided the red product **3.5** in 50% yield after purification (Scheme 3.1). Compound **3.4** displayed expected diamagnetic resonances in the NMR spectrum. X-ray quality crystals were grown by vapor diffusion of hexanes into a concentrated DCM solution at room temperature. The solid state structure of **3.4** features Ni1–Ni2 and Ni3–Ni4 distances of 2.8232(15) Ǻ and 2.8686(14) Ǻ respectively (Figure 3.3, Table 3.1).

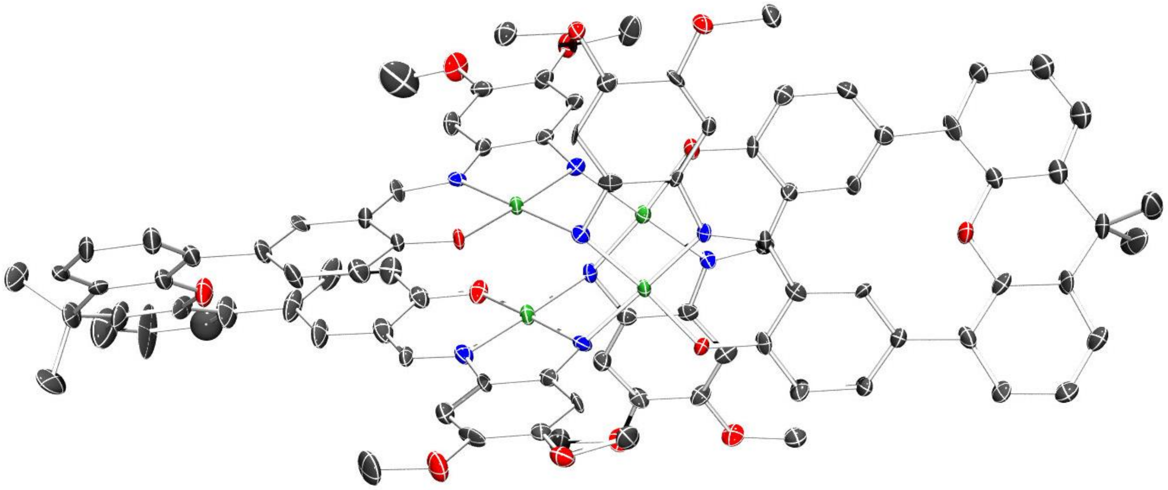

Figure 3.3. Solid state molecular structure of **3.4**. Hydrogen atoms and co-crystallized solvent molecules were removed for clarity (C, black; N, blue; O, red; Ni, green).

From Table 3.1, the Ni–Ni distances between **3.1**-**3.4** do not seem to follow any trends regarding changes between more electron donating or withdrawing groups on the aromatic rings of the ligand. However, the average Ni–Ni distances in **3.3** (2.8503 Å) and **3.4** (2.8459 Å) are distinctly shorter than the average Ni–Ni distances in **3.1** (2.876 Å) and **3.2** (2.858 Å). This trend is also observed in the measured Ni–mean ligand plane distances (Table 3.1). The average Ni–mean ligand plane distances in **3.3** and **3.4** were 0.076 Å and 0.091 Å while **3.1** and **3.2** revealed average distances of 0.066 Å and 0.065 Å respectively.

To evaluate possible ligand strain induced by the 1,2-diaminobenzene substituents, we measured the bending angle of the xanthene ligand groups in **3.1**-**3.4** (Table 3.1). An illustrative example how this was measured is depicted in Figure 3.4.

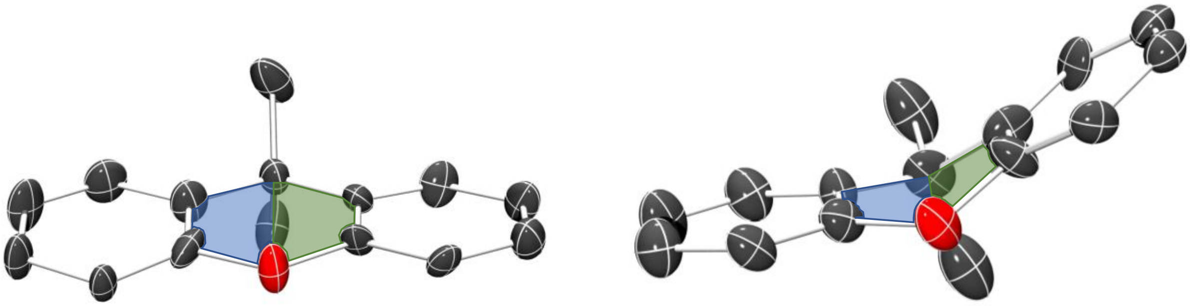

3.1 **3.3**

Figure 3.4. Drawn-in ligand xanthene planes for **3.1** and **3.3** used to calculate the bend angles described in Table 3.1.

For compound **3.1**, the average xanthene ring angles were almost flat at 176.3°. Compound **3.4** did deviate far from **3.1** featuring average xanthene ring angles of 172.8°. Compounds **3.2** and **3.3** deviate the most from the original compound with xanthene ring angles of 165.1° and 147.5° respectively. While the angle difference in **3.2** is slight, **3.3** feature a significantly large bend in the ring.

3.2.2 Electrochemistry of Ni_4 Clusters in Dichloromethane

The electrochemistry of **3.1** in DCM was described in Chapter 2 and is depicted in Figure 3.5 with redox values provided in Table 3.2. Cyclic voltammetry of **3.2** in DCM revealed three reversible oxidation events in a 1:1:2 e^- ratio at 0.118, 0.570, and 0.875 V vs. Fc^+/Fc respectively (Figure 3.5), which are cathodically shifted by 130, 86, and 57 mV respectively

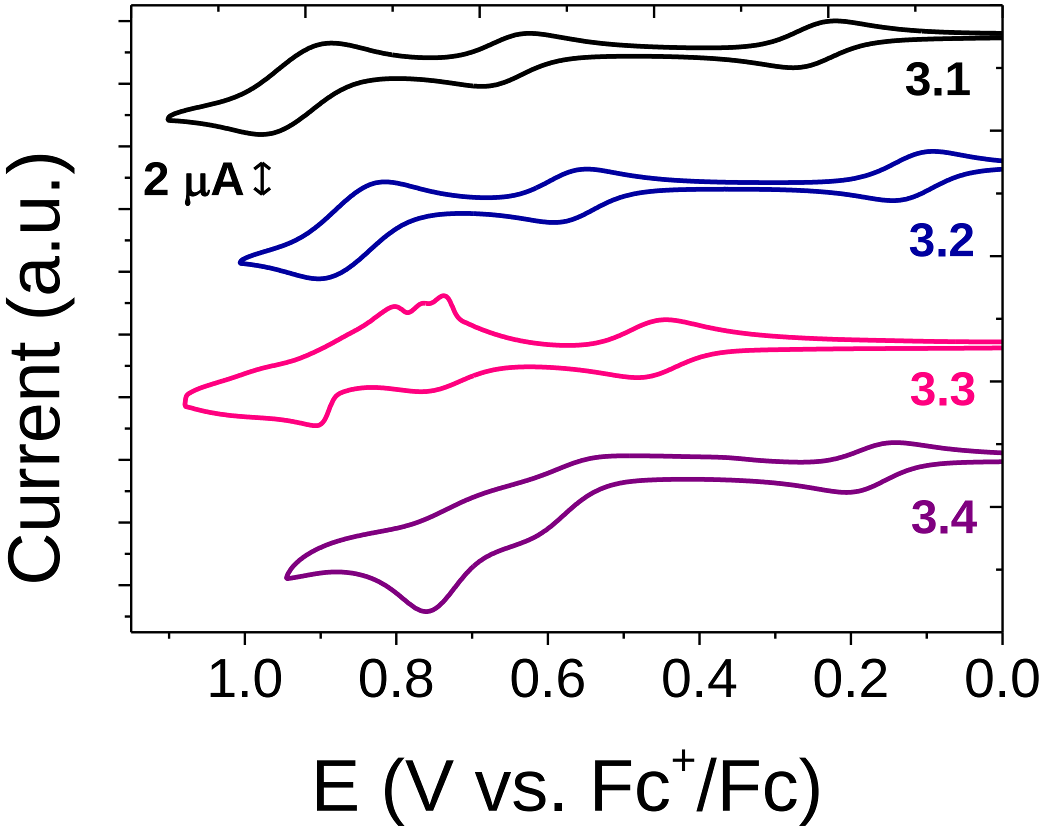

Figure 3.5. Stacked CVs of **3.1** (black trace), **3.2** (blue trace), **3.3** (pink trace), and **3.4** (purple trace) in DCM at 10 mV/s scan rates (0.43 mM [Ni_4], 0.1 M [Bu_4N][PF_6] supporting electrolyte, glassy carbon working electrode, Pt wire counter electrode, and Ag wire pseudo-reference electrode).

Table 3.2. Oxidation potential of compounds **3.1**-**3.4** in DCM.

Compounds	Oxidation Potentials in Dichloromethane (V vs. Fc^+/Fc)		
	1st (1 e^-)	2nd (1 e^-)	3rd (2 e^-)
3.1	0.248	0.656	0.932
3.2	0.118	0.570	0.875
3.3	0.464	0.737	0.958
3.4	0.174	0.574	0.783

relative to the oxidations observed for **3.1** in DCM. As mentioned in Chapter 2, the tetra-oxidized product of **3.1** is highly reactive and readily decomposes to the di-oxidized state preventing an accurate full characterization. **3.2** has more cathodic oxidation potentials relative to **3.1**; therefore, we hypothesized that it could be more stable when tetra-oxidized. We attempted to synthesize the tetra-cation of **3.2** by reacting it with 10 equivalents of $[(2,4\text{-}Br_2C_6H_3)_3N][B(C_6F_5)_4]$ in DCM with **3.2**; however, attempts to grow X-ray quality crystals of the tetra-cation were unsuccessful. By happenstance, during one of our crystallographic attempts we mounted a crystal of the di-cation of **3.2** and obtained the solid-state molecular structure of $\mathbf{3.2^{2+}}$ (Figure 3.6). Such occurrences were common when we previously attempted to isolate the tetra-cation of **3.1**. The solid-state structure of $\mathbf{3.2^{2+}}$ features two contracted Ni–Ni bonds with Ni1–Ni2 and Ni3–Ni4 distances of 2.7095(18) Ǟ and 2.6284(18) Ǟ (Table 3.1). The bond length and angle metrics are similar to that of $\mathbf{3.1^{2+}}$ also provided in Table 3.1.

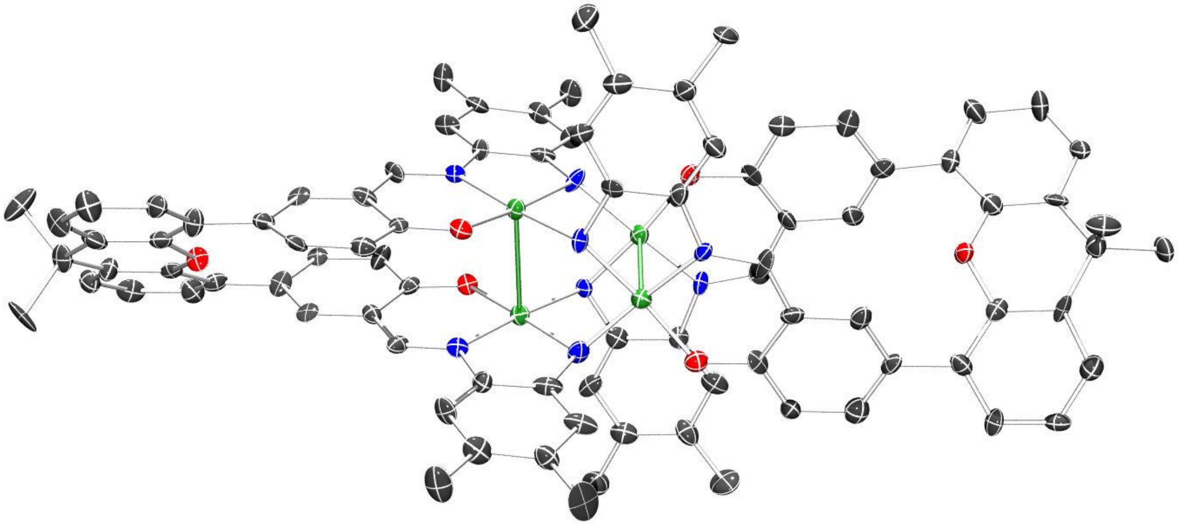

Figure 3.6. Solid state molecular structure of **3.2**$^{2+}$. The solid green bonds represent long Ni–Ni bonds. Hydrogen atoms, counter-anions, and co-crystallized solvent molecules were removed for clarity (C, black; N, blue; O, red; Ni, green).

Cyclic voltammetry of **3.3** in DCM reveals two reversible and one quasi-reversible oxidation events in a 1:1:2 e$^-$ ratio at 0.464, 0.737, and 0.958 V vs. Fc$^+$/Fc respectively (Figure 3.5), which are significantly shifted anodically relative to **3.1**. While it may seem that the second oxidation event is quasi-reversible, if the potential window is cut off prior to the third oxidation event, the second event becomes fully reversible. The EC mechanism associated with the generation of the presumed tetra-cation of **3.3** is indicative of a distinct structural change occuring within the complex that can be captured on the time scale of the slower CV scan rates (Figure 3.7A, black trace). However, if the potential is scanned fast enough then the presumed tetra-cation can be reduced before any significant change in structure can occur (Figure 3.7B, purple trace).

Cyclic voltammetry of **3.4** in DCM provides one reversible and two quasi-reversible oxidation events in a 1:1:2 e$^-$ ratio at 0.174, 0.574, and 0.783 V vs. Fc$^+$/Fc respectively (Figure 3.5). For compounds **3.1-3.3,** the potential window seperation between the second and third oxidation events were distinct, however, the second oxidation in **3.4** has significant overlap with the third oxidation event providing a unique current response without affecting the reversibility of the first redox couple.

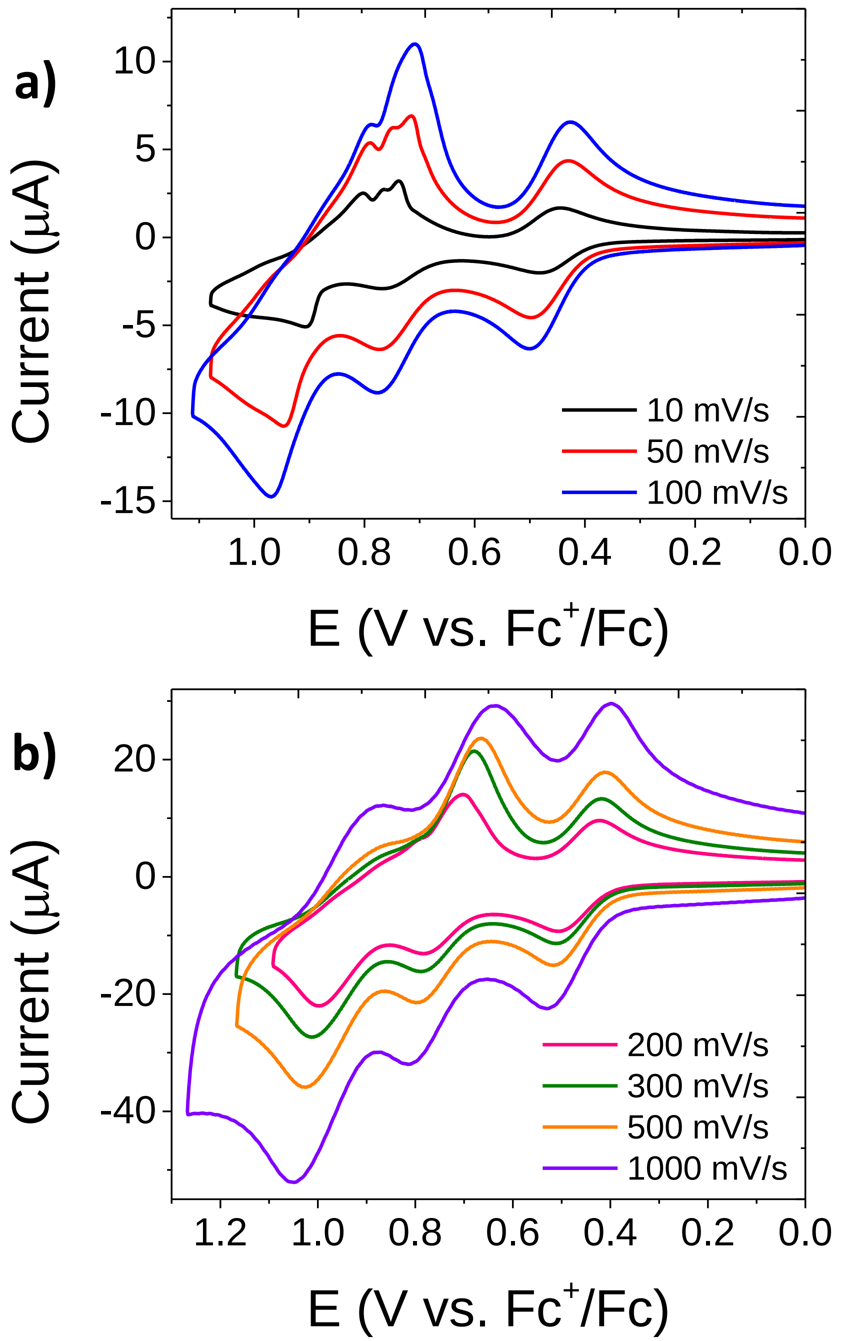

Figure 3.7. CVs of **3.3** in DCM at varying scan rates: (a) 10, 50, and 100 mV/s (b) 200, 300, 500, and 1000 mV/s. Conditions: 0.43 mM of 3.4, 0.1 M $[Bu_4N][PF_6]$ supporting electrolyte, glassy carbon working electrode, Pt wire counter electrode, and Ag wire pseudo-reference electrode).

3.2.3 Electrochemistry of Ni_4 Clusters in 1,2-Difluorobenzene

To effectively probe the reductive behavior of the Ni_4 clusters we used 1,2-difluorobenzene (DFB) as the solvent due to its reductive stability and low donor number. The cyclic voltammogram of **3.1** in DFB spanning both the anodic and cathodic regions is shown in Figure 3.8A. Two $1e^-$ oxidation events followed by a $2e^-$ oxidation were observed at 0.266, 0.644, and 0.901 V vs. Fc^+/Fc respectively, like the redox behavior observed in DCM (Figure 3.5), while two sequential reductions occurred at -2.273 and -2.460 V vs. Fc^+/Fc. The current response for the second reduction is larger than the first reduction, which could be indicative of a $2e^-$ reduction. To elucidate this feature, we performed DPV in the same solution sweeping the potential both anodically and cathodically (Figure 3.8B). The DPV of **3.1** in DFB indicates that the two reductions shown in Figure 3.2 are likely to both be $1e^-$ events; however, **3.1** can access a third reduction which was more easily resolved by DPV than by CV. The third reduction occurs near the potential limit of the solvent which is likely the reason for the large current response of the second reduction at -2.460 V. From the DPV, the anodic peak potentials are at 0.266, 0.646, and 0.910 V vs. Fc^+/Fc while the cathodic peak potentials are -2.273, -2.471, and -2.805 V vs. Fc^+/Fc. The current magnitude of the third reduction may indicate a $2e^-$ event.

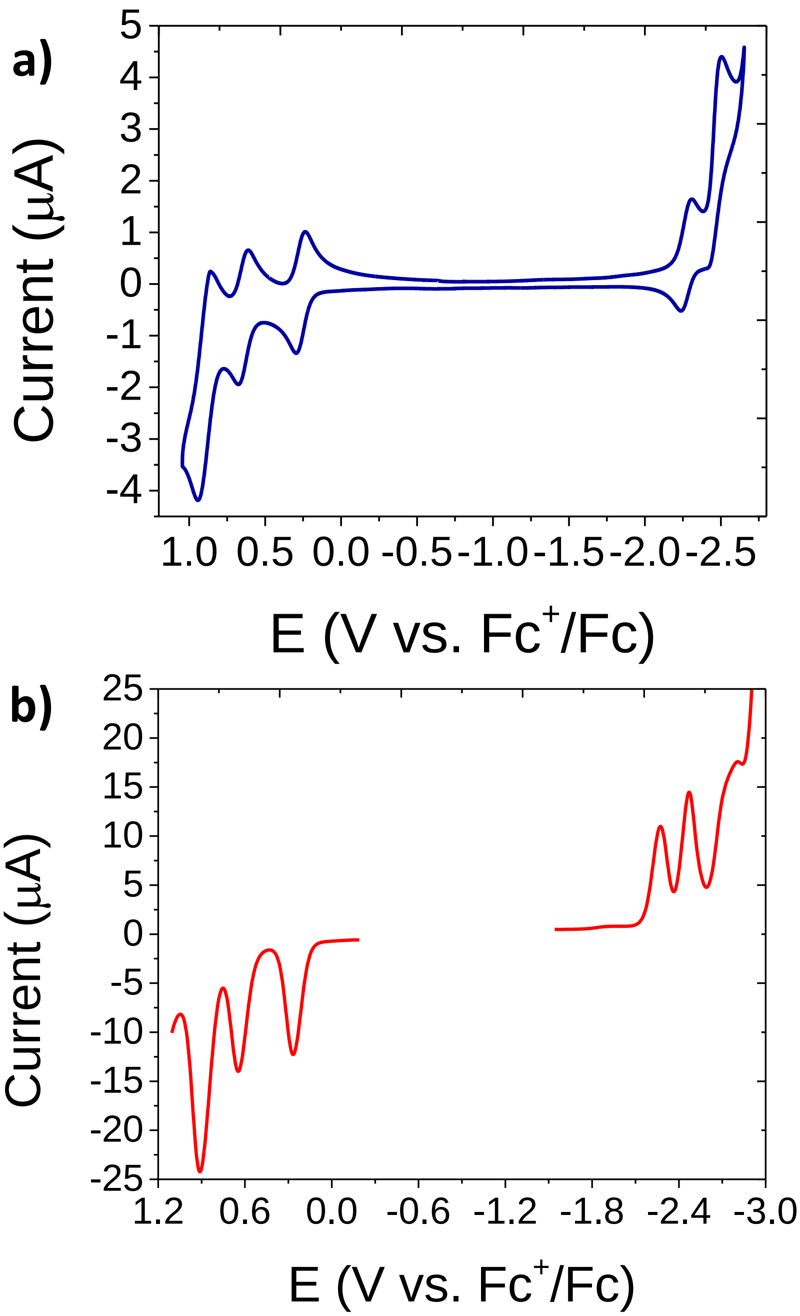

Figure 3.8. (a) CV of **3.1** in DFB at 10 mV/s. (b) Anodic and Cathodic DPVs of **3.1** in DFB. 0.43 mM of **3.1**, 0.1 M $[Bu_4N][PF_6]$ supporting electrolyte, glassy carbon working electrode, Pt wire counter electrode, and Ag wire pseudo.

Cyclic voltammetry of **3.3** in DFB provides oxidation couples at 0.478, 0.717, and 0.912 V vs. Fc$^+$/Fc (Figure 3.9). The third oxidation, while different from the current response observed in DCM, displays a large current spike upon reduction of the presumably formed tetra-cation. We again attribute this feature to a more pronounced structural change in **3.3** than what was observed for **3.1** upon tetra-oxidation. A cathodic scan of **3.3** in DFB provides several reduction events that become more quasi-reversible when the potential window is cycled more cathodically (Figure 3.15). An oxidative feature at -1 V after cycling cathodically also becomes apparant when the potential is scanned past the third reduction couple. The first two reduction events are fully reversible when the potential is cut off after the latter. From the CV, the first two reductions occur at -2.081 and -2.300 V vs. Fc$^+$/Fc; however, the midpoint potential of the subsequent reductons are too ambiguous to assign.

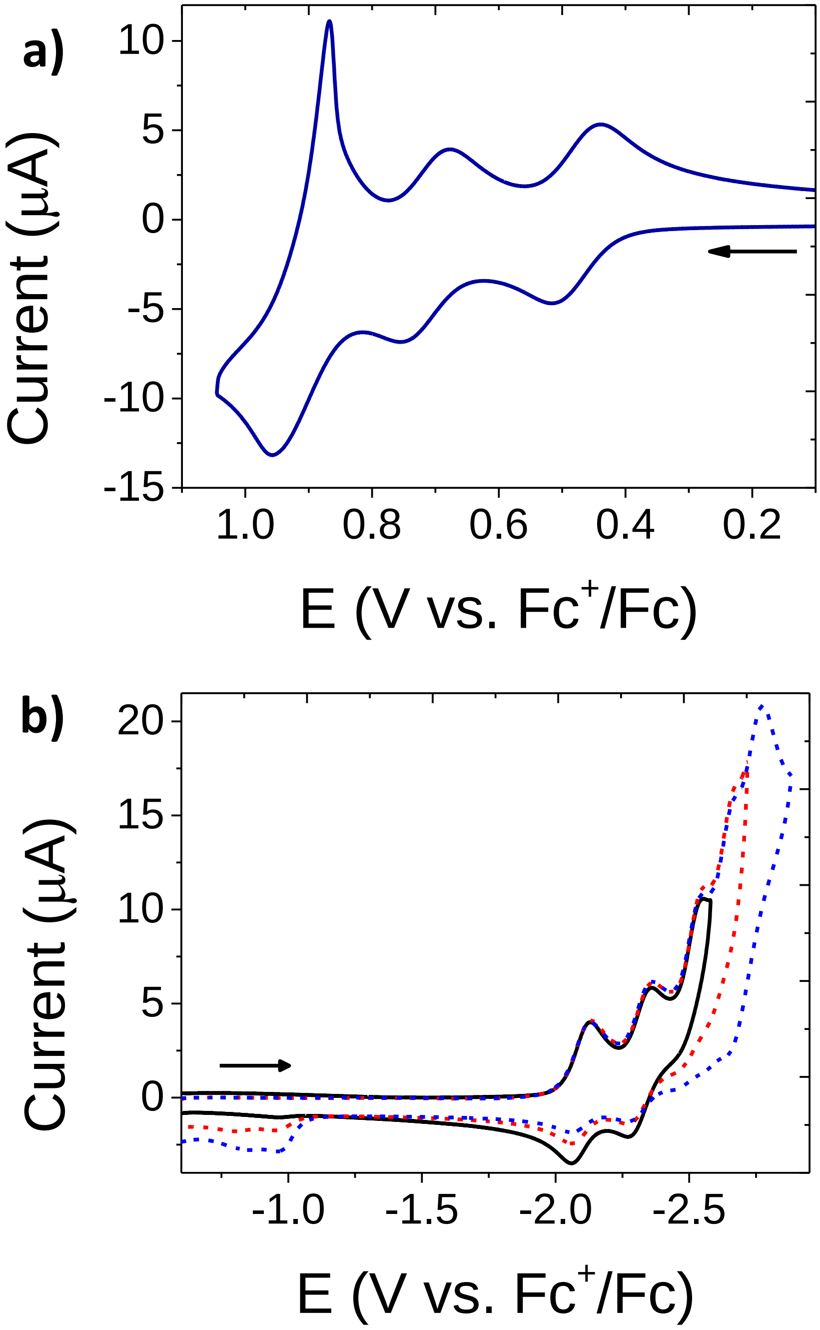

Figure 3.9. (a) Oxidative CV of **3.3** in DFB at 100 mV/s. (b) Reductive CVs of **3.4** in DFB at 100 mV/s with varying potential windows. 0.43 mM of **3.3**, 0.1 M [Bu_4N][PF_6] supporting electrolyte, glassy carbon working electrode, Pt wire counter electrode, and Ag wire pseudo-reference electrode.

DPV of **3.3** in DFB further elucidates the reductions observed by CV for which two small current peaks are present after the second reduction following by another reduction that is more proportional in current magnitude (Figure 3.10A). Integration of the the first two reduction peaks together and the subsequent reductions from the DPV (Figure 3.10B) provides two similar areas, indicative that the reductions of **3.3** mirror that of the oxidations by following a 1:1:2 e^- reduction event motif. From the DPVs shown in Figure 3.10A, the voltage window of **3.3** is 3.658 V by comparing the midpoint potentials of both the most reductive and oxidative peaks.

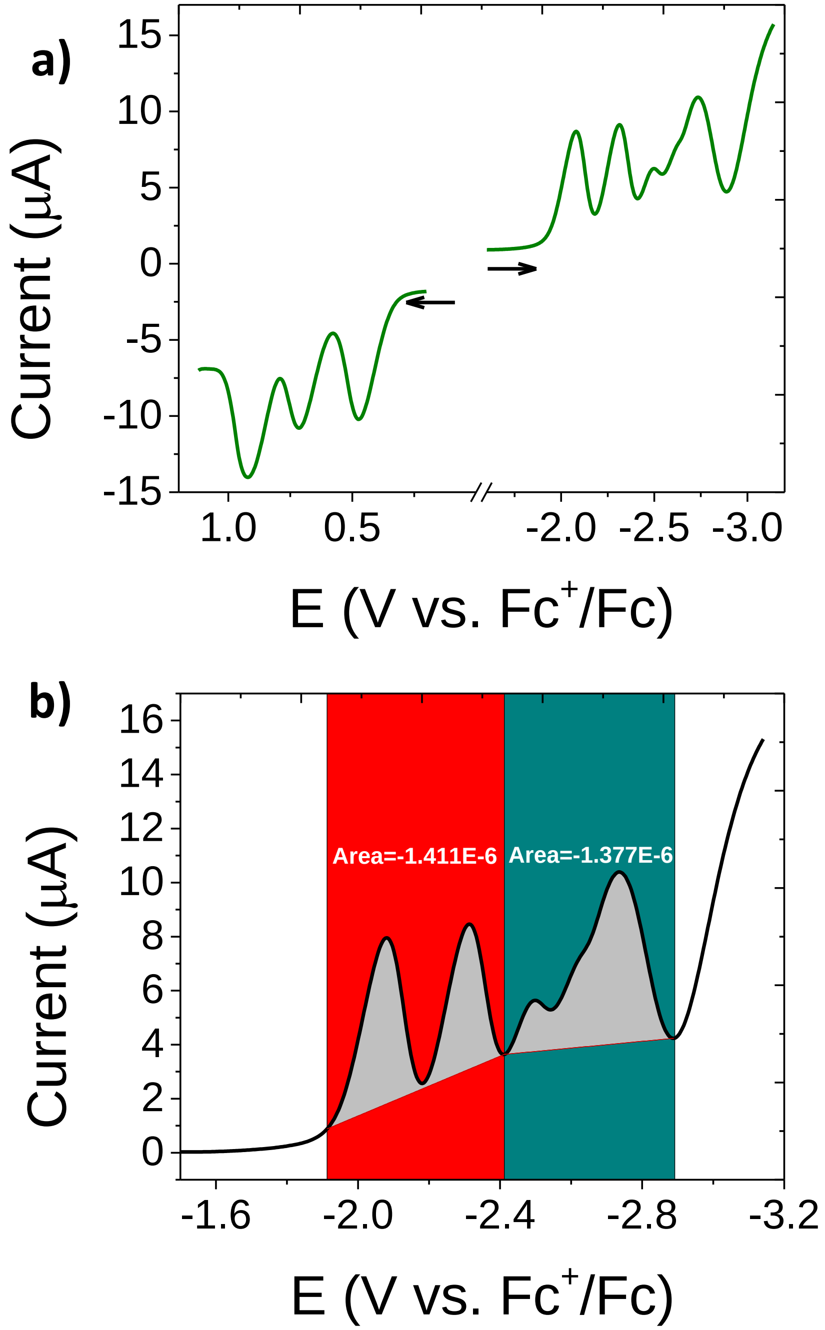

Figure 3.10. (a) Anodic and cathodic DPVs of **3.3** in DFB. (b) Estimation of the number of electrons associated with each reduction by a rough integration of the peaks. 0.43 mM of **3.3**, 0.1 M $[Bu_4N][PF_6]$ supporting electrolyte, glassy carbon working electrode, Pt wire counter electrode, and Ag wire pseudo-reference electrode.

3.2.4 Electrochemistry of Ni_4 Clusters in Butyronitrile

As discussed in Chapter 2, the tetra-oxidation of **3.1** results in a highly reactive all Ni^{III} tetra-cation species that is difficult to isolate in high purity and study spectroscopically.[9] We hypothesized that a redox inert ligand might stabilize the high-valent nickel centers if coordinated upon oxidation. To evaluate this hypothesis, we sought to collect electrochemical data of **3.1** in acetonitrile (MeCN) due its redox inert and coordinating characteristics. Unfortunately, **3.1** is completely insoluble in MeCN, however, it is soluble in butyronitrile (BuCN). Cyclic voltammetry of **3.1** in BuCN with potentials swept anodically reveals a quasi-reversible redox couple at 0.292 V (measured at 1000 mV/s scan rate) followed by an irreversible oxidation event with a peak potential at 0.591 V vs. Fc^+/Fc (measured at 10 mV/s scan rate) (Figure 3.11). The first oxidation is quasi-reversible with a reversible wave observable at faster scan rates and the second oxidation is irreversible regardless of scan rate. Such features are indicative of an EC mechanism (electron transfer followed by chemical reaction).

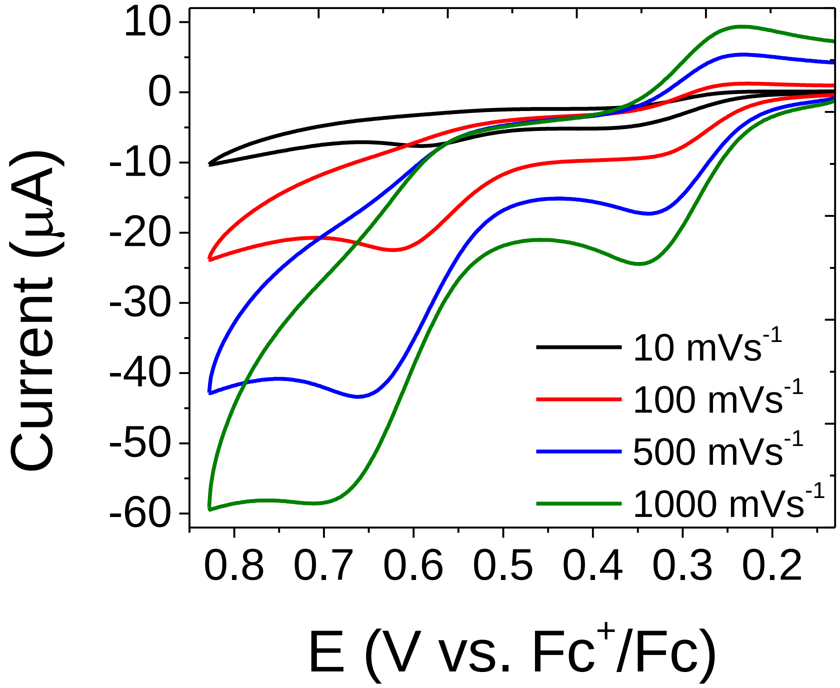

Figure 3.11. CVs at varying scan rates of **3.1** in BuCN (0.43 mM of **3.1**, 0.1 M $[Bu_4N][PF_6]$ supporting electrolyte, glassy carbon working electrode, Pt wire counter electrode, and Ag wire pseudo-reference electrode).

In Chapter 2, we described having to treat **3.1** with 10 equivalents of the "magic-green" oxidant, $[(2,4\text{-}Br_2C_6H_3)_3N]^+$, to isolate and grow x-ray quality crystals of the tetra-cation species. While the potential of the second oxidation of **3.1** in BuCN is reminiscent of the midpoint potential of **3.1**$^{2+}$ in DCM (Figure 3.5), the current intensity in BuCN (Figure 3.11) could be indicative of a multi-electron event. Therefore, out of caution, when targeting the product of the EC mechanism revealed in Figure 3.11, we used a slight excess of magic-green. To elucidate the product of the electrochemical reaction, we treated a frozen slurry of **3.1** in MeCN with 6 equivalents of magic-green oxidant and allowed the reaction to warm up to room temperature with stirring (Scheme 3.2). The color of the reaction changed from red to

Scheme 3. Reaction of **3.1** with 6 equivalents of $[(2,4\text{-}Br_2C_6H_3)_3N][SbF_6]$. The reaction is not balanced.

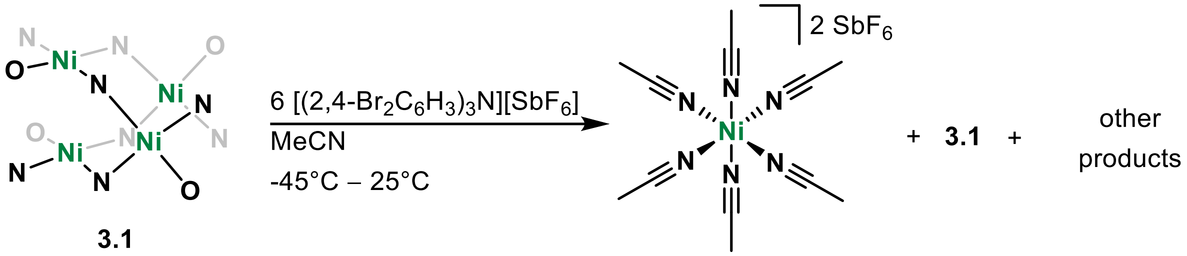

green to a brown/red color. After working up the reaction, the ^{1}H NMR revealed a mixture of diamagnetic and paramagnetic products.

Single crystals suitable for XRD studies were obtained from the reaction after purification providing unit cells for hexakis(acetonitrile)nickel(II) with two SbF_6 counter-anions and the **3.1** starting material.[9, 21] Despite several attempts, we were unsuccessful in growing diffraction quality crystals of other products from the reaction to effectively balance it. While the formation of the hexa-acetonitrile nickel salt was undesirable, we can conclude that the nickel centers in **3.1** are susceptible to further coordination upon oxidation.

While methylation of the ligand did not increase the solubility of **3.2** in MeCN, the $^{Me}LH_4$ ligand should chelate stronger than the $^{H}LH_4$ ligand and provide a unique electrochemical response in BuCN. Cyclic voltammetry of **3.2** in BuCN at 10 mV/s (Figure 3.12, black trace) revealed a unique electrochemical response relative to **3.1** (Figure 3.12, dashed red trace). From Figure 3.12, compound **3.1** shows a larger current magnitude at the initial oxidation event than the second, while the opposite is observed in the black trace of compound **3.2**. Also, the initial oxidation of **3.2** is more reversible than for **3.1**. Further optimization of the ligand and cluster could lead to the development of reversible redox events like what was observed in DCM in donating solvents like nitriles.

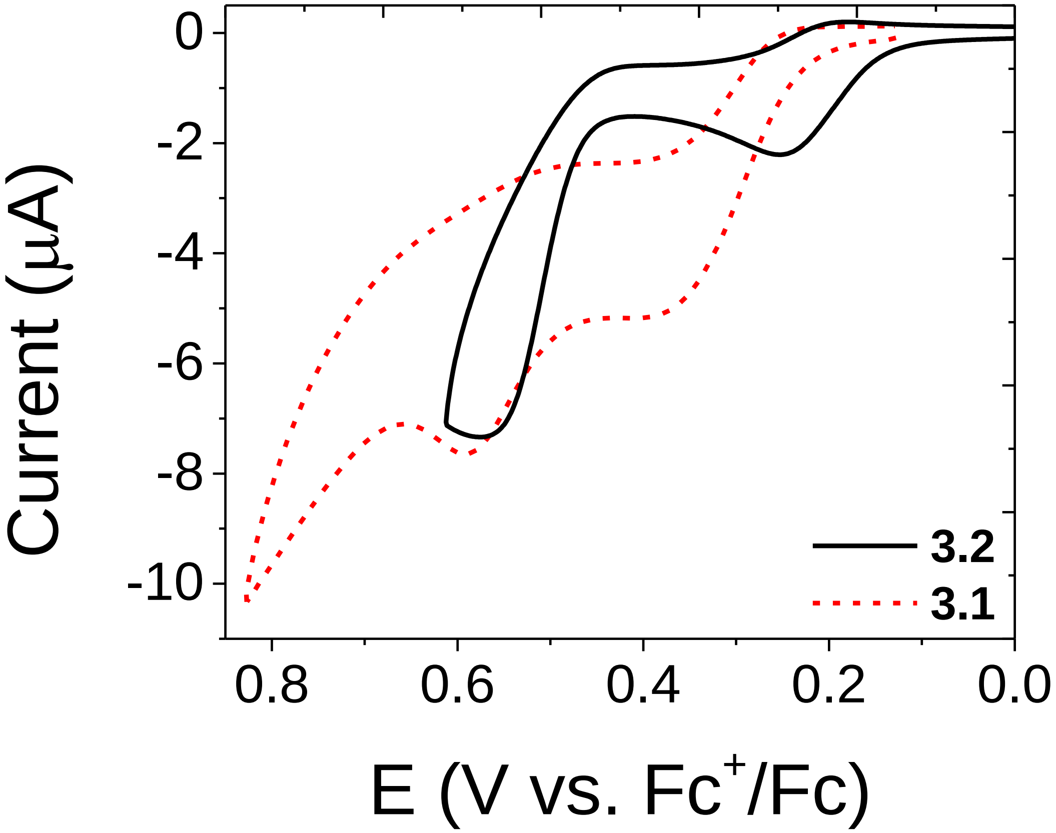

Figure 3.12. CVs in BuCN at 10 mV/s of **3.2** (black trace) and **3.1** (red dashed trace). 0.43 mM of **3.2** or **3.1**, 0.1 M $[Bu_4N][PF_6]$ supporting electrolyte, glassy carbon working electrode, Pt wire counter electrode, and Ag wire pseudo-reference electrode).

3.2.5 Electrochemistry of Ni_4 Clusters in Tetrahydrofuran

Cyclic voltammetry of **3.1** in THF revealed two reversible oxidations at 0.254 V and 0.605 V vs. Fc^+/Fc (Figure 3.13). Interestingly, THF is a coordinating solvent with a higher donor number than acetonitrile and is easily susceptible to oxidation; however, an EC mechanism was not observed on the CV time scale like in Figure 3.11.[22, 23] Cyclic voltammetry of **3.2** in

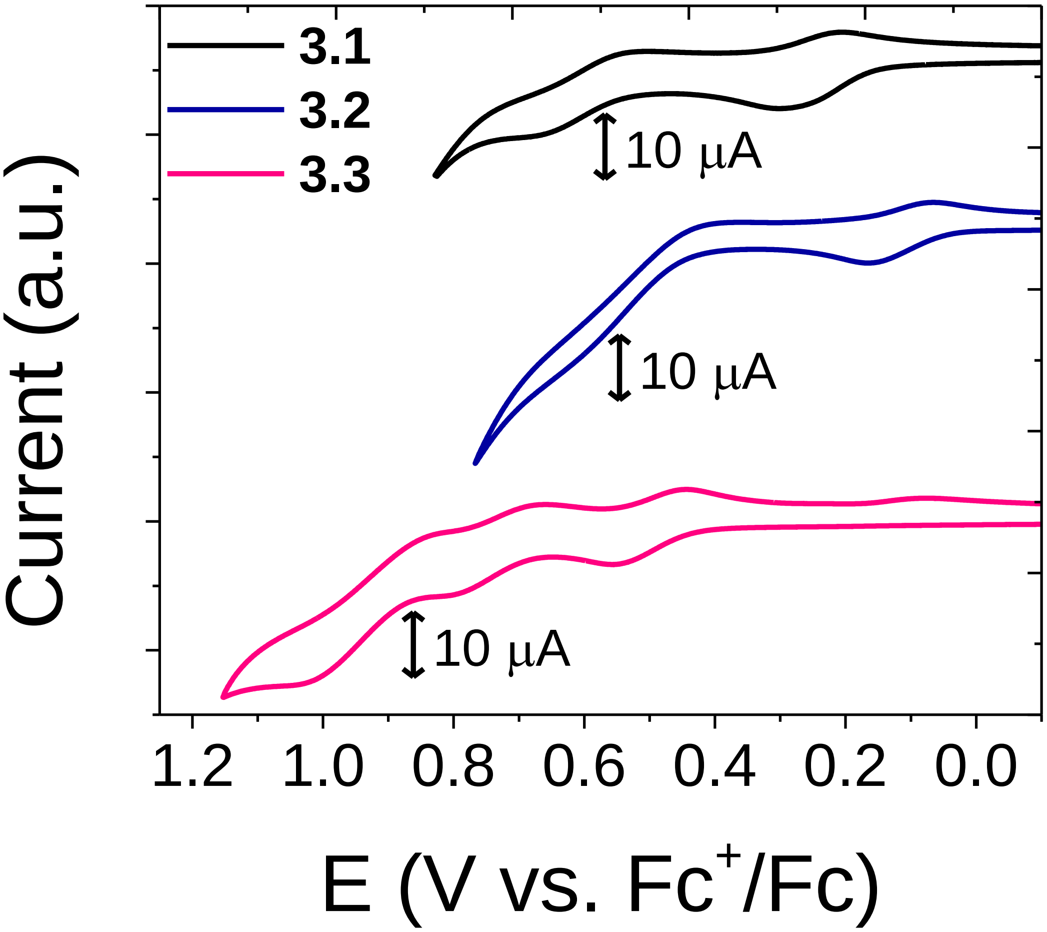

Figure 3.13. Stacked CVs of **3.1**, **3.2**, and **3.3** in THF at 100 mV/s scan rates (0.43 mM [Ni_4], 0.1 M [Bu_4N][PF_6] supporting electrolyte, glassy carbon working electrode, Pt wire counter electrode, and Ag wire pseudo-reference electrode).

THF revealed a reversible oxidation at 0.116 V vs. Fc^+/Fc, a 0.138 V cathodic shift relative to **3.1**, followed by a catalytic current likely induced by the formation of the **3.2**$^{2+}$ (Figure 3.13). The catalytic feature observed for **3.2** in THF further deviates from electrochemical response observed in BuCN (Figure 3.12). In contrast cyclic voltammetry of **3.3** in THF revealed three reversible oxidations at 0.501 V, 0.738 V, and 0.934 V vs. Fc^+/Fc as well as a reduction at 0.077 V vs. Fc^+/Fc on the return sweep towards the origin (Figure 3.13). The reduction at 0.077 V is only observable upon accession of the third redox couple.

Despite having the most cathodic oxidation potentials, **3.2** is the only compound for which catalytic oxidation of THF was observed. The catalysis is likely the result of an inner-sphere reaction between **3.2** and THF, otherwise the same catalytic current would have been observed for both **3.1** and **3.3** considering they have significantly more anodic oxidation potentials than **3.2**.

3.2.6 Investigation of Catalytic Ammonia Oxidation

MeCN is an ideal organic solvent for studying catalytic NER due to its redox inert nature and the solubility of NH_3 (~2 M) and has been utilized for several molecular catalysts[24-31]. Despite the lower solubility of NH_3, other catalytic examples have utilized benzene[29] or THF[26, 32] for studying catalytic NER. Due to the insolubility of **3.1** in MeCN and the complications of performing electrochemical measurements in benzene, we investigated catalytic NER using **3.1** in THF.

Compound **3.1** features a $1e^-$ oxidation at 0.254 V vs. Fc^+/Fc and in the presence of NH_3 (~930 equivalents) a catalytic current is observed with an onset potential of 0.090 V vs. Fc^+/Fc (Figure 3.14). The onset of catalysis in the red trace occurs more cathodically than catalytic oxidation of NH_3 at the glassy carbon working electrode (Figure 3.14, blue dashed trace), confirming the catalytic reaction in the red trace is induced by compound **3.1**. Interestingly, a pronounced pre-catalytic wave is present (Figure 3.14, red trace) that begins approximately at -0.4 V and increases until the onset of catalysis at 0.090 V. A similar pre-catalytic event has been reported for water oxidation catalyzed by a nickel cyclam analog.[16] In both cases, it is likely that a chemical step, such as coordination and/or a structural change, is occurring prior to an electron transfer.

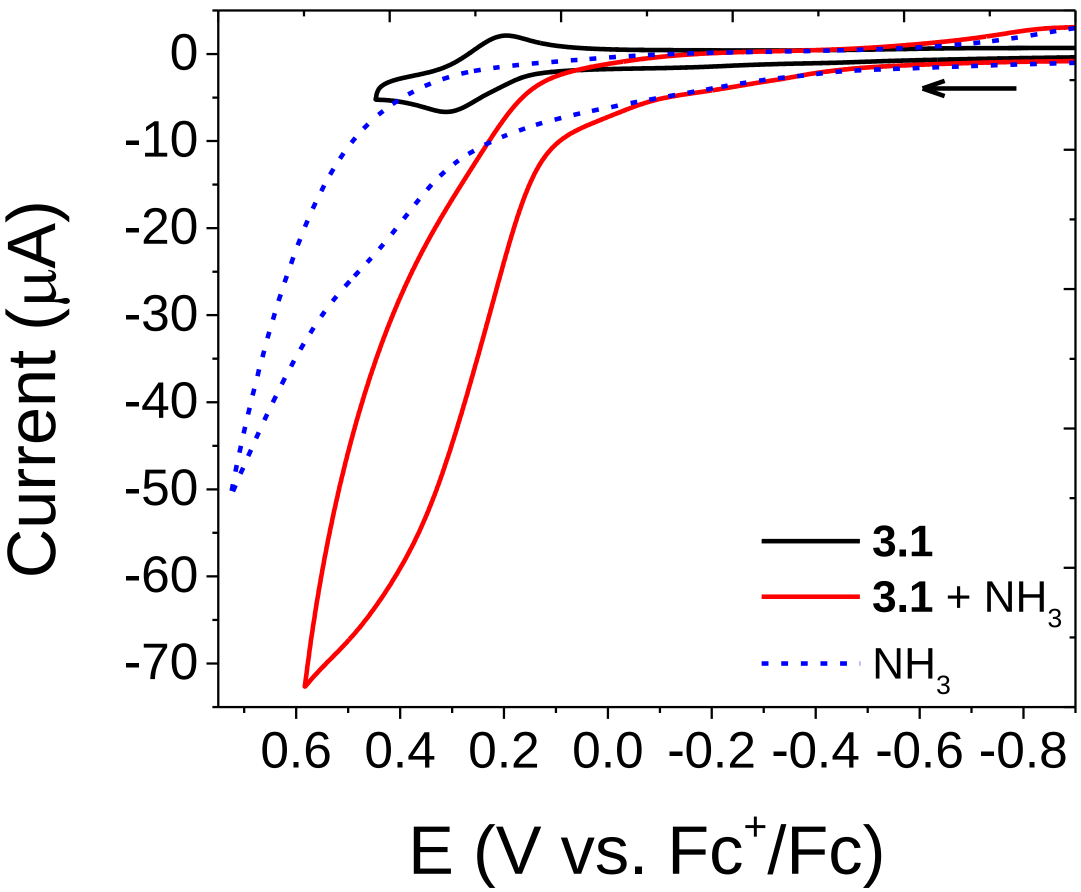

Figure 3.14. CV of **3.1** in THF at 100 mV/s (black trace), with NH_3 added as a substrate (red trace), and just NH_3 (blue dashed trace). 0.43 mM of **3.1**, 0.1 M $[Bu_4N][PF_6]$ supporting electrolyte, 0.4 M NH_3, glassy carbon working electrode, Pt wire counter electrode, and Ag wire pseudo-reference electrode.

Compound **3.2** was investigated under similar conditions using cyclic voltammetry and a catalytic current in the presence of NH_3 was evident with a catalytic onset potential of -0.032 V vs. Fc^+/Fc (Figure 3.15). The catalytic onset potential for **3.2** is shifted 122 mV cathodically relative to the onset potential observed for **3.1** (Figure 3.14).

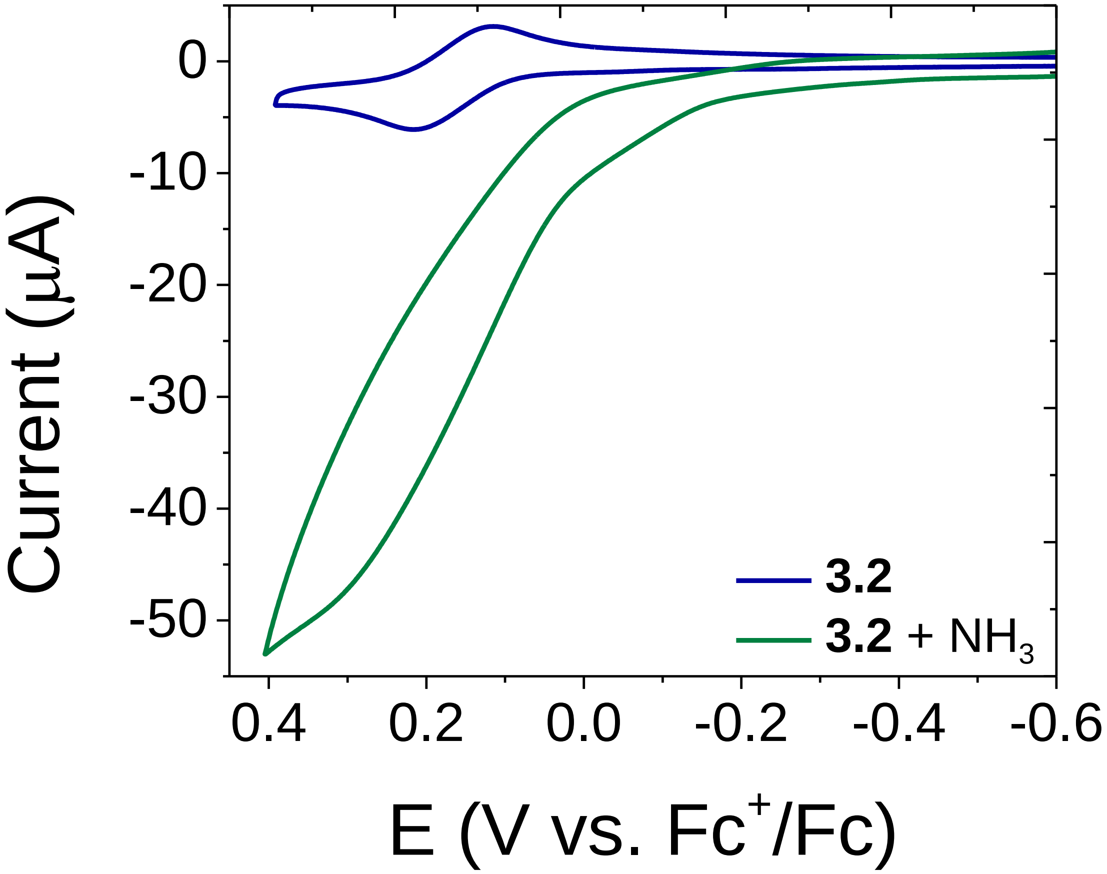

Figure 3.15. CV of **3.2** in THF at 100 mV/s (blue trace) and with NH_3 added as a substrate (green trace). 0.43 mM of **3.2**, 0.1 M $[Bu_4N][PF_6]$ supporting electrolyte, 0.4 M NH_3, glassy carbon working electrode, Pt wire counter electrode, and Ag wire pseudo-reference electrode.

The catalytic green trace in Figure 3.15 also features a pronounced pre-catalytic wave for **3.2**, similar to that of **3.1**, and is also likely caused by a chemical step prior to the electron transfer step. Currently, only one molecular electrocatalyst, a polypyridyl ruthenium complex, has been reported for catalytic NER in THF. However, the ruthenium catalyst features an impressive onset potential of 0.03 V vs Fc^+/Fc in THF. Interestingly, compound **3.2** displays an onset for NH_3 oxidation 62 mV more cathodic than that of leading Ruthenium catalyst in THF. These results highlight that both **3.1** and **3.2** are promising candidates for studying electrocatalytic NER. The ligand framework for the Ni_4 class of clusters is easily modified; therefore, optimization of the catalyst should be facile for later studies.

3.2.7 Preliminary Investigation of Catalytic Water Oxidation

Compound **3.1** displayed promising electrocatalytic reactivity for the catalytic oxidation of NH_3. However, **3.1** can also be tetra-oxidized to an all Ni^{III} complex making it a promising candidate to study the $4e^-$ water oxidation reaction to produce O_2. While DCM provided great stability and was necessary for the full characterization of **3.1**, as discussed in Chapter 2, we opted to use the related 1,2-dichloroethane (DCE) for our preliminary water oxidation investigation. DCE has a lower vapor pressure than DCM which makes electrochemical studies, requiring sparging solutions to detect O_2, more facile and is more reputable than DCM for stabilizing reactive cations.[33]

Cyclic voltammetry of **3.1** in carefully dried DCE revealed three reversible oxidations at 0.235, 0.633, and 0.928 V vs. Fc^+/Fc (Figure 3.16, black trace) in the same 1:1:2 e^- ratio observed in DCM (Figure 3.5, black trace). Next, we performed cyclic voltammetry of **3.1** in wet DCE outside of the glovebox. For this measurement, we carefully degassed the solution by bubbling argon and swept the potential cathodically to -1.6 V vs. Fc^+/Fc and the current did not increase for this portion of the measurement indicating no oxygen was present in solution (Figure 3.16, dashed red trace). During the same CV measurement, the potential was swept anodically to 1.30 V vs. Fc^+/Fc and then back to -1.6 V (Figure 3.16, blue trace). From the blue trace, large catalytic current was observed upon accessing the third oxidation of **3.1**, perhaps indicative of water oxidation, and another large current was observed during the cathodic return sweep at -1.20 V vs. Fc^+/Fc. We attribute this reduction at -1.20 V vs. Fc^+/Fc as reduction of O_2 generated from the oxidation of water during the anodic scan. To confirm this, we performed a control experiment in the absence of **3.1** in wet DCE for which we swept the potential cathodically in the presence of air and observed O_2 reduction at the same potential (Figure 3.16 purple dashed trace).

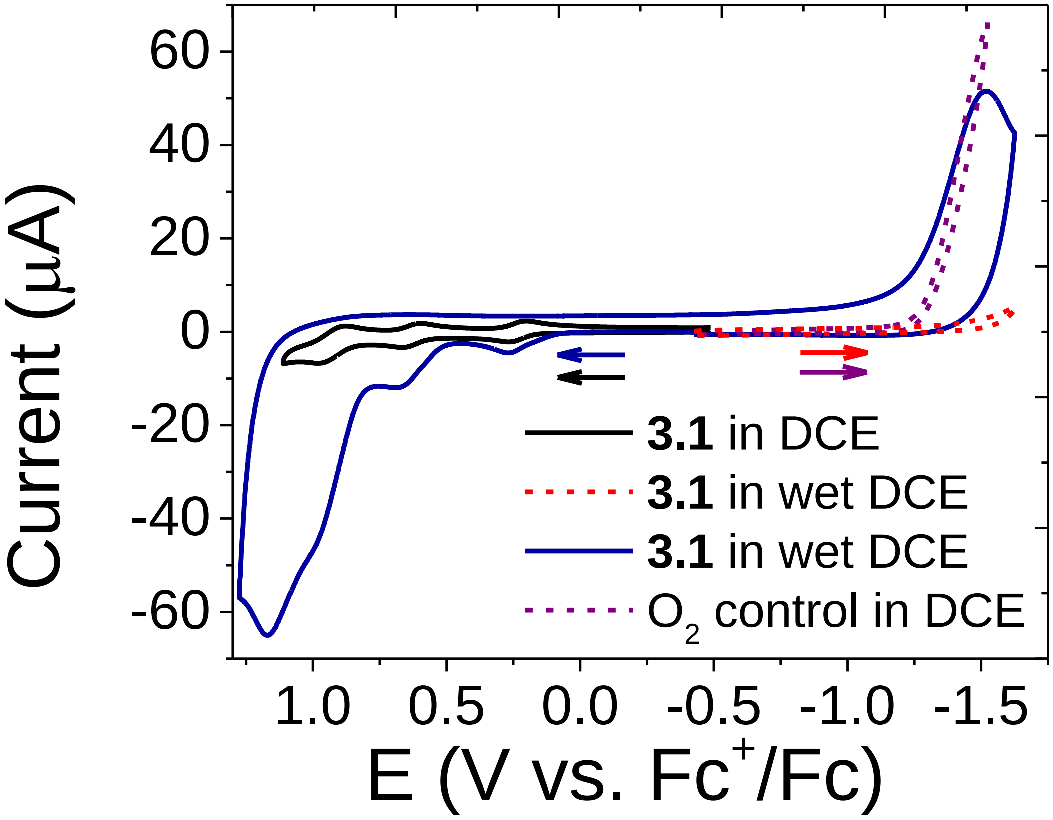

Figure 3.16. CV of **3.1** in dry DCE at 100 mV/s in the glovebox (black trace); **3.1** in wet DCE at 100 mV/s degassed with argon swept cathodically (red dashed trace) and then anodically (blue trace) in the same measurement; CV of wet DCE in the absence of inert gas and **3.1** (purple dashed trace). 0.43 mM of **3.1**, 0.1 M $[Bu_4N][PF_6]$ supporting electrolyte, glassy carbon working electrode, Pt wire counter electrode, and Ag wire pseudo-reference electrode.

From these results, **3.1** is shown to be a promising candidate for molecular water oxidation catalysis. The investigation of **3.1** for water oxidation is difficult, however, because the solvents it is most soluble and most stable in are immiscible with water. Although it is rarely used for studying water oxidation, **3.1** has appreciable solubility in 1,2-dimethoxyethane (DME) which is miscible with water and is relatively stable towards oxidation, allowing further investigation. Cyclic voltammetry of **3.1** in DME revealed two reversible oxidations at 0.341 V and 0.694 V vs. Fc^+/Fc followed by a quasi-reversible oxidation at 0.946 V vs. Fc^+/Fc (Figure 3.17, red trace). The third oxidation significantly deviates from the reversible redox events observed in DCM, DCE, and DFB. Oxidation of DME shown to occur outside of the analyte scans by the control scan in Figure 3.17 (black dashed trace) and is likely due to trace water or the coordinating nature of DME. Upon addition of 0.1 mL of water to a 3 mL solution of **3.1** in DME, we observe large increases in current at the onset for both the second and third oxidation events. Given the potential, it is unlikely that O_2 would be generated at the second oxidation of **3.1**, in which case, an intermediate, like hydrogen peroxide, could be the result of the increased current density. The purple dashed trace in Figure 3.17 confirms that the increase in current upon addition of water is induced by **3.1**. Optimization of the Ni_4 complex to increase solubility in solvents like acetonitrile or propylene carbonate would be ideal for further investigation into water oxidation.

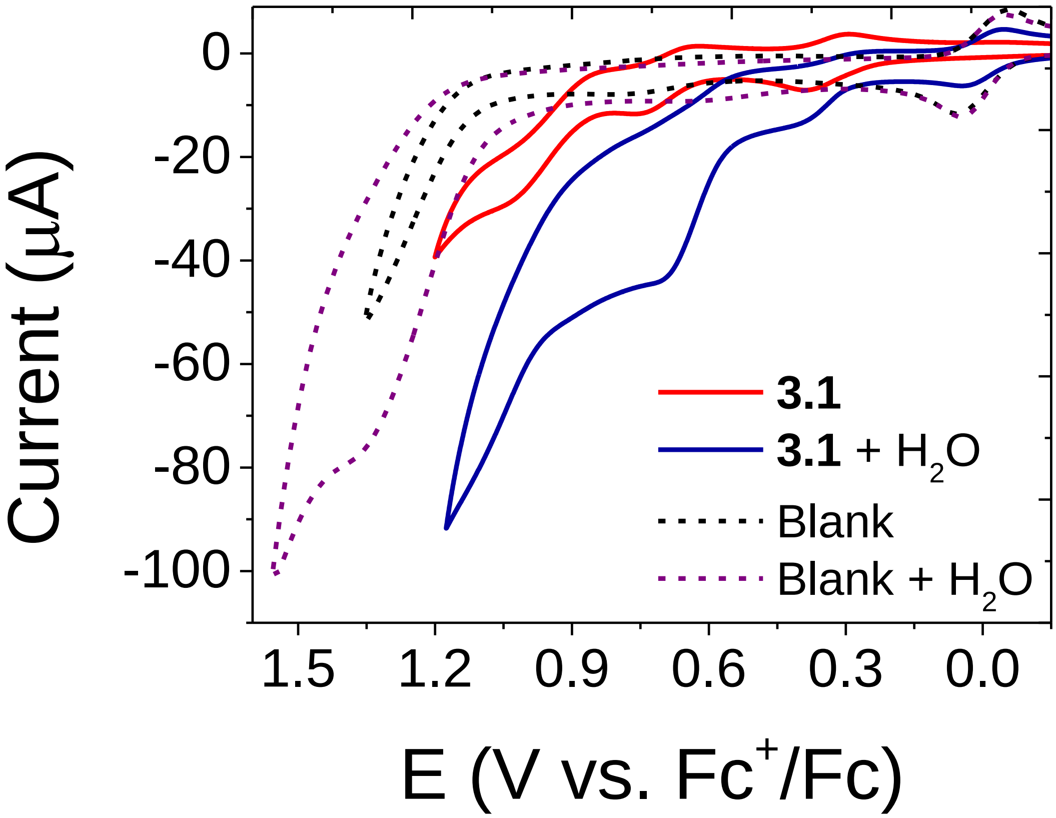

Figure 3.17. CV of **3.1** in DME at 100 mV/s (red trace), with H_2O added as a substrate (blue trace), in the absence of **3.1** in DME (black dashed trace), and absence of **3.1** with H_2O (purple dashed trace). Ferrocene is included as an internal reference in the blue, black, and purple traces. 0.43 mM of **3.1**, 0.1 M $[Bu_4N][PF_6]$ supporting electrolyte, glassy carbon working electrode, Pt wire counter electrode, and Ag wire pseudo-reference electrode

3.3 Summary

In conclusion, synthesized and crystallographically characterized analogous tetranuclear Ni species originally discussed in Chapter 2. We show that the redox properties of the cluster can be influenced by functionalizing the ligand with various substituents. Also, preliminary results suggest that the Ni_4 platform, and its analogs, are promising candidates for studying catalytic NER.

3.5 Experimental

3.5.1 General Considerations

Techniques and Reagents. All manipulations were performed under an atmosphere of dry N_2 by means of standard Schlenk or glovebox techniques (MBRAUN UNIlab Pro SP Eco equipped with a −40 °C freezer), unless stated otherwise. Hexanes (Fisher), Benzene (Sigma), and DCM (Fisher) were dried using an MBRAUN-Solvent Purification System. 1,2-difluorobenzene, butyronitrile, and 1,2-dimethoxyethane were degassed by 4 cycles of freeze pump/thaw prior to bringing them into the glovebox. All solvents were stored over activated 4 Å molecular sieves for 2 days prior to use. $Ni(OAc)_2•4H_2O$, 4,5-dimethyl-1,2-diaminobenzene, and 4,5-difluoro-1,2-diaminobenzene were purchased from Fisher and used as received. Deuterated solvents were purchased from Cambridge Isotope Laboratories and stored over 4 Å molecular sieves for at least 2 days prior to use. Celite was dried by heating above 250 °C under dynamic vacuum for at least 48 h prior to use. 5,5’-(9,9-

Dimethylxanthene-4,5-diyl)bis(salicylaldehyde)[34], 4,5-dimethoxy-1,2-diaminobenzene[35], and $[(2,4\text{-}C_6H_3Br_2)_3N][B(C_6F_5)_4]$[36] were prepared according to literature procedures.

Spectroscopic Measurements. NMR spectra were obtained on Agilent Technologies 400 and 600 MHz spectrometers, and referenced to residual solvent or externally (^{19}F, $CFCl_3$). Chemical shifts (δ) are recorded in ppm, and the coupling constants are in Hz.

Electrochemical Measurements. Cyclic voltammetry was performed on a CH Instruments 630E electrochemical analysis potentiostat, equipped with a 3 mm diameter glassy carbon working electrode, a Ag wire pseudo-reference electrode, and a Pt wire counter electrode in a conventional three-electrode cell. DCM, BuCN, DFB, DME, and THF were used as the solvent for electrochemical measurements with $[Bu_4N][PF_6]$ (0.1 M) as the supporting electrolyte. The glassy carbon working electrode was cleaned prior to each experiment by polishing with 1, 0.3, and 0.05 mm alumina (CH Instruments) in descending order, followed by a water rinse and finally brief sonication in water. The potential of the pseudo-reference was referenced to the Fc^+/Fc redox couple.

2.4.2 Syntheses

$^{Me}LH_4$: A 50 mL round bottom flask was charged with 5,5'-(9,9-Dimethylxanthene-4,5-diyl)bis(salicylaldehyde)[34] (200 mg, 0.444 mmol), 4,5-dimethyl-1,2-diaminobenzene (605 mg, 4.440 mmol), and ethanol (25 mL). The reaction was refluxed overnight hours open to atmosphere. After several minutes the reactants went into solution and formed a deep orange color. Eventually, yellow-orange precipitates were formed. After reflux, the reaction was allowed to cool to room temperature and was filtered. The yellow product was washed with ethanol and dried under vacuum. Yield: 470 mg (91%). ^{1}H NMR (400 MHz, Acetone) δ 13.41 (s, 2H), 8.28 (s, 2H), 7.59 – 7.53 (m, 2H), 7.34 (d, *J* = 2.1 Hz, 2H), 7.30 (dd, *J* = 8.3, 2.3 Hz, 2H), 7.25 – 7.15 (m, 4H), 6.82 (d, *J* = 2.0 Hz, 2H), 6.70 – 6.63 (m, 4H), 4.60 (s, 4H), 2.12 (s, 6H), 2.11 (s, 6H), 1.75 (s, 6H).

3.2: To a 250 mL round bottom flask was added a magnetic stir bar, **^{Me}LH$_4$** (277 mg, 0.4033 mmol), $Ni(OAc)_2•4H_2O$ (201 mg, 0.8066 mmol), and 125 mL of ethanol. The reaction was refluxed overnight. Upon heating, the powders went into solution and the color changed into a deep red and red precipitates eventually formed. After reflux, the reaction was removed from heat and allowed to cool to room temperature. The reaction was filtered over a fine frit. The red solids were washed with ethanol until the washings were colorless. Next the crude product was washed with water (2 x 10 mL), methanol (4 x 10 mL), and finally hexanes (3 x 10 mL). The red product was dried under high vacuum at 100 °C overnight before bringing into the glovebox. Yield: 349.1 mg (53%). X-ray quality crystals were grown by vapor diffusion of hexanes into a concentrated DCM solution of the product at room temperature. NMR. ^{1}H NMR (400 MHz, $CDCl_3$) δ 8.56 (s, 4H), 7.43 – 7.35 (m, 12H), 7.24 (d, *J* = 1.6 Hz, 4H), 7.15 (d, *J* = 7.3 Hz, 9H), 6.91 (s, 4H), 6.47 (d, *J* = 8.6 Hz, 4H), 2.28 (s, 13H), 2.21 (s, 13H), 1.77 (s, 12H), 1.28 (s, 4H).

.

^{F}LH$_4$: The synthesis of this compound was analogous to **^{Me}LH$_4$** except that 4,5-difluoro-1,2-diaminobenzene was used instead of 4,5-dimethyl-1,2-diaminobenzene. Yield: 517 mg (66%). ^{1}H NMR (400 MHz, Acetone) δ 12.86 (s, 2H), 8.30 (2, 2H), 7.57 (dd, *J* = 7.4, 2.2

Hz, 2H), 7.36 (d, *J* = 8.0 Hz, 4H), 7.25 – 7.16 (m, 4H), 7.07 (m, 2H), 6.81 – 6.68 (m, 4H), 5.03 (1, *J* = 8.8 Hz, 4H), 1.75 (s, 6H).

3.3: The synthesis of this compound was analogous to **3.2** except that **^{F}LH$_4$** was used instead of **^{Me}LH$_4$**. Yield: 298 mg (50%). ^{1}H NMR (400 MHz, CDCl$_3$) δ 8.60 (t, *J* = 9.2 Hz, 4H), 7.53 – 7.31 (m, 14H), 7.20 (dd, *J* = 23.7, 7.4 Hz, 10H), 6.98 (d, *J* = 8.5 Hz, 8H), 6.53 (d, *J* = 8.6 Hz, 4H), 3.73 (s, 4H), 1.76 (s, 12H), 1.30 (s, 4H).

^{OMe}LH$_4$: The synthesis of this compound was analogous to **^{Me}LH$_4$** except that 4,5-dimethoxy-1,2-diaminobenzene was used instead of 4,5-dimethyl-1,2-diaminobenzene. And the reaction stirred at room temperature under nitrogen overnight. Yield: 123 mg (72%). ^{1}H NMR (400 MHz, acetone) δ 13.40 (s, 2H), 8.24 (s, 2H), 7.56 (dd, *J* = 7.5, 1.9 Hz, 2H), 7.35 – 7.11 (m, 8H), 6.81 (s, 2H), 6.66 (d, *J* = 8.3, 1.8 Hz, 2H), 6.51 (s, 2H), 4.60 (s, 4H), 3.75 (s, 6H), 3.74 (s, 6H), 1.75 (s, 6H).

3.4: The synthesis of this compound was analogous to **3.2** except that **^{OMe}LH$_4$** was used instead of **^{Me}LH$_4$** and the reaction was refluxed under nitrogen. Yield: 70 mg (50%). ^{1}H NMR (400 MHz, cdcl$_3$) δ 8.33 (s, 4H), 7.39 (dd, *J* = 18.9, 10.4 Hz, 12H), 7.26 (s, 5H), 7.15 (t, *J* = 7.7 Hz, 4H), 6.95 (s, 4H), 6.63 (s, 4H), 6.55 (d, *J* = 8.6 Hz, 4H), 3.93 (s, 12H), 3.91 (s, 12H), 1.77 (s, 12H), 1.29 (s, 4H).

3.6 References

1. Itoh, S.; Bandoh, H.; Nakagawa, M.; Nagatomo, S.; Kitagawa, T.; Karlin, K. D.; Fukuzumi, S., Formation, characterization, and reactivity of bis(mu-oxo)dinickel(III) complexes supported by a series of bis[2-(2-pyridyl)ethyl]amine ligands. *J Am Chem Soc* **2001,** *123* (45), 11168-78.
2. Morimoto, Y.; Takagi, Y.; Saito, T.; Ohta, T.; Ogura, T.; Tohnai, N.; Nakano, M.; Itoh, S., A Bis(mu-oxido)dinickel(III) Complex with a Triplet Ground State. *Angew Chem Int Ed Engl* **2018,** *57* (26), 7640-7643.
3. Cotton, F. A.; Matusz, M.; Poli, R.; Feng, X., Dinuclear formamidinato complexes of nickel and palladium. *Journal of the American Chemical Society* **1988,** *110* (4), 1144-1154.
4. Lee, C.-M.; Chiou, T.-W.; Chen, H.-H.; Chiang, C.-Y.; Kuo, T.-S.; Liaw, W.-F., Mononuclear Ni(II)-Thiolate Complexes with Pendant Thiol and Dinuclear Ni(III/II)-Thiolate Complexes with Ni···Ni Interaction Regulated by the Oxidation Levels of Nickels and the Coordinated Ligands. *Inorganic Chemistry* **2007,** *46* (21), 8913-8923.
5. Berry, J. F.; Bothe, E.; Cotton, F. A.; Ibragimov, S. A.; Murillo, C. A.; Villagran, D.; Wang, X., Metal-metal bonding in mixed valence Ni2(5+) complexes and spectroscopic evidence for a Ni2(6+) species. *Inorg Chem* **2006,** *45* (11), 4396-406.
6. Diccianni, J. B.; Hu, C.; Diao, T., N-N Bond Forming Reductive Elimination via a Mixed-Valent Nickel(II)-Nickel(III) Intermediate. *Angew Chem Int Ed Engl* **2016,** *55* (26), 7534-8.

7. Diccianni, J. B.; Hu, C.; Diao, T., Binuclear, High-Valent Nickel Complexes: Ni-Ni Bonds in Aryl-Halogen Bond Formation. *Angew Chem Int Ed Engl* **2017,** *56* (13), 3635-3639.

8. Shoshani, M. M.; Agapie, T., Ligand architecture for triangular metal complexes: a high oxidation state Ni3 cluster with proximal metal arrangement. *Chem Commun (Camb)* **2020,** *56* (76), 11279-11282.

9. Jacob, S. I.; Douair, I.; Wu, G.; Maron, L.; Menard, G., A tetranuclear nickel cluster isolated in multiple high-valent states. *Chem Commun (Camb)* **2020,** *56* (59), 8182-8185.

10. Wang, R.; Liu, H.; Zhang, K.; Zhang, G.; Lan, H.; Qu, J., Ni(II)/Ni(III) redox couple endows Ni foam-supported Ni2P with excellent capability for direct ammonia oxidation. *Chemical Engineering Journal* **2021,** *404*.

11. Afif, A.; Radenahmad, N.; Cheok, Q.; Shams, S.; Kim, J. H.; Azad, A. K., Ammonia-fed fuel cells: a comprehensive review. *Renewable and Sustainable Energy Reviews* **2016,** *60*, 822-835.

12. Han, Y.; Wu, Y.; Lai, W.; Cao, R., Electrocatalytic Water Oxidation by a Water-Soluble Nickel Porphyrin Complex at Neutral pH with Low Overpotential. *Inorg Chem* **2015,** *54* (11), 5604-13.

13. Wang, D.; Ghirlanda, G.; Allen, J. P., Water oxidation by a nickel-glycine catalyst. *J Am Chem Soc* **2014,** *136* (29), 10198-201.

14. Wang, J.-W.; Hou, C.; Huang, H.-H.; Liu, W.-J.; Ke, Z.-F.; Lu, T.-B., Further insight into the electrocatalytic water oxidation by macrocyclic nickel(ii) complexes:

the influence of steric effect on catalytic activity. *Catalysis Science & Technology* **2017,** *7* (23), 5585-5593.

15. Wang, D.; Bruner, C. O., Catalytic Water Oxidation by a Bio-inspired Nickel Complex with a Redox-Active Ligand. *Inorg Chem* **2017,** *56* (22), 13638-13641.
16. Zhang, L. H.; Yu, F.; Shi, Y.; Li, F.; Li, H., Base-enhanced electrochemical water oxidation by a nickel complex in neutral aqueous solution. *Chem Commun (Camb)* **2019,** *55* (43), 6122-6125.
17. Garrido-Barros, P.; Grau, S.; Drouet, S.; Benet-Buchholz, J.; Gimbert-Suriñach, C.; Llobet, A., Can Ni Complexes Behave as Molecular Water Oxidation Catalysts? *ACS Catalysis* **2019,** *9* (5), 3936-3945.
18. Gutsulyak, D. V.; Piers, W. E.; Borau-Garcia, J.; Parvez, M., Activation of water, ammonia, and other small molecules by PC(carbene)P nickel pincer complexes. *J Am Chem Soc* **2013,** *135* (32), 11776-9.
19. Gu, N. X.; Oyala, P. H.; Peters, J. C., Hydrazine Formation via Coupling of a Nickel(III)-NH2 Radical. *Angew Chem Int Ed Engl* **2021,** *60* (8), 4009-4013.
20. Fisher, K. J.; Feuer, M. L.; Lant, H. M. C.; Mercado, B. Q.; Crabtree, R. H.; Brudvig, G. W., Concerted proton-electron transfer oxidation of phenols and hydrocarbons by a high-valent nickel complex. *Chem Sci* **2020,** *11* (6), 1683-1690.
21. Leban, I.; Gantar, D.; Frlec, B.; Russell, D. R.; Holloway, J. H., Structure of Hexakis(Acetonitrile)Nickel(Ii) Hexafluoroantimonate(V). *Acta Crystallogr C* **1987,** *43*, 1888-1890.
22. Cataldo, F., a Revision of the Gutmann Donor Numbers of a Series of Phosphoramides Including Tepa. *Eur. Chem. Bull* **2015,** *4* (2), 92-97.

23. Waidmann, C. R.; Miller, A. J. M.; Ng, C.-W. A.; Scheuermann, M. L.; Porter, T. R.; Tronic, T. A.; Mayer, J. M., Using combinations of oxidants and bases as PCET reactants: thermochemical and practical considerations. *Energy & Environmental Science* **2012,** *5* (7).

24. Zott, M. D.; Garrido-Barros, P.; Peters, J. C., Electrocatalytic Ammonia Oxidation Mediated by a Polypyridyl Iron Catalyst. *ACS Catalysis* **2019,** *9* (11), 10101-10108.

25. Zott, M. D.; Peters, J. C., Enhanced Ammonia Oxidation Catalysis by a Low-Spin Iron Complex Featuring Cis Coordination Sites. *J Am Chem Soc* **2021,** *143* (20), 7612-7616.

26. Habibzadeh, F.; Miller, S. L.; Hamann, T. W.; Smith, M. R., 3rd, Homogeneous electrocatalytic oxidation of ammonia to N2 under mild conditions. *Proc Natl Acad Sci U S A* **2019,** *116* (8), 2849-2853.

27. Nakajima, K.; Toda, H.; Sakata, K.; Nishibayashi, Y., Ruthenium-catalysed oxidative conversion of ammonia into dinitrogen. *Nat Chem* **2019,** *11* (8), 702-709.

28. Trenerry, M. J.; Wallen, C. M.; Brown, T. R.; Park, S. V.; Berry, J. F., Spontaneous N2 formation by a diruthenium complex enables electrocatalytic and aerobic oxidation of ammonia. *Nat Chem* **2021**.

29. Dunn, P. L.; Johnson, S. I.; Kaminsky, W.; Bullock, R. M., Diversion of Catalytic C-N Bond Formation to Catalytic Oxidation of NH3 through Modification of the Hydrogen Atom Abstractor. *J Am Chem Soc* **2020,** *142* (7), 3361-3365.

30. Holub, J.; Vereshchuk, N.; Sanchez-Baygual, F. J.; Gil-Sepulcre, M.; Benet-Buchholz, J.; Llobet, A., Synthesis, Structure, and Ammonia Oxidation Catalytic

Activity of Ru-NH3 Complexes Containing Multidentate Polypyridyl Ligands. *Inorg Chem* **2021,** *60* (18), 13929-13940.

31. Toda, H.; Kuroki, K.; Kanega, R.; Kuriyama, S.; Nakajima, K.; Himeda, Y.; Sakata, K.; Nishibayashi, Y., Manganese-Catalyzed Ammonia Oxidation into Dinitrogen under Chemical or Electrochemical Conditions*. *Chempluschem* **2021**.

32. Bhattacharya, P.; Heiden, Z. M.; Chambers, G. M.; Johnson, S. I.; Bullock, R. M.; Mock, M. T., Catalytic Ammonia Oxidation to Dinitrogen by Hydrogen Atom Abstraction. *Angew Chem Int Ed Engl* **2019,** *58* (34), 11618-11624.

33. Riddlestone, I. M.; Kraft, A.; Schaefer, J.; Krossing, I., Taming the Cationic Beast: Novel Developments in the Synthesis and Application of Weakly Coordinating Anions. *Angew Chem Int Ed Engl* **2018,** *57* (43), 13982-14024.

34. Hirotsu, M.; Ohno, N.; Nakajima, T.; Kushibe, C.; Ueno, K.; Kinoshita, I., Synthesis and characterization of xanthene-bridged Schiff-base dimanganese(iii) complexes: bimetallic catalysts for asymmetric oxidation of sulfides. *Dalton Trans.* **2010,** *39* (1), 139-148.

35. Perrin, L.; Hudhomme, P., Synthesis, Electrochemical and Optical Absorption Properties of New Perylene-3,4:9,10-bis(dicarboximide) and Perylene-3,4:9,10-bis(benzimidazole) Derivatives. *European Journal of Organic Chemistry* **2011,** *2011* (28), 5427-5440.

36. Lam, K.; Geiger, W. E., Anodic Oxidation of Disulfides: Detection and Reactions of Disulfide Radical Cations. *J. Org. Chem.* **2013,** *78* (16), 8020-8027.

Chapter 4

Homogeneous Electrocatalytic Nitrogen Evolution Reaction Under Aqueous Conditions Using a Polypyridyl Ruthenium Catalyst

4.1 Introduction

A key issue inhibiting the transition from our current fossil fuel economy to a hydrogen fuel economy lies in the production and storage of hydrogen. Hydrogen is the smallest diatomic molecule and will readily leak from various storage containers.[1] Storage of hydrogen by compression or condensation do little to relieve this burden as the compression of hydrogen at room temperature requires a pressure of 750 bars or 150 bars if the temperature is reduced to -196°C.[1] Instead of storing hydrogen in its diatomic state, we can instead use hydrogen generated from water electrolysis in the Haber Bosch process to effectively store it in the form of ammonia.[2]

Ammonia is a hydrogen dense molecule (17.6% w/w) and can be liquified at 20°C with a modest pressure of 8 bars.[3] Because of its utilization in the production of fertilizers, the infrastructure for the physical storage and international transportation of ammonia are already optimized. Ammonia can be cracked to produce hydrogen for use on-site or used in a direct ammonia fuel cell (DAFC).[1, 3-7] While cracking of ammonia to produce hydrogen is attractive because it takes advantage of current hydrogen fuel cell technology, ammonia is cheaper than hydrogen on a source-to-tank basis.[8] A DAFC bypasses the need to install ammonia cracking units at fuel stations and obviates the safety concerns associated with hydrogen.[1]

A variety of DAFCs exist such as solid oxide fuel cells (SOFC), alkaline membrane-based fuel cell (AMFC), and alkaline ammonia fuel cell (AAFC). Several of these fuel cells utilize molten salts by operating at high temperatures and pressures, bypassing the need for the inclusion of a room temperature solvent and making the process of splitting ammonia more facile.[1, 3-7] These systems work well for power plants, but such extreme conditions lose applicability for smaller energy devices (*e.g.*, vehicles). As such, there is a clear need to develop the technology to utilize DAFCs under more ambient conditions which will require a solvent to dissolve the electrolyte (*vide infra*).

The anode and cathode reactions within DAFCs can involve a variety of reactions to generate electricity. However, it is necessary that the oxidation of NH_3 to N_2, nitrogen evolution reaction (NER), occurs at the anode and reduction of O_2, oxygen reduction reaction (ORR), occurs at the cathode. In the cases of SOFC-O and SOFC-H DAFCs, the ORR can either proceed to OH^- or directly to H_2O. Depending on the type of membrane utilized, either OH^- or H^+ ions will cross to further react at the opposite electrode. While thermodynamically feasible, the $6e^-$ oxidation reaction in the NER is kinetically challenging and the bulk of studies have been done with heterogeneous catalysts.[1, 3-13] Recently, substantial progress has been made in the field of molecular catalysts for NER.[14-22] However, currently all molecular electrocatalysts for NER have been studied in aprotic solvents, such as acetonitrile (MeCN) and tetrahydrofuran (THF). While these aprotic solvents are attractive for studying molecular catalysts given their higher solubility, they impose a major issue in the implementation of a DAFC. In a DAFC, the ORR occurring at the cathode must produce OH^- or H_2O (depending on the membrane and conditions); however, in aprotic solvents, oxygen reduction can proceed by either a 2 e^- reduction pathway to produce hydrogen peroxide (H_2O_2) or a 1 e^- reduction pathway to produce superoxide (O_2^-). The production of H_2O_2 is not detrimental to a system, but the reaction is deleterious because the energy provided is far less than direct reduction to H_2O (a loss of 530 mV in MeCN).[23, 24] The production of superoxide, however, can eliminate any energy output from a fuel cell and is known to destroy catalysts and other components utilized in fuel cells.[24-26] As such, a DAFC operating under ambient conditions would require protic solvents such as ammonia or water.

Liquid ammonia provides the highest VED; however, not without several caveats. For instance, the NER has only been studied in liquid NH_3 using heterogeneous catalysts; the solubility of molecular catalysts in liquid NH_3 remains unknown. Liquid NH_3 has higher safety risks than room-temperature solvents and, as such, it is considerably difficult to utilize in academic laboratories where most studies of molecular catalysts occur. Liquid or compressed NH_3 is the ideal choice for large scale fuel cells; however, due to its flammability and toxicity, it is undesirable for use in smaller energy devices.[3, 5-7]

Given the above considerations, we propose that water may be an ideal solvent to utilize for investigating and designing molecular NER electrocatalysts to operate in fuel cells under ambient conditions. An aqueous NH_3 fuel cell provides a cell potential of 1.14 V and while the ORR in water still presents the possibility of H_2O_2 formation, superoxide formation is suppressed.[24] NH_3 has a high solubility in water (~30% w/w) and concentrated aqueous solutions are commercially available and inexpensive. A 30% w/w aqueous NH_3 solution has a gravimetric energy density (GED) of 5.81 MJ/kg and a VED of 5.18 MJ/L. The VED of aqueous NH_3 is either comparable to or larger than compressed H_2 depending on the compression pressure.[3, 6, 27] Aqueous NH_3 is considerably less toxic than anhydrous NH_3 and is non-flammable, further strengthening its prospects as a fuel. Several aqueous NH_3 fuel cells have been reported with respectable cell potentials and peak power densities operating between 25-120 °C.[3, 8, 27] The major concern of aqueous NH_3 fuel cells is the production NO_x species at the anode.[3] As such, an ideal catalyst for the aqueous NER from NH_3 should ideally favor the NER over the formation of NO_x species.

Herein, we report the investigation of a reported polypyridyl ruthenium molecular catalyst (**4.1**) – previously used for the electrocatalytic oxidation of H_2O and chemical catalytic oxidation of NH_3 – and explored its ability to efficiently catalyze the NER under aqueous conditions (Scheme 4.1). We discovered that this catalyst exhibits both high selectivity for N_2 production from the oxidation of NH_3 and exceptionally fast kinetic turnover frequencies under the most realistic NH_3 concentrations for an industrial application for a molecular catalyst.

Scheme 4.1. Molecular ruthenium catalyst studied in this work.

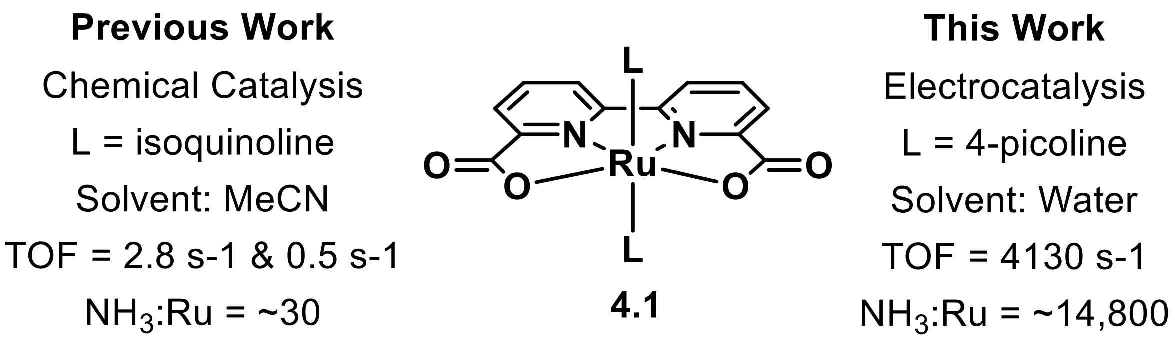

4.2 Results and Discussion

4.2.1 Cyclic Voltammetry and Controlled Potential Coulometry

Cyclic voltammetry of **4.1** in water with NaOTf (0.1 M) as supporting electrolyte at variable scan rates provides a reversible Ru$^{II/III}$ reduction couple at 0.441 V vs. NHE (**Error! Reference source not found.**). Upon addition of NH_3 (14.3 M), a catalytic current is observed indicative of catalytic oxidation of NH_3, with an onset potential of 0.409 V vs.

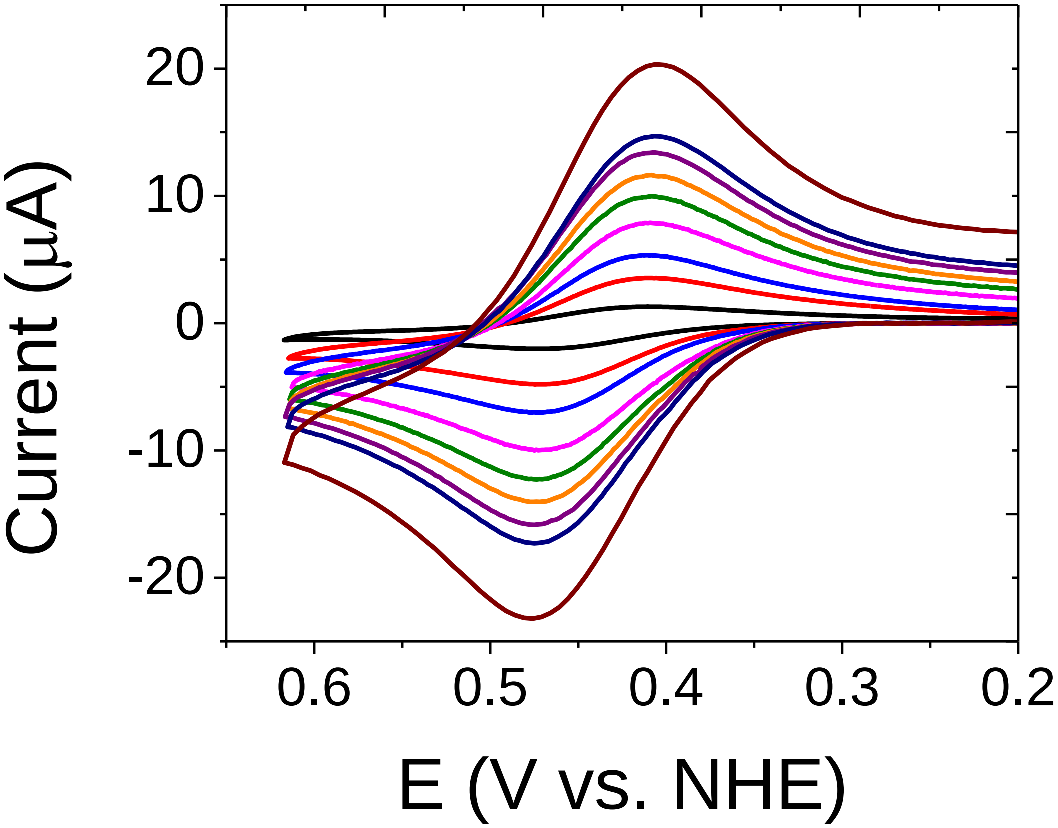

Figure 4.1. Overlaid CVs of 4.1 (1 mM) at variable scan rates of in water with NaOTf (0.1 M) supporting electrolyte. 10 (black), 50 (red), 100 (blue), 200 (pink), 300 (green), 400 (orange), 500 (purple), 600 (navy blue), 1000 mV/s (brown). GC working, Pt counter, and saturated KCl calomel reference electrodes.

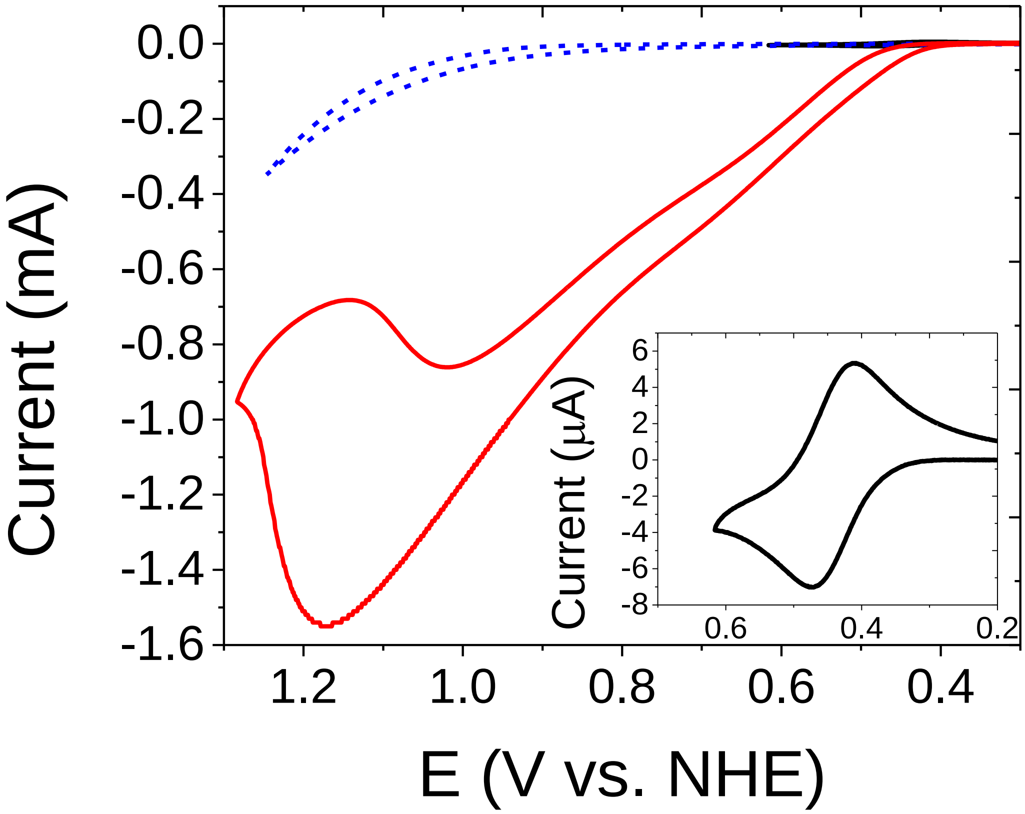

Figure 4.2. CVs of water solutions with NaOTf (0.1 M) as supporting electrolyte at 100 mV/s scan rates containing **4.1** (1 mM) (black trace, inset), **4.1** (1 mM) with NH_3 (14.3 M) (red trace), and NH_3 (14.3 M) only (blue dashed trace). GC working, Pt counter, and saturated KCl calomel reference electrodes.

NHE (Figure 4.2). Controlled potential coulometry (CPC) with a bias held at 0.685 V vs. NHE was performed with **4.1** in water with NH_3 (14.3 M) and NaOTf (0.1 M) as supporting electrolyte. A total charge of 20.4 C was generated over 118 mins. Analysis of the headspace gas by GC-TCD revealed the formation of N_2, H_2, as well as trace O_2 from air leaking through the septa during the injection process (Figure 4.3). The total amount of N_2 produced during the reaction was quantified as the sum of the N_2 measured in the headspace of the cell (determined by GC-TCD) and the N_2 dissolved in solution (determined using Henry's constant for N_2 in water) and provided a faradaic efficiency of 59% and a turnover number of 5.1. The nitrogen peak was corrected for the contribution from air. Analysis of the O_2 peak before and after CPC from the GC-TCD measurement indicated that the oxygen evolution reaction does not occur to a detectable

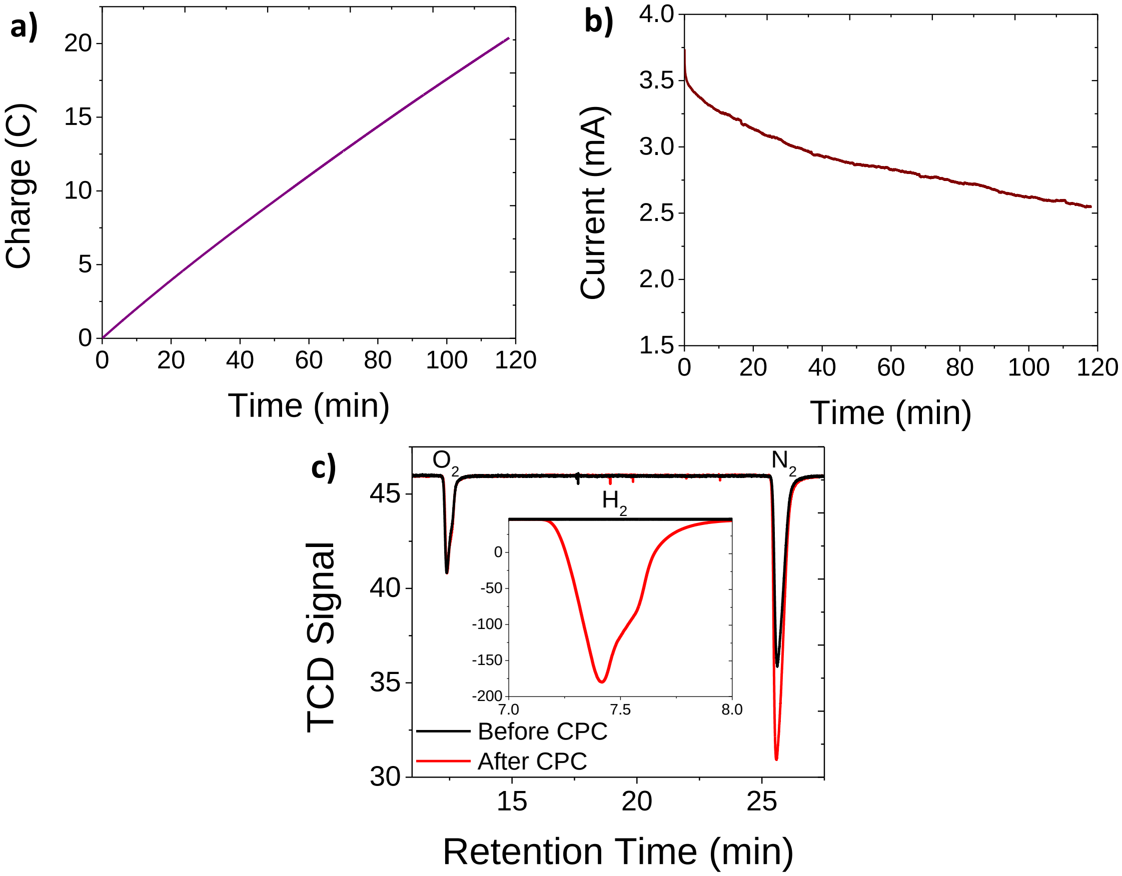

Figure 4.3. CPC data corresponding to a 2-hour catalytic experiment with an applied potential of 0.685 V vs. NHE with **4.1** (1 mM) and NaOTf (0.1 M) supporting electrolyte in NH_4OH (NH_3 14.3 M). (a) Charge vs time, (b) current vs. time, (c) TCD signal from injection of 100 μL of headspace from the electrolysis cell before (black trace) and after (red trace) CPC.

amount in the presence of a high concentration of NH_3 (Figure 4.3C). Similar conditions were repeated twice more with the same concentration of catalyst, for which faradaic efficiencies of 61% and 46% with respective turnover numbers of 6.5 and 5.5 were obtained. This data is summarized in Table 4.1.

Table 4.1. Results of catalytic CPC experiments performed for NER. BDL = below detection limit.

Entry	[Ru] (mM)	[NH4] (M)	Charge (C)	TON	FE N2 (%)	Time (min)	E_{app} (V)
1	1	0	20.4	5.1	59	118	0.685
2	1	0	30.8	6.5	61	180	0.685
3	1	0	35.1	5.5	46	180	0.685
4	1	1	20.1	8.2	94	26	0.685
5	1	1	20.0	7.8	90	27	0.685
6	1	1	20.1	7.2	83	28	0.685
7	1	1	27.3	10	84	70	0.530
8	none	1	4	n/a	BDL	878	0.685

For our electrolysis cell, the working and counter electrodes are not separated from each other for the purpose of minimizing the volume of the cell. For a single compartment cell to provide reliable data for catalytic NER, the concentration of protons must be high enough for the counter electrode to produce enough H_2 to compensate the current passed at the working electrode. We hypothesized that the low and inconsistent faradaic efficiencies obtained for **4.1** were due to the low concentration of $[NH_4^+]$ in the solution. Ammonia has a low acid dissociation constant ($K_b = 1.77 \times 10^{-5}$) and a 14.3 M solution of aqueous ammonia provides an $[NH_4^+]$ concentration of 16 mM. Due to the low $[NH_4]$, side reactions likely occurred at the counter electrode to offset the large currents measured at the working electrode. The products from such side reactions could then react further at the working electrode contributing to total measured current. To test this hypothesis, we added NH_4OTf (1 M) to the subsequent experiments.

The CV of **4.1** in water with NH_4OTf (1 M) and NaOTf (0.1 M) as supporting electrolyte provides a reversible $Ru^{II/III}$ couple at 0.572 V vs. NHE (Figure 4.4 inset), 0.131 V more positive than in the absence of NH_4OTf. A large catalytic current is observed in the presence of NH_3 (14.3 M) with an onset potential of 0.497 V vs. NHE (Figure 4.4), 0.088 V more positive than in the absence of NH_4OTf. CPC of **4.1** with an applied potential of 0.685 V vs. NHE in water with NH_3 (14.3 M), NH_4OTF (1 M), and NaOTf (0.1 M) as supporting

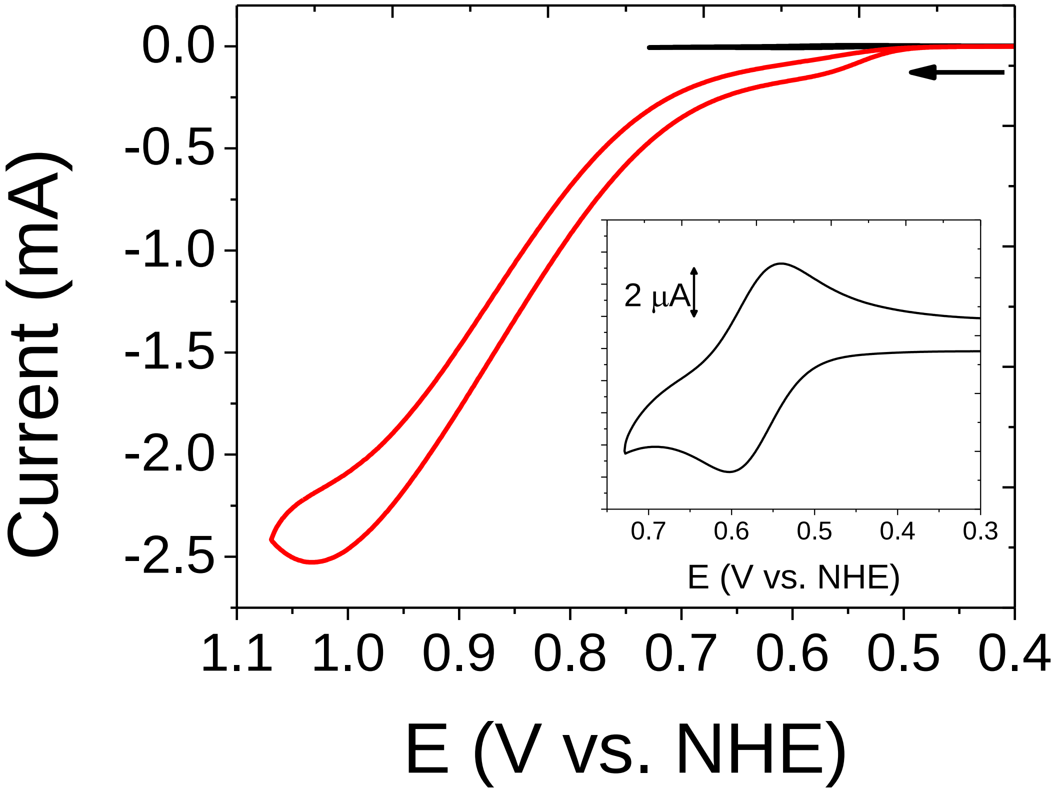

Figure 4.4. CVs of **4.1** (1 mM) with NH_4OTf (1 M), and NaOTf (0.1 M) as supporting electrolyte in water (black trace, inset) and with NH_3 (14.3 M) (red trace). GC working, Pt counter, and saturated KCl calomel reference electrodes.

electrolyte produced 20.1 C of charge over 26 min with a faradaic efficiency of 94% and a TON of 8.2 (Figure 4.5, entry 4 in Table 4.1). The same conditions were repeated twice more with the same concentration of **4.1** for which faradaic efficiencies of 90% and 83% with respective turnover numbers of 7.8 and 7.2 were obtained. This data is summarized in Table 4.1 (entries 4-6).

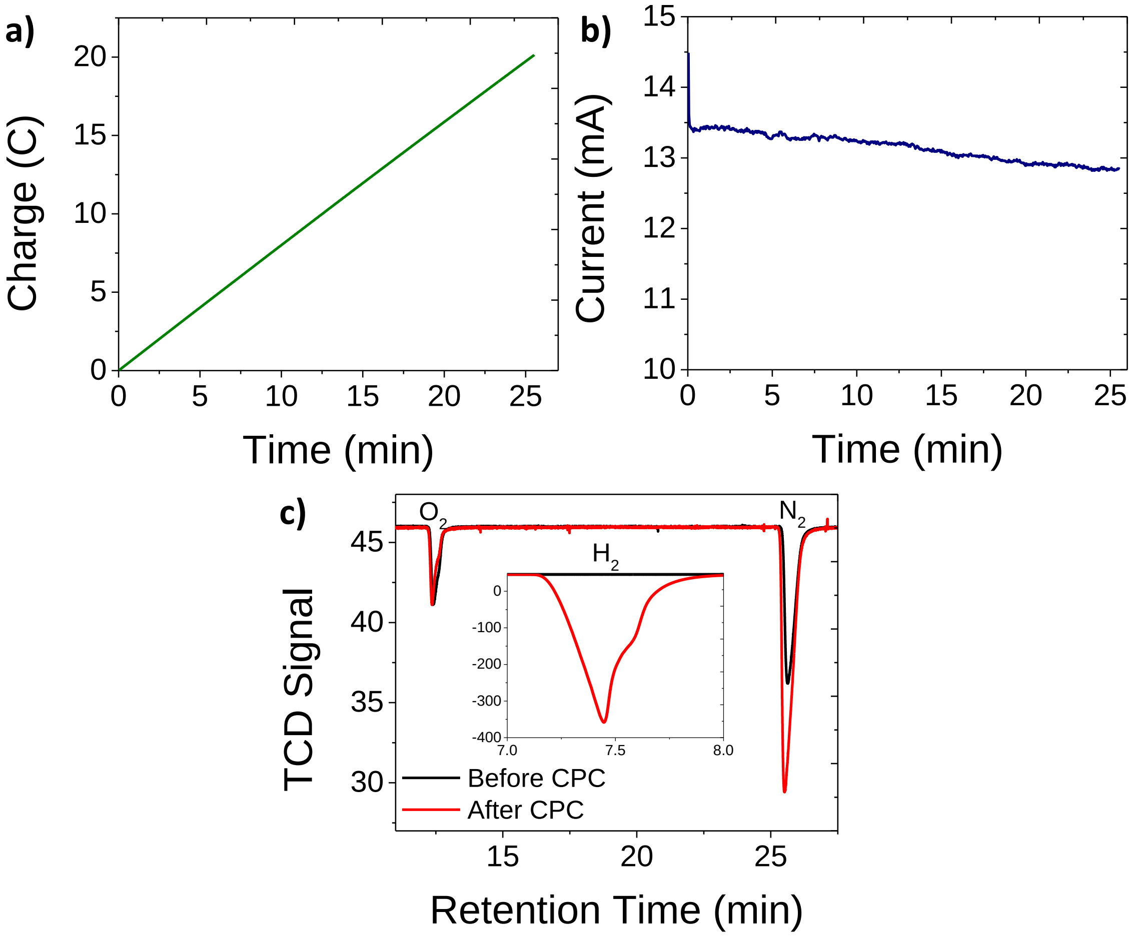

Figure 4.5. CPC data corresponding to a 26-minute catalytic experiment with an applied potential of 0.685 V vs. NHE with **4.1** (1 mM), NH_4OTf (1 M), and NaOTf (0.1 M) supporting electrolyte in NH_4OH (NH_3 14.3 M). (a) Charge vs time, (b) current vs. time, (c) TCD signal from injection of 100 µL of headspace from the electrolysis cell before (black trace) and after (red trace) CPC.

4.2.2 Reaction Mechanism and Kinetics

Typically, molecular catalysts for NER will operate by either an ammonia nucleophilic attack (ANA) or by an interaction of two metal-nitrogen ligands (I2N). The elucidation of such mechanisms can be interrogated by raising the concentration of the substrate (NH_3) such that the reaction is pseudo-first order in concentration of the catalyst. To gain insight into the mechanism, we performed sequential 100 mV/s scan rates with variable concentrations of **4.1** (0.25 mM – 1 mM) in water with ~14,800 – 59,200 equivalents of NH_3 (14.3 M), NH_4OTf (1 M), and NaOTf (0.1 M) as the supporting electrolyte (Figure 4.6A). A plot of i_{cat} vs. [**4.1**] (i_{cat} is the plateau current generated by the catalyst in the presence of substrate) shows a linear relationship (Figure 4.6B). The slope of the plot in Figure 4.6B depends on the reaction mechanism such that the rate of an ANA mechanism is first order in [Ru] and second order in [Ru] for an I2N mechanism. The catalytic current is proportional to the rate constant (*vide infra*) and therefore the linear relationship between i_{cat} and [Ru] observed in Figure 4.6B is indicative of an ANA mechanism. Such a phenomenon is rare for RuBda catalysts as they commonly operate via a bimolecular mechanism for catalytic water oxidation[28-31] and were previously reported to chemically catalyze the oxidation of NH_3 via an I2N mechanism by Nishibayashi and coworkers in acetonitrile using magic blue as a sacrificial oxidant (*vide infra*). However, RuBda catalysis via single site mechanisms is not novel and the complexes can convert between bimolecular and unimolecular mechanisms depending on ligand modification, surface attachment, etc.[32-34] We note that the catalytic current increases upon addition of NH_4^+ indicating an increase in reaction rate (*vide infra*). Berry and coworkers recently reported a dinuclear ruthenium catalyst for which the reaction rate decreased upon addition of NH_4^+ for which they attribute to the rate-determining step (RDS) involving a deprotonation. In the case of **4.1**, the increased rate suggests that deprotonation is not part of the RDS. Because of this, we hypothesize that the RDS likely involves N–N bond formation and the process is sped up in the presence of NH_4.

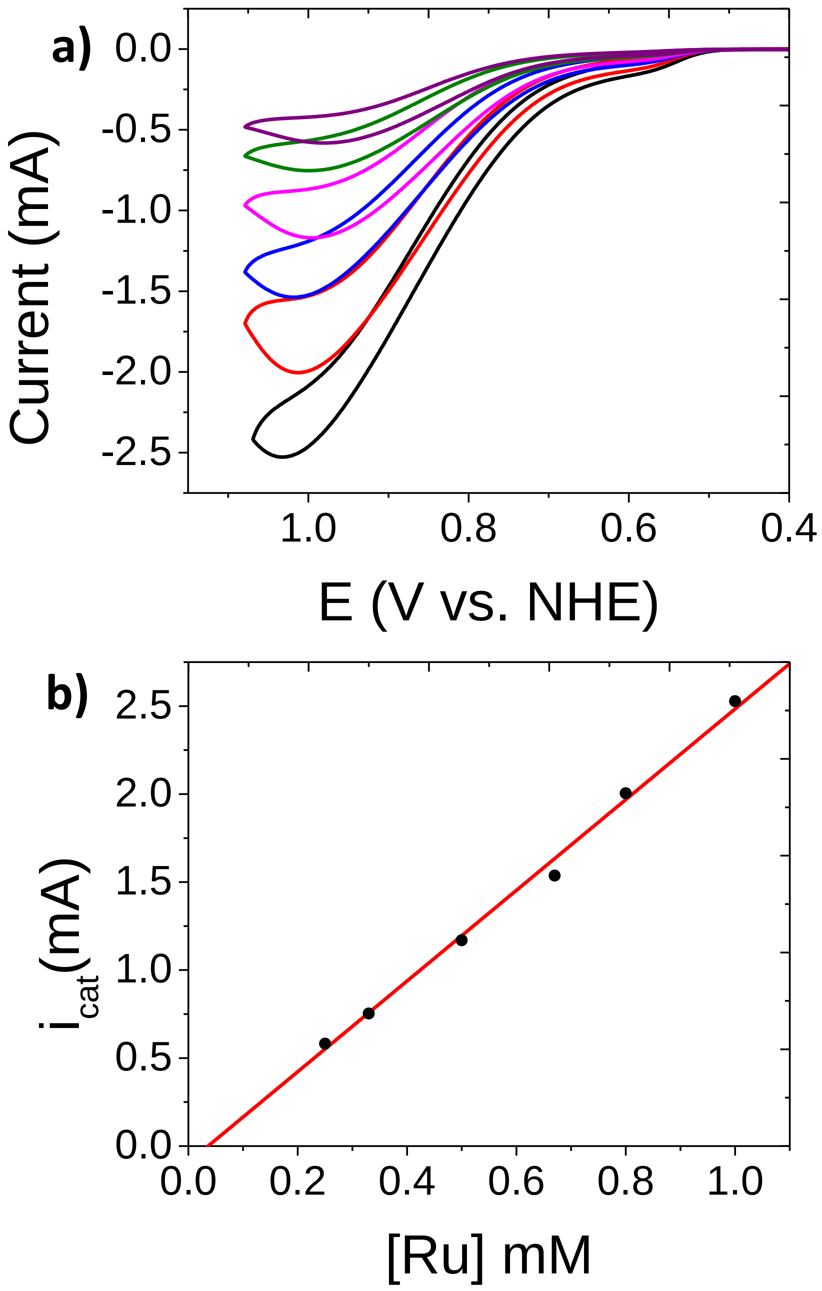

Figure 4.6. a) CVs of **4.1** at variable concentrations at 100 mV/s. [**4.1**] = 1 mM (black), 0.80 mM (red), 0.67 mM (blue), 0.50 mM (pink), 0.33 mM (green), and 0.25 mM (purple). Glassy carbon working, Pt wire counter, and saturated KCl calomel reference electrodes. b) Plot of i_{cat} vs concentration of **4.1** with $R^2 = 0.9963$

The CVs in Figures 4.2 and 4.4 both reveal two separate catalytic events. Figure 4.7A shows the CV of **4.1** with wider potential window revealing the subsequent $Ru^{III/IV}$ couple of the ruthenium catalyst. Overlaid with this CV is the addition of NH_3 with the currents normalized to enable better comparison and it is noteworthy that at the onset of the $Ru^{III/IV}$ couple (Figure 4.7A, black trace), we observe the slope of the catalytic current change significantly in the presence of NH_3 (Figure 4.7A, red trace). These distinct events are more easily visualized from the differential pulse voltammogram (DPV) of **4.1** under the respective conditions for which we differentiate the catalytic events as E1 and E2 (Figure 7B). The catalytic nature of E1 is evident from the current ratio in the presence and absence of NH_3; however, it is not immediately explicit what the catalytic reaction is. Our previous CPC experiments were performed with an applied potential of 0.685 V vs. NHE which coincided with the E2 catalytic event. To evaluate the nature of the E1 catalytic event for NER, we performed CPC to distinctly target the E1 event (Figure 4.7C).

CPC of **4.1** (1 mM) with an applied potential of 0.530 V vs. NHE in water with NH_3 (14.3 M), NH_4OTF (1 M), and NaOTf (0.1 M) as supporting electrolyte generated 27.3 C of charge in 70 mins with a faradaic efficiency of 84% and a TON of 10 (Figure 4.8 and entry 7 in Table 4.1). Albeit slower than E2, this confirms that E1 is catalytic for the NER. Given the abrupt change in the slope upon applying potentials for which the $Ru^{III/IV}$ couple would be accessed, the difference in currents between E1 and E2 could be due to the catalyst accessing higher potentials more reactive for NER, perhaps indicating an alternative mechanism. Interestingly, the CVs reported by Nishibayashi for the same catalyst with isoquinoline axial ligands show a similar catalytic curve in acetonitrile for which two distinct catalytic slopes are observed.

However, they do not comment on this feature and provide DFT evidence supporting an I2N mechanism.

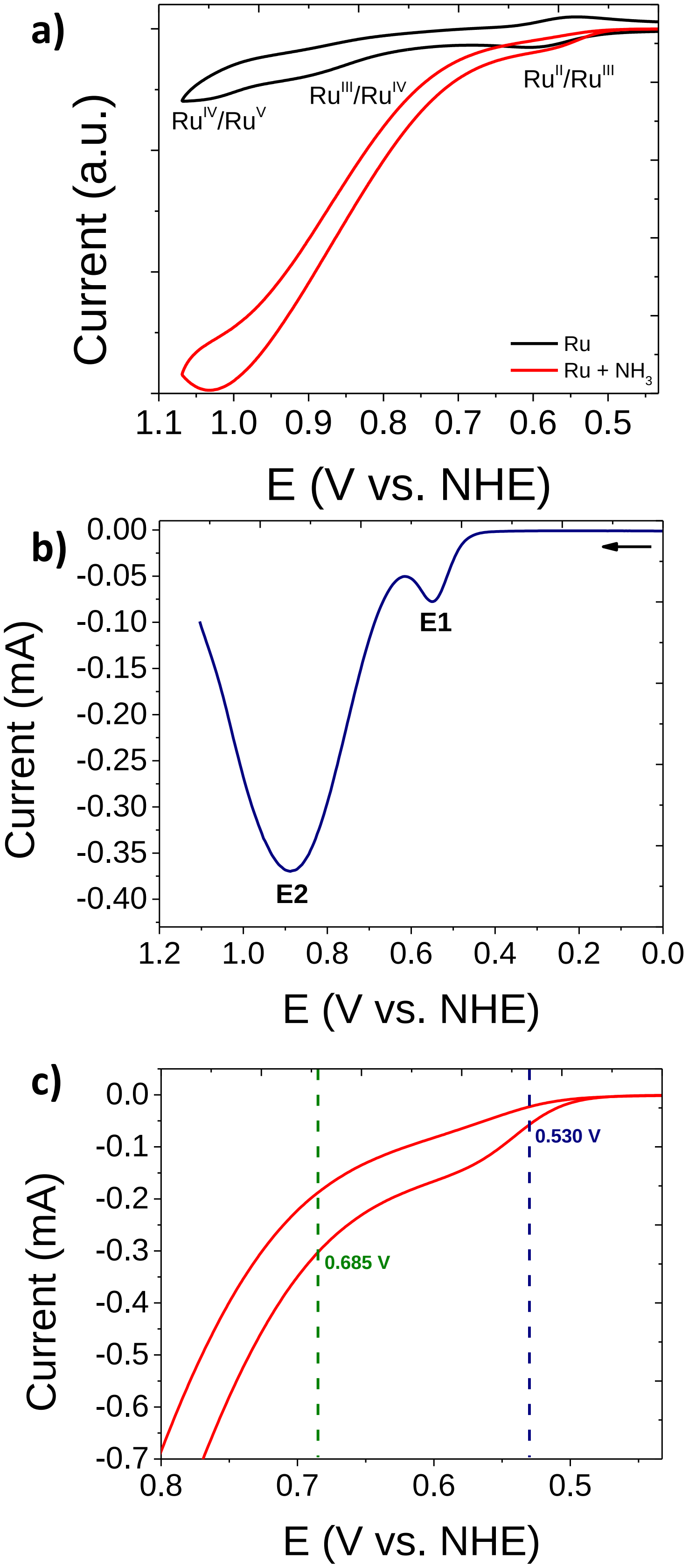
a)
Current (a.u.)
Ru^{IV}/Ru^{V}
Ru^{III}/Ru^{IV}
Ru^{II}/Ru^{III}
Ru
Ru + NH_3
1.1
1.0
0.9
0.8
0.7
0.6
0.5
E (V vs. NHE)
b)
Current (mA)
0.00
-0.05
-0.10
-0.15
-0.20
-0.25
-0.30
-0.35
-0.40
E1
E2
1.2
1.0
0.8
0.6
0.4
0.2
0.0
E (V vs. NHE)
c)
Current (mA)
0.0
-0.1
-0.2
-0.3
-0.4
-0.5
-0.6
-0.7
0.530 V
0.685 V
0.8
0.7
0.6
0.5
E (V vs. NHE)

Figure 4.7. (a) CV overlay of **4.1** (1 mM) in water with NH_4OTf (1 M) and NaOTf (0.1 M) (black trace) and in the presence of NH_3 (14.3 M) (red trace). The current of the red trace was normalized by dividing by 17 to better comparison. (b) DPV of **4.1** (1 mM), NH_3 (14.3 M), NH_4OTf (1 M), and NaOTf (0.1 M) in water. Both catalytic peaks are marked by either E1 or E2. (c) Zoomed in CV of **4.1** (1 mM), NH_3 (14.3 M), NH_4OTf (1 M), and NaOTf (0.1 M) in water with dashed lines marking the potentials applied for CPC experiments.

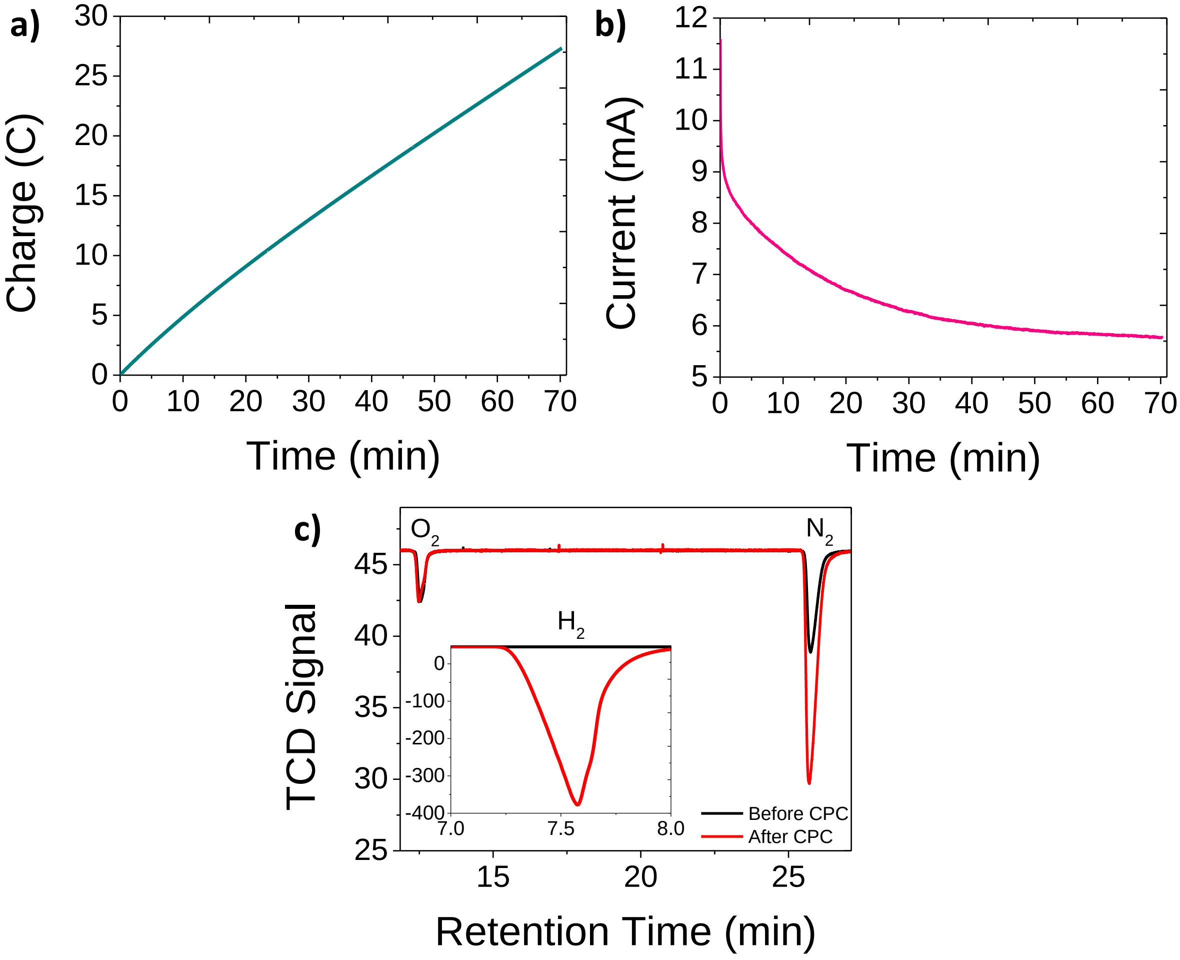

Figure 4.8. CPC data corresponding to a 70-minute catalytic experiment with an applied potential of 0.530 V vs. NHE with **4.1** (1 mM), NH_3 (14.3 M), NH_4OTf (1 M), and NaOTf (0.1 M) as supporting electrolyte in water. (a) Charge vs time, (b) current vs. time, (c) TCD signal from injection of 100 μL of headspace from the electrolysis cell before (black trace) and after (red trace) CPC.

Given the single site mechanism, we estimated the turnover frequency (TOF) of **4.1** using the method of plateau current analysis (equations 1-4).[35, 36] The utilization of plateau current analysis is made possible if the concentration of the substrate is high enough such that the catalytic reaction is pseudo first-order in terms of the concentration of the catalyst and S-shape peaks can be obtained for which their current magnitude is independent of the scan-rate.

$$i_{cat} = nFA[cat]\sqrt{Dk_{cat}} \tag{1}$$

$$i_p = 0.4463n_pFA[cat]\sqrt{\frac{n_pFvD}{RT}} \tag{2}$$

$$\frac{i_{cat}}{i_p} = \frac{n_{cat}}{0.4463n_p}\sqrt{\frac{RTk_{cat}}{n_pFv}} \tag{3}$$

$$k_{cat} = 5.533x10^{-3}\frac{FM^2}{RT} \tag{4}$$

From equation 1, i_{cat} is the plateau current generated by the catalyst in the presence of substrate, n is the number of electrons used for one turnover of the catalytic reaction, F is Faraday's constant, A is the area of the electrode, [cat] is the concentration of the catalyst in solution, D is the diffusion coefficient, and k_{cat} is the pseudo-first-order rate constant.

Knowledge of the diffusion coefficient of a catalyst and surface area of an electrode can be avoided by dividing the plateau current, i_{cat}, by the peak current, i_p, in the absence of substrate. From the Randles-Sevcik equation, the value of i_p is represented by the variables in equation 2. From equation 2, n_p is the number of electrons transferred from the working electrode to the catalyst in the absence of substrate, R is the universal gas constant, T is the temperature, and *v* is the scan rate. Dividing the catalytic current, i_{cat}, by the current in the absence of substrate, i_p, yields equation 3 which utilizes variables that are more facile to obtain.

S-shape cyclic voltammograms with plateau currents independent of the scan rate were obtained for **4.1** in water with NH_3 (14.3 M), NH_4OTf (1 M), and NaOTf (0.1 M) as supporting electrolyte at variable scan rates (Figure 4.9A). To ensure reproducibility and reliability, the electrode was polished between every scan.[37] Attempts to collect CVs at scan rates slower than 100 mV/s were unsuccessful due the rapid bubble formation at the face of the glassy carbon working electrode. Plotting the ratio of the i_{cat} and i_p as a function of the inverse of the square root of the scan rate, we observed a linear relationship with an R^2 of 0.999 and a slope of 137.5 (Figure 4.9B). Equation 3 can be further simplified by assigning $(i_{cat}/i_p)^2/\nu$ as the slope, designated as M, from Figure 4.10 and by assigning n_p and n_{cat} to be 1 and 6 respectively to obtain equation 4. From equation 4, we estimated a TOF of 4130 s^{-1} using the slope (137.5) extracted from Figure 4.10.

Using the same method just described, we estimated the TOF of **4.1** for its catalytic oxidation of NH_3 in the absence of NH_4OTf. While the CV traces observed in the absence of NH_4OTf did not conform to a classic S-shape, plateau currents independent of the scan rate were observed between 100 mV/s and 600 mV/s (Figure 4.10A). The ratio of the i_{cat} and i_p as a function of the inverse of the square root of the scan rate (Figure 4.10B) provided a slope of 70, from which we estimated the TOF to be 1065 s^{-1} with equation 4. Interestingly, the addition of NH_4OTf multiplies TOF of the **4.1** by about four.

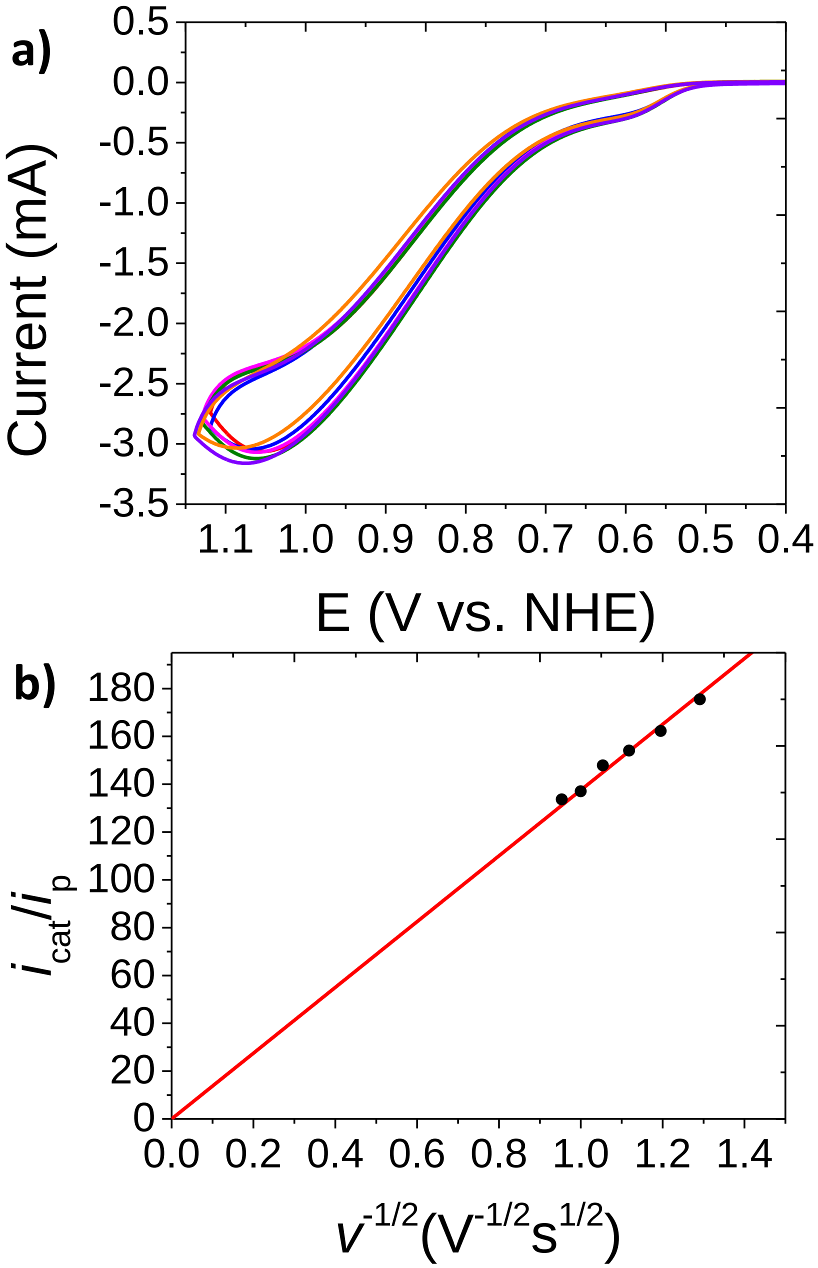

Figure 4.9. (a) CVs of **4.1** (1 mM) in water with NH_3 (14.3 M), NH_4OTf (1 M), and NaOTf (0.1 M) as supporting electrolyte at variable scan rates of 600 (red), 700 (blue), 800 (pink), 900 (green), 1000 (orange), and 1100 (purple) mV/s. GC working, Pt counter, and saturated KCl calomel reference electrodes. (b) Plot of i_{cat}/i_p as a function of $v^{-1/2}$ providing a linear relationship. The red line is forced to adhere to the origin.

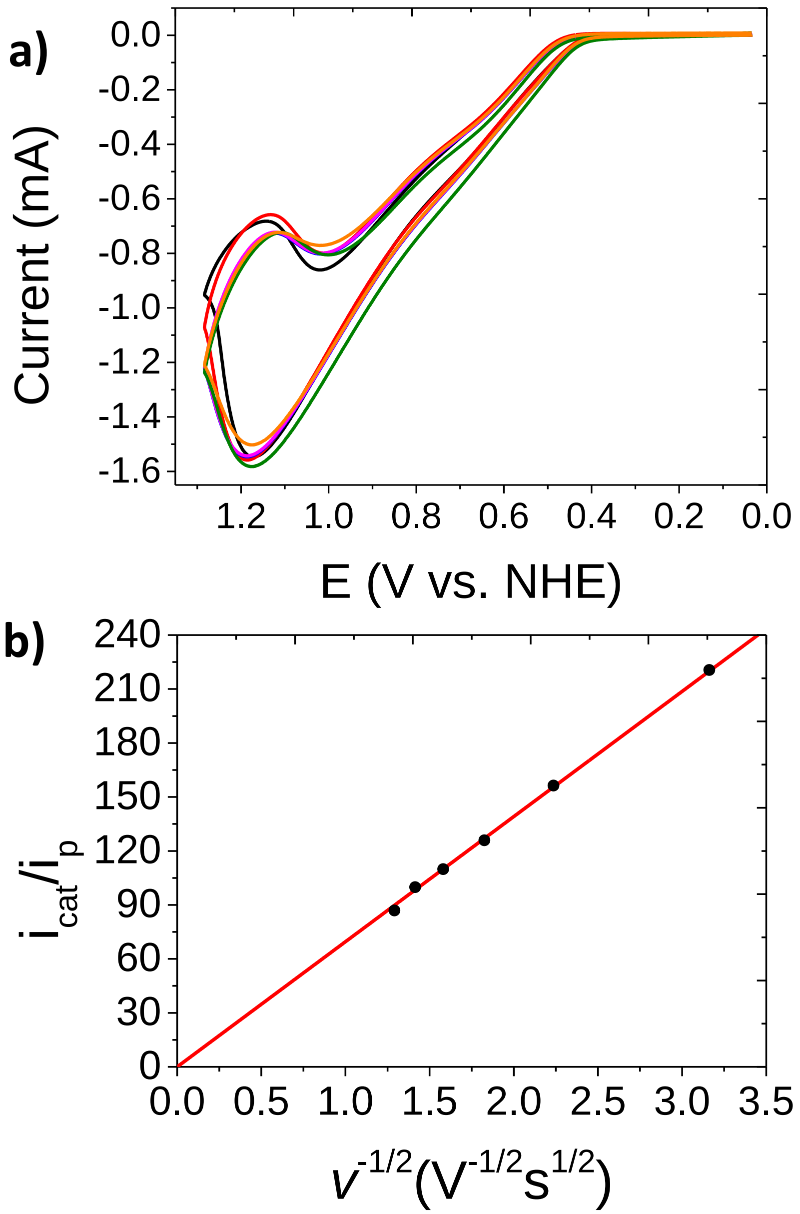

Figure 4.10. (a) CVs of **4.1** (1 mM) in water with NH_3 (14.3 M) and NaOTf (0.1 M) as supporting electrolyte at variable scan rates of 100 (black), 200 (red), 300 (blue), 400 (pink), 500 (green), and 600 mV/s (orange). GC working, Pt counter, and saturated KCl calomel reference electrodes. (b) Plot of i_{cat}/i_p as a function of $v^{-1/2}$ providing a linear relationship. The red line is forced to adhere to the origin.

4.2.3 Foot of the Wave Analysis (FOWA)

The TOF of an electrocatalyst is commonly estimated by using a variety of methods such as currents independent of the scan rate (*vide supra*) or foot-of-the-wave analysis (FOWA).[35, 37-40] FOWA is a method that allows the estimation of a rate constant for a catalytic reaction for cases that a non-ideal S-shape curve is observed by cyclic voltammetry. In such cases it is assumed that side phenomena are occurring, such as substrate depletion, catalyst deactivation, product inhibition, etc. FOWA can be utilized to estimate the kinetics of a catalytic reaction with side-phenomena by analyzing the currents at the foot of the catalytic wave where the forward and reverse CV traces overlay to the ideal S-shape.

For a FOWA to provide a TOF, the first step of the reaction must be the rate determining step. Otherwise, a FOWA provides a rate constant for k_1 if it is a multi-step reaction. Without a proper mechanistic analysis, it should be assumed that a FOWA is providing a rate constant for k_1 and not a TOF.[35, 41-43] While such an analysis is unnecessary for our system, some of the previously reported rate constants for molecular NER electrocatalysts were calculated with a FOWA.[14, 20] Therefore we performed the calculation to compare the k_1 of our system with the k_1 rate constants reported in the literature.

The FOWA calculation requires knowledge of the catalytic reaction mechanism being analyzed. Our results indicate that **4.1** undergoes an ANA mechanism for the oxidation of ammonia to nitrogen (*vide supra*); therefore, we employed a FOWA using equation 5.[40]

$$\frac{i_{cat}}{i_p} = \frac{n \cdot 2.24\sqrt{\frac{RT}{Fv}}k_{obs}}{1 + exp\frac{F(E^\circ - E)}{RT}} \qquad (5)$$

From equation 5, i_{cat} is the catalytic current, i_p is the anodic peak potential estimated from the $Ru^{II/III}$ couple, n is the number of electrons involved in the catalytic reaction which we assigned as 6, R is the universal gas constant, T is temperature, F is Faraday's constant, *v* is the scan rate, E° is the midpoint potential of the catalytic event, E is the applied potential, and k_{obs} is the pseudo first order rate constant for the reaction.

We performed FOWA on scan rates utilized in the previous method that displayed plateau currents independent of the scan rate. Figure 4.11 shows an example of the potential window selected for the FOWA, the midpoint potential of the catalytic current, and the data used for fitting at 600 mV/s. The potentials that FOWA was performed on was kept constant

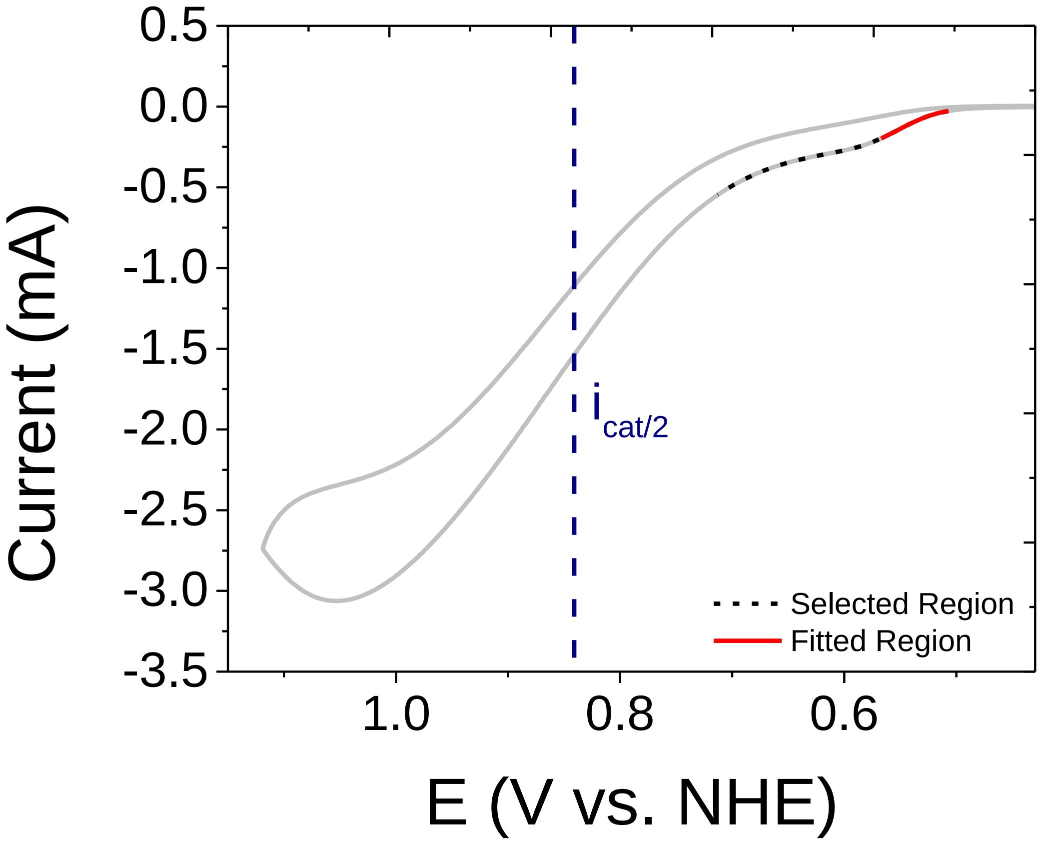

Figure 4.11. CV of **4.1** (1 mM), NH_3 (14.3 M), NH_4OTf (1 M), and NaOTf (0.1 M) in water at 600 mV/s. The black dashed trace shows the data used for performing the FOWA, the red

solid trace shows the data used for fitting the slope, and the vertical navy-blue dashed line represents the E° value used in the FOWA calculation.

for the 600, 700, 800, 900, 1000, and 1100 mV/s scan rates. The slopes obtained from the FOWA plots, an example of the 600mV/s analysis is shown in Figure 4.12, were utilized in equation 5 to calculate the k_{obs}. Each of the k_{obs} values were plotted against the natural log of the scan rate (Figure 4.13) to ensure that the rate was independent of the scan rate. The results were averaged and the apparent pseudo-first order rate constant $k_{obs} = 4.33\text{x}10^{10}$ s^{-1} was obtained for **4.1**. From the k_{obs} we obtain the apparent second order rate constant $k_1 = 2.93\text{x}10^9$ $M^{-1}s^{-1}$ that is of the same order of magnitude to fastest rate constant reported for molecular iron NER catalysts.[20] We note that the rate estimated for **4.1** using FOWA is orders of magnitude larger than what was estimated by the plateau current analysis. Such a case is not novel as there are reports of rate constants determined by FOWA and plateau current analysis for the same catalyst that differ by orders of magnitude.[44, 45] The k_1 calculated for **4.1** by the FOWA allows for wider comparison with other molecular catalysts for NER, however, the 4130 s^{-1} rate constant calculated from the plateau currents does reflect the TOF of **4.1** under the conditions provided in this work.

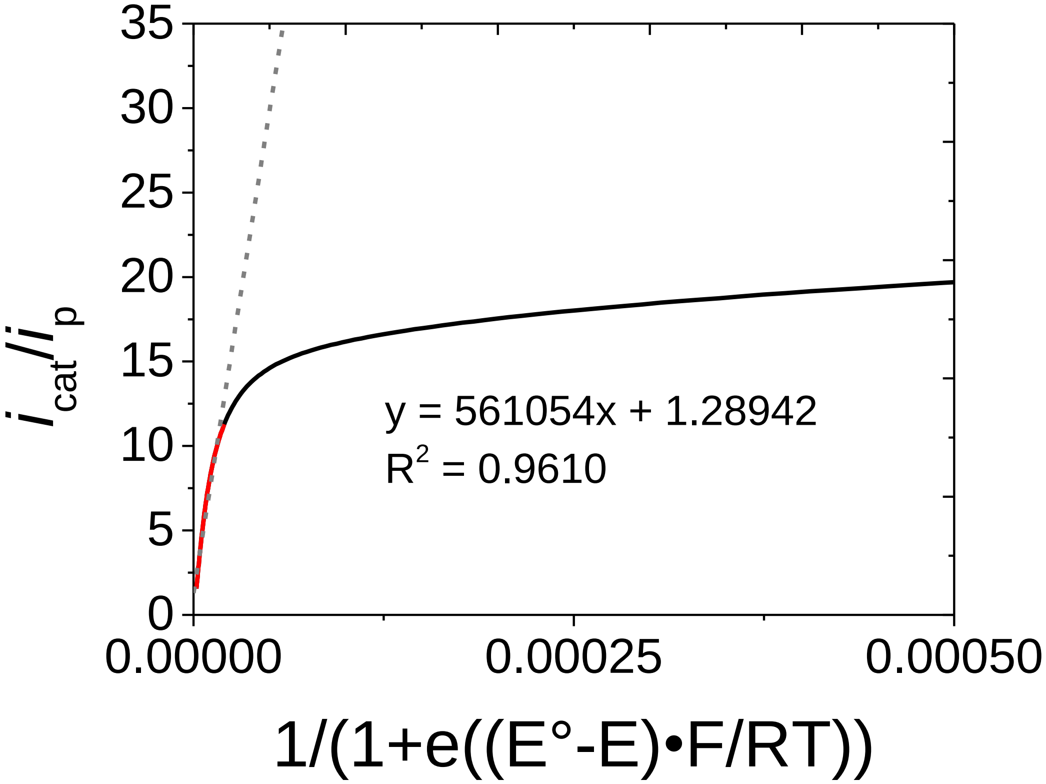

Figure 4.12. FOWA plot of an ANA mechanism calculated from the CV shown in Figure 4.11.

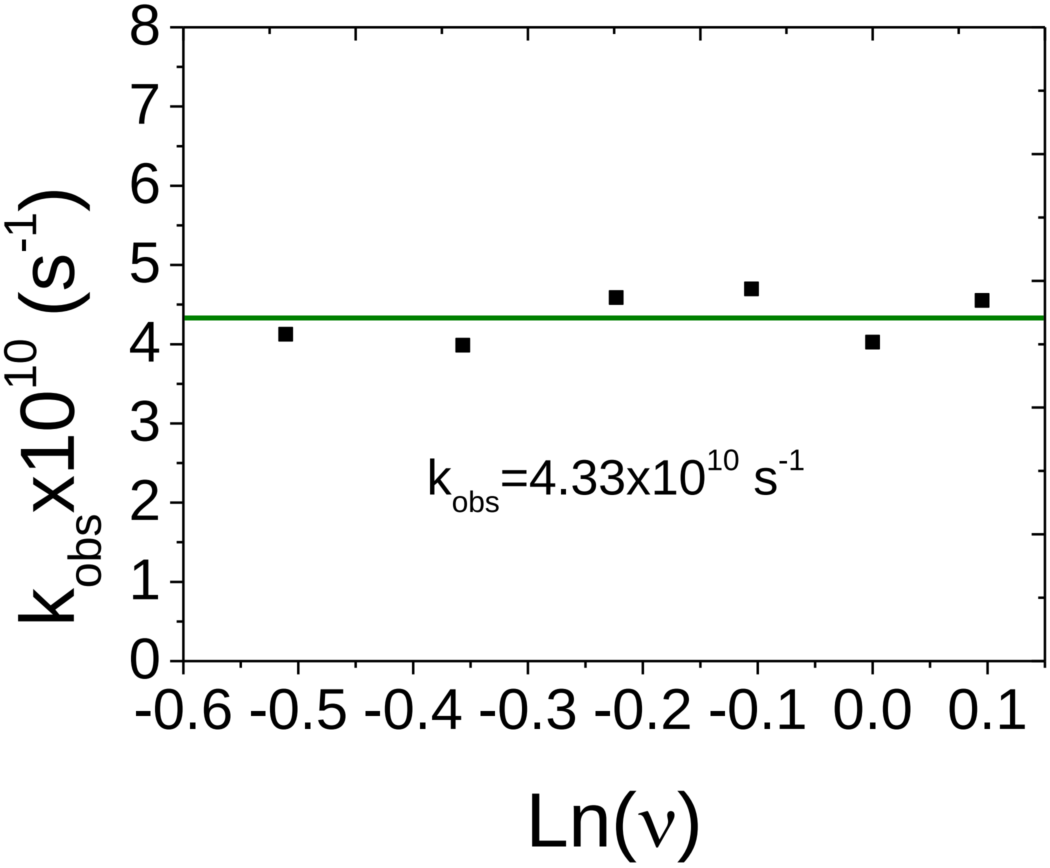

Figure 4.13. Plot of the k_{obs} determined by FOWA from CVs of **4.1** (1 mM), NH_3 (14.3 M), NH_4OTf (1 M), and NaOTf (0.1 M) in water at varied scan rates vs the natural logarithm of the scan rate. An average $k_{obs} = 4.33 \times 10^{10}$ s^{-1} was obtained and is marked by a horizontal green line in the plot.

4.2.4 Investigation of Catalyst Stability

To further elucidate the prospects of **4.1** as an aqueous NER catalyst, we interrogated its stability under high concentrations of aqueous NH_3. For this we wanted to evaluate its stability under catalytic and ambient conditions. To evaluate its catalytic stability, we performed a rinse test on the glassy carbon rod working electrode post electrolysis (entry 4 in Table 4.1). After the electrolysis with **4.1**, we rinsed the glassy carbon rod with water and acetone, and immediately took CVs with the electrode in a fresh ammonia solution with the same electrolyte in the absence of **4.1** (Figure 4.14). From Figure 4.14 it is notable that there is not a significant change in current magnitude between the rinsed electrode and a freshly polished electrode, which is indicative that a catalytically active heterogeneous species is not strongly deposited onto the electrode during CPC.

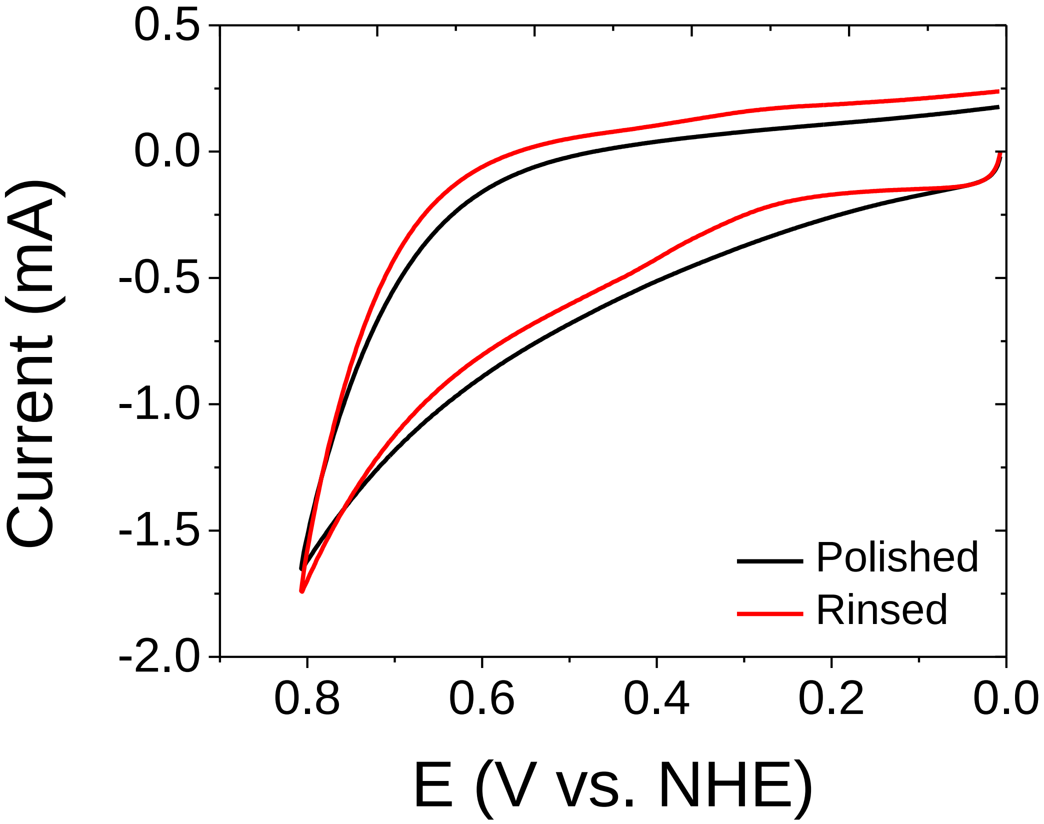

Figure 4.14. CVs of polished glassy carbon rod electrode and the same electrode rinsed with water and acetone after CPC, recorded in water with NH_3 (14.3 M), NH_4OTf (1 M), and NaOTf (0.1 M). Pt counter and saturated KCl calomel reference electrodes. Prior to this measurement, the working electrode was subjected to a CPC experiment containing **4.1** (table 4.2, entry 4).

Next, 100 consecutive CV sweeps were taken of the same solution containing **4.1** post electrolysis (entry 4 in Table 4.2) at 100 mV/s to further confirm its catalytic stability (Figure 4.15A). The catalytic response does not exhibit novel features that were not observed by CV prior to CPC. We note that the magnitude of the plateau current observed in Figure 4.16 seems to arbitrarily decrease and increase between cycles; however, this is due to the observed formation of bubbles at the surface of the electrode during the static experiment that can be seen with the naked eye (Figure 4.15B). As such, it does not appear that a heterogeneous catalytic species is deposited on the electrode during a static experiment either.

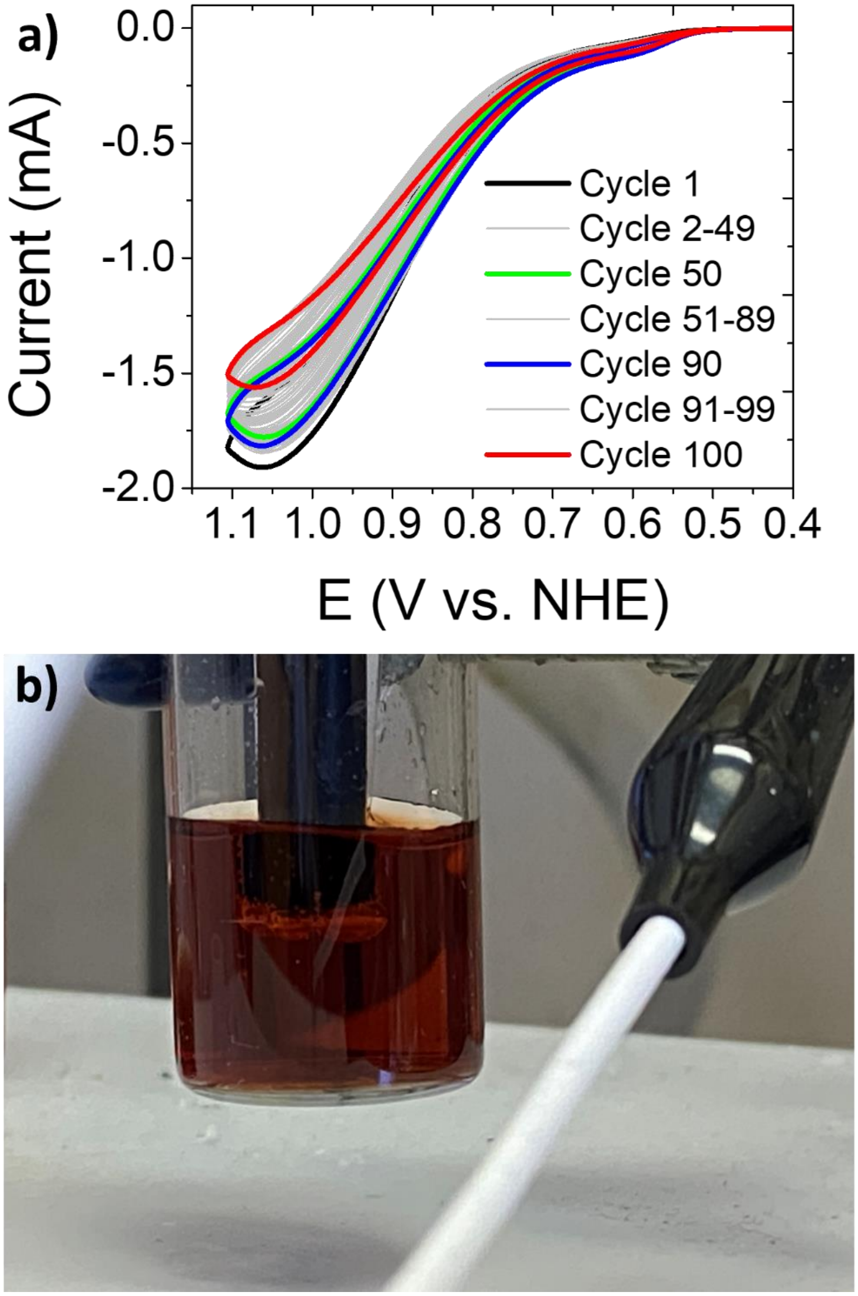

Figure 4.15. (a) 100 CV sweeps of 4.1 at 100 mV/s post-CPC (Table 4.1, entry 4). (b) Picture taken during the 100 CV cycles. Bubbles of N2 are observed to form at the face of the glassy carbon working electrode.

For ambient conditions we dissolved 3.78 μmol of **4.1** in 750 μL in D_2O with dissolved ND_3 (ND_3 25-30%) and took a ^{1}H NMR (Figure 4.16 top). Upon dissolution in the presence of ammonia, the complex loses symmetry and exhibits six proton signals related to the bipyridine ligand instead of three when dissolved in DMSO (Figure 4.17). This is due to coordination of ammonia at the ruthenium center causing one of the carboxylate groups to dissociate. The NMR spectrum of the same solution after 36 days exhibits the same asymmetry for the bipyridine protons and the methyl protons from the axial ligands still integrate to 6 (Figure 4.16 bottom). The clean NMR spectra are indicative

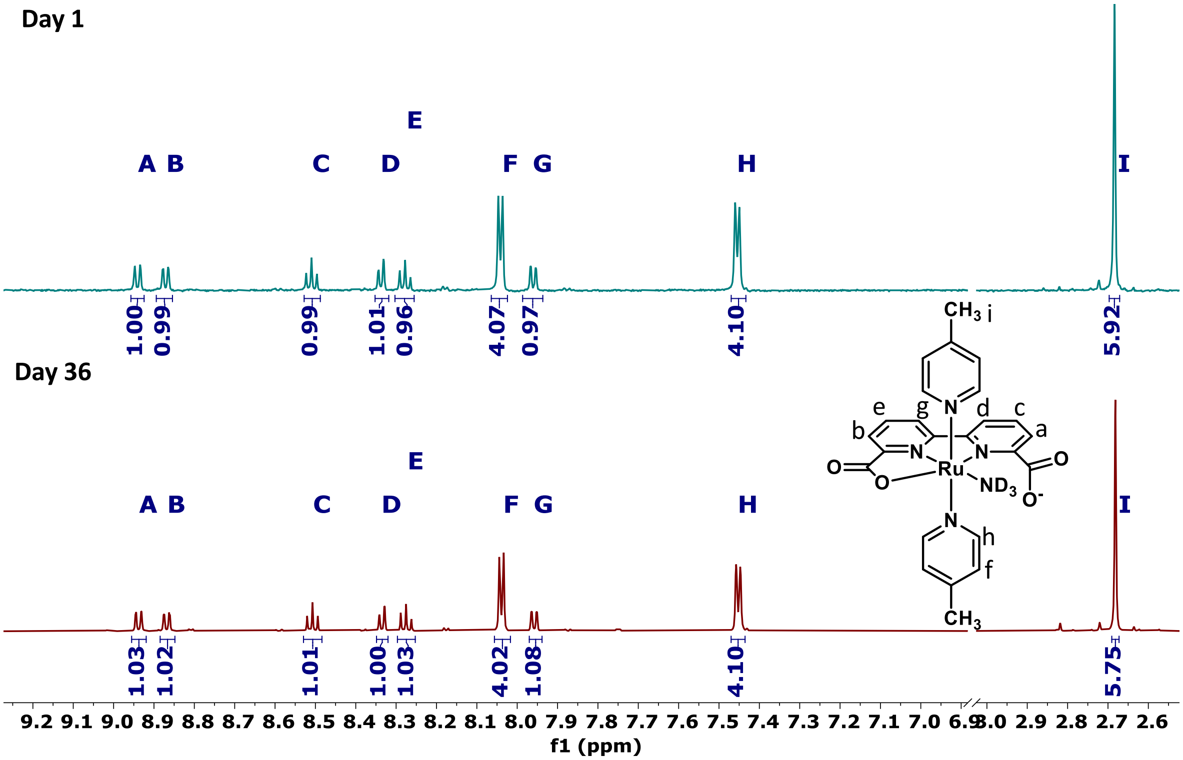

Figure 4.16. ^{1}H NMR spectra of **4.1** (3.78 μmol) in 750 μL of ND_4OD (25-30% ND_3). Top spectrum was taken immediately after dissolving the complex. Bottom spectrum was taken after 36 days of the solution allowed to sit without disturbance. The ratio of ND_3 to **4.1** is approximately 2900:1.

that all the pyridyl ligands remained coordinated to the ruthenium despite prolonged dissolution with ~2900 equivalents of ammonia.

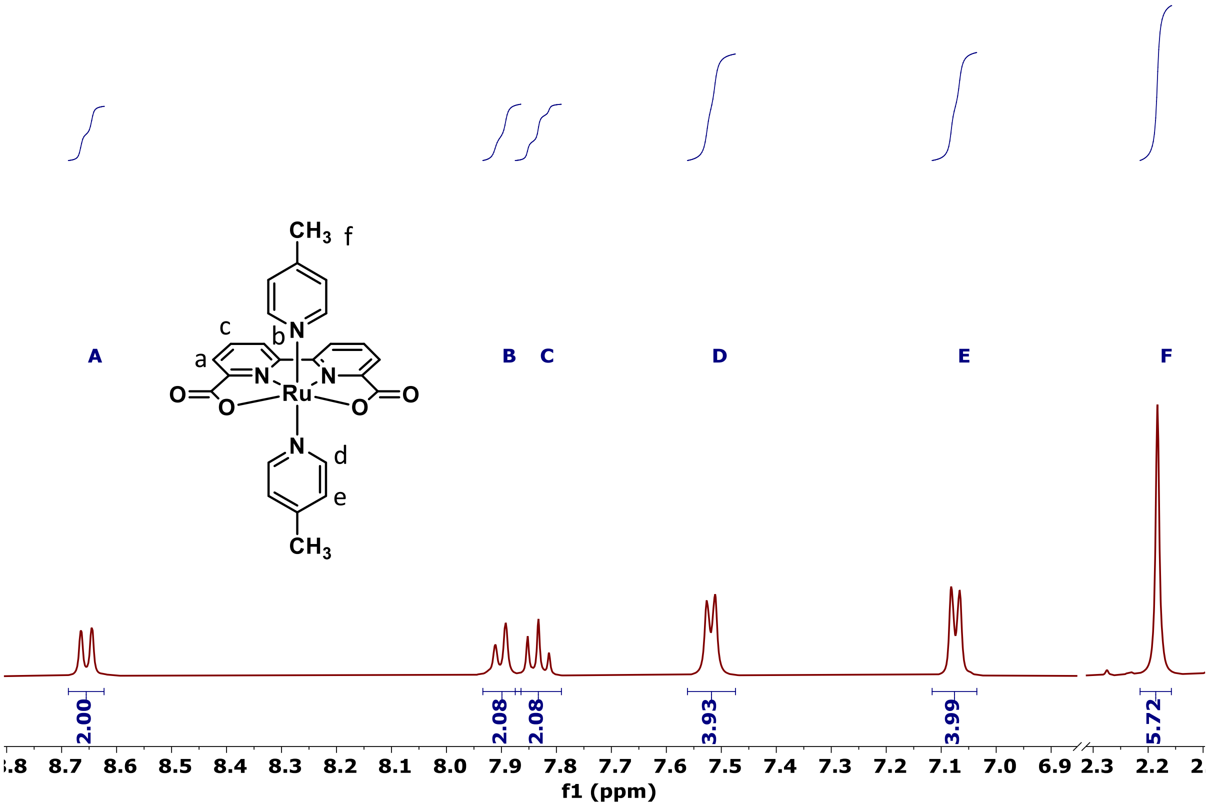

Figure 4.17. ^{1}H NMR spectra of **4.1** in d-DMSO.

4.3 Summary:

In summary, we report the first molecular electrocatalyst for NER under aqueous conditions to achieve high faradaic efficiencies (>84%) and a TON > 1. Important characteristics of other NER molecular electrocatalysts are provided in Table 4.2 for comparison. Complex **4.1** exhibits the highest TOF to be reported for a NER electrocatalyst and displays impressive stability in realistic commercial concentrations of NH_3 without any indication of decomposition. Our kinetic analyses suggest that the catalyst operates via an ANA mechanism which is highly applicable for commercially viable fuel cells as it can likely be attached to an electrode surface without reducing its catalytic activity. The catalyst's overpotential, however, is still not viable for an applicable fuel cell. Our lab is currently working on modifying the bipyridine ligand framework to lower the overpotential as well as studying its reactivity while attached to a conductive surface.

Table 4.2. Comparison of reported molecular NER catalysts.[a]

Catalyst	**Solvent**	**E_{onset} (V)**	**E_{app} (V)[b]**	**FE N_2 (%)**	**TON**	**TOF or k_{obs}**	**Eq NH_3**
4.1	Water pH 10	0.497	0.530	84	10	4130 s^{-1} [c]	14300
			0.685	94	8.2		
RuBdaIsoq	MeCN	0.83	-	-	14	0.5 s^{-1} [c]	30
RuTerpBipy	THF	0.56	0.73	90	2	-	125
Fe(TPA)	MeCN	1.33	1.65	93	9.6	10^7 M^{-1} s^{-1} [d]	130
Fe(bpyPy$_2$Me)	MeCN	1.08	1.48	84	149	1.8×10^9 M^{-1} s^{-1} [d]	400
RuTdaPyr	water	1.15	1.20	30-45	1	-	2000
	MeCN	1.15	1.40	74	7.5		500
MnSalen	MeCN	1.29	1.49	96	6.6	-	50
$Ru_2(chp)_4$	MeCN	0.375	0.63	52	5	5.63×10^{-4} s^{-1} [e]	1070

[a] All potentials are referenced to NHE. Potentials originally reported against Fc in MeCN and THF were converted to NHE by adding 0.63 and 0.53 V respectively. [b] Potentials applied for CPC. The thermodynamic potentials for NH_3 oxidation to N_2 in MeCN, THF, and water pH 10 are -0.309 V, -0.280 V, and -0.498 V vs. NHE respectively. [c] Calculated from plateau currents independent of the scan rate. [d] Calculated from a FOWA. [e] Calculated from UV-Vis experiment.

4.4 Appendix:

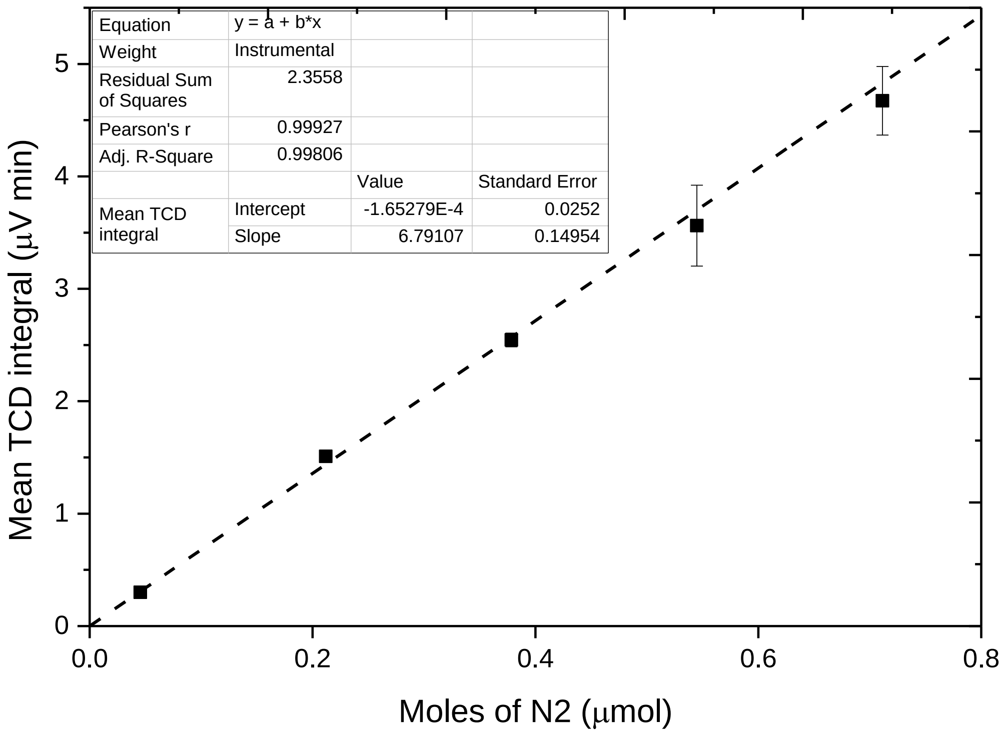

Figure 4.18. Calibration curve for quantification of N_2 gas made by direct injections of N_2 gas.

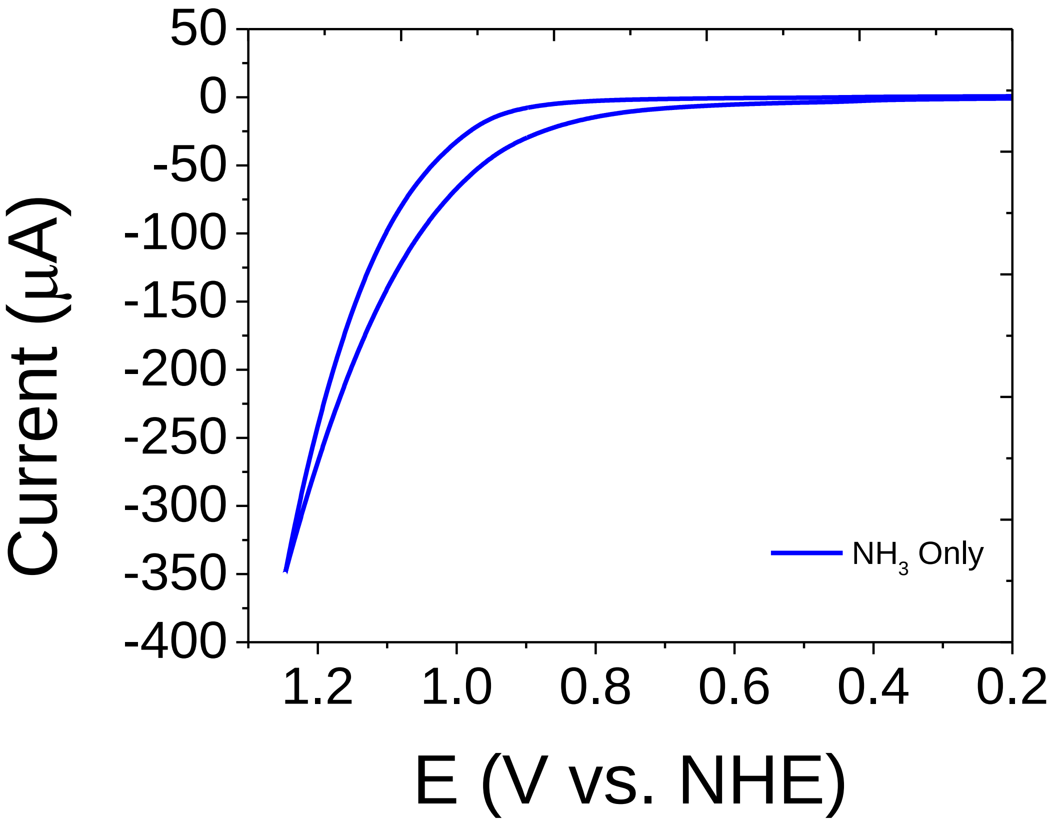

Figure 4.19. CV of NH_3 (14.3 M) in water with NH_4OTf (1 M) and NaOTf (0.1 M) as supporting electrolyte. Glassy carbon working, Pt counter, and saturated KCl calomel reference electrodes.

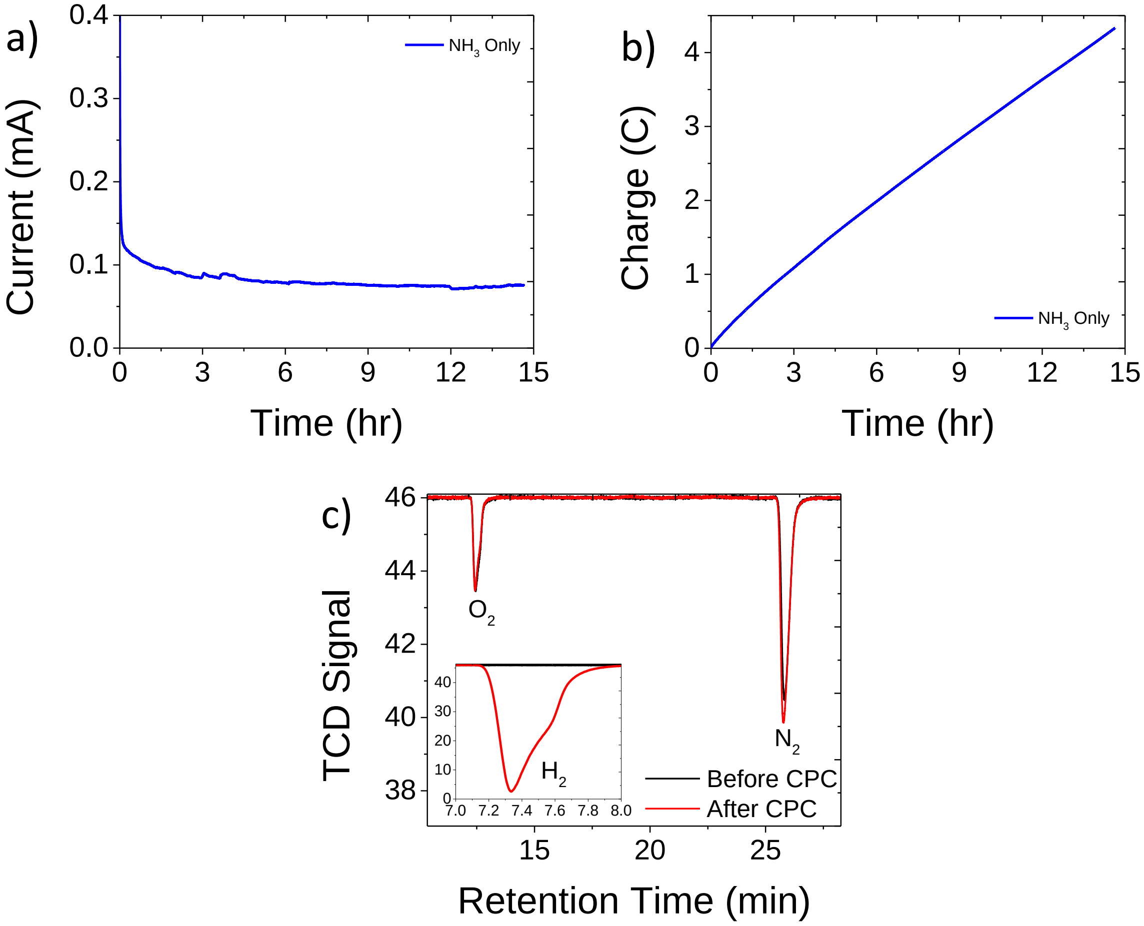

Figure 4.20. CPC data corresponding to an 878-minute control experiment with an applied potential of 0.685 V vs. NHE with NH_3 (14.3 M), NH_4OTf (1 M), and NaOTf (0.1 M) as supporting electrolyte in water. (a) Charge vs time, (b) current vs. time, (c) TCD signal from injection of 100 μL of headspace from the electrolysis cell before (black trace) and after (red trace) CPC.

4.5 Experimental:

General Considerations. All manipulations were performed under an atmosphere of dry Ar or N_2 by means of standard Schlenk or glovebox techniques (MBRAUN UNIlab Pro SP Eco equipped with a −40 °C freezer), unless stated otherwise. Ammonium trifluoromethane sulfonate was purchased from Fisher and was dried under heat and vacuum prior to transferring to the glovebox. Aqueous ammonia solution with pH=12 was purchased from Fisher. The solution was titrated and the $[NH_3]$ = 14.3 M. Deuterated solvents were purchased from Cambridge Isotope Laboratories and stored over 4 Å molecular sieves for at least 2 days prior to use except for the deuterated ammonia solution. Compound **4.1** was prepared according to literature procedure[34].

Spectroscopic Measurements. NMR spectra were obtained on Agilent Technologies 600 MHz spectrometers and referenced to residual solvent or externally. Chemical shifts (δ) are recorded in ppm, and the coupling constants are in Hz.

Electrochemical Measurements. All electrochemical experiments were performed on a CH Instruments 630E electrochemical analysis potentiostat. Cyclic voltammetry experiments were carried out with a 3 mm diameter glassy carbon working electrode, a saturated KCl Calomel Electrode (SCE), and a Pt wire counter electrode in a conventional three-electrode cell. We noted that degassing solutions did not affect the reactions at the working electrode, therefore CV measurements were done in open air. DI water (MilliQ) and aqueous ammonia (14.3 M, pH 12) were used as the solvent for electrochemical measurements with [Na][OTf] (0.1 M) as the supporting electrolyte. The glassy carbon working electrode was polished before each measurement using diamond slurry pads (3 μm, 1 μm, 0.25 μm and 0.05 μm, Buehler MetaDiTM Supreme) on polishing pads (Buehler MasterTex) for at least 2 minutes, followed by sonication in DI water (MilliQ) for ~ 10 s, and air-dried. The potential of the SCE reference electrode was referenced to the potassium ferricyanide Fe^{III}/Fe^{II} redox couple (0.36 V vs. NHE) prior to each experiment.

Controlled Potential Coulemetry. For controlled potential coulomentry experiments a glassy carbon rod working electrode, a large surface platinum wire coil counter electrode, and a saturated KCL SCE reference electrode were used. CPC experiments were done in a custom-made glass cell with sampling port plugged with a suba-seal during measurements. To the cell was added **4.1** (2.1 mg, 1 mM) and 4 mL of aqueous solution containing NH_3 (14.3 M), NaOTf (0.1 M), NH_4OTf (1 M). The headspace volume after addition of liquid was 10 mL. The cell was sealed and degassed briefly with argon to remove air. The headspace of the cell sampled with a gas tight syring prior to each electrolysis which was injected in the GC-TCD to confirm the absence of air. Each electrolysis was ran for varied times and stopped after 20-30 Coulombs of charge passed. Charges larger than 30 C typically showed signs of leakage due to the increased pressure build up. After each electrolysis was finished, the cell was sampled three times to ensure reliability of results.

GC-TCD. Headspace samplings of electrolysis reactions were done with a gastight syringe and analyzed using an Agilent 6890N GC with a CP Molsieve 5Å column (50 m long, 0.53 mm OD) equipped with a TCD detector to qualitatively test for H_2 and N_2 formation from these reactions. High purity argon (99.998%) from Praxair was used as the eluent. Method parameters used for the GC-TCD runs are below.

Parameter	**Value**
Inlet mode	Splitless
Inlet pressure	0.387 bar
Inlet temperature	225°C
Inlet flow rate	31.6 mL/min
Inlet purge flow	20 mL/min@0.5min
Column mode	Constant flow
Column flow rate	9.5 mL/min
Oven temperature	35°C
Detector temperature	225°C
Makeup flow	0.5 mL/min
Column + Makeup flow	10 mL/min
Reference flow	26.4 mL/min
Detector sampling rate	20 Hz
Computer interfacing software	ChemStation Version N.05.04

100 µL of gas samples were analyzed on the GC-TCD unless otherwise mentioned. All injections were performed manually at ~ 20 µL/s to minimize carrier gas laminar flow at the inlet. The elution times for O2 (~12.3 minutes) and N2 (~25.7 minutes) were determined by injecting 20 µL samples of air into the GC-TCD. To determine the elution time of H_2, we trapped 5 µmol H_2 gas generated by electrolyzing 1 mM aqueous H2SO4 using two Pt wire electrodes in a sealed vial with a septum. We sampled the headspace (~10 mL) of this vial and analyzed it to establish the elution time of H_2 to be ~7.3 minutes. We ran samples of the electrochemical cell atmsphere on the GC-TCD to confirm the absence of leaks prior to each electrolysis. For these samples, we observe Ar from the cell atmosphere atmosphere as well as a small signal for O_2 and N_2 from air in the syringe needle and gas lock valve assembly. Air contributions we small enough to be corrected for.

4.6 References:

1. Adli, N. M.; Zhang, H.; Mukherjee, S.; Wu, G., Review—Ammonia Oxidation Electrocatalysis for Hydrogen Generation and Fuel Cells. *Journal of The Electrochemical Society* **2018,** *165* (15), J3130-J3147.
2. Service, R. F., Ammonia—a renewable fuel made from sun, air, and water—could power the globe without carbon. *Science* **2018**.
3. Jeerh, G.; Zhang, M.; Tao, S., Recent progress in ammonia fuel cells and their potential applications. *Journal of Materials Chemistry A* **2021,** *9* (2), 727-752.
4. Li, Y.; Pillai, H. S.; Wang, T.; Hwang, S.; Zhao, Y.; Qiao, Z.; Mu, Q.; Karakalos, S.; Chen, M.; Yang, J.; Su, D.; Xin, H.; Yan, Y.; Wu, G., High-performance ammonia oxidation catalysts for anion-exchange membrane direct ammonia fuel cells. *Energy & Environmental Science* **2021,** *14* (3), 1449-1460.
5. Rees, N. V.; Compton, R. G., Carbon-free energy: a review of ammonia- and hydrazine-based electrochemical fuel cells. *Energy & Environmental Science* **2011,** *4* (4).
6. Afif, A.; Radenahmad, N.; Cheok, Q.; Shams, S.; Kim, J. H.; Azad, A. K., Ammonia-fed fuel cells: a comprehensive review. *Renewable and Sustainable Energy Reviews* **2016,** *60*, 822-835.
7. Lan, R.; Tao, S., Ammonia as a Suitable Fuel for Fuel Cells. *Frontiers in Energy Research* **2014,** *2*.
8. Zhao, Y.; Setzler, B. P.; Wang, J.; Nash, J.; Wang, T.; Xu, B.; Yan, Y., An Efficient Direct Ammonia Fuel Cell for Affordable Carbon-Neutral Transportation. *Joule* **2019,** *3* (10), 2472-2484.

9. Little, D. J.; Edwards, D. O.; Smith, M. R., 3rd; Hamann, T. W., As Precious as Platinum: Iron Nitride for Electrocatalytic Oxidation of Liquid Ammonia. *ACS Appl Mater Interfaces* **2017,** *9* (19), 16228-16235.

10. Kim, H.; Yang, W.; Lee, W. H.; Han, M. H.; Moon, J.; Jeon, C.; Kim, D.; Ji, S. G.; Chae, K. H.; Lee, K.-S.; Seo, J.; Oh, H.-S.; Kim, H.; Choi, C. H., Operando Stability of Platinum Electrocatalysts in Ammonia Oxidation Reactions. *ACS Catalysis* **2020,** *10* (19), 11674-11684.

11. Little, D. J.; Smith, I. I. I. M. R.; Hamann, T. W., Electrolysis of liquid ammonia for hydrogen generation. *Energy & Environmental Science* **2015,** *8* (9), 2775-2781.

12. Candido, L.; Gomes, J. A. C. P., Evaluation of anode materials for the electro-oxidation of ammonia and ammonium ions. *Materials Chemistry and Physics* **2011,** *129* (3), 1146-1151.

13. Herron, J. A.; Ferrin, P.; Mavrikakis, M., Electrocatalytic Oxidation of Ammonia on Transition-Metal Surfaces: A First-Principles Study. *The Journal of Physical Chemistry C* **2015,** *119* (26), 14692-14701.

14. Zott, M. D.; Garrido-Barros, P.; Peters, J. C., Electrocatalytic Ammonia Oxidation Mediated by a Polypyridyl Iron Catalyst. *ACS Catalysis* **2019,** *9* (11), 10101-10108.

15. Bhattacharya, P.; Heiden, Z. M.; Chambers, G. M.; Johnson, S. I.; Bullock, R. M.; Mock, M. T., Catalytic Ammonia Oxidation to Dinitrogen by Hydrogen Atom Abstraction. *Angew Chem Int Ed Engl* **2019,** *58* (34), 11618-11624.

16. Habibzadeh, F.; Miller, S. L.; Hamann, T. W.; Smith, M. R., 3rd, Homogeneous electrocatalytic oxidation of ammonia to N2 under mild conditions. *Proc Natl Acad Sci U S A* **2019,** *116* (8), 2849-2853.

17. Nakajima, K.; Toda, H.; Sakata, K.; Nishibayashi, Y., Ruthenium-catalysed oxidative conversion of ammonia into dinitrogen. *Nat Chem* **2019,** *11* (8), 702-709.

18. Dunn, P. L.; Cook, B. J.; Johnson, S. I.; Appel, A. M.; Bullock, R. M., Oxidation of Ammonia with Molecular Complexes. *J Am Chem Soc* **2020,** *142* (42), 17845-17858.

19. Dunn, P. L.; Johnson, S. I.; Kaminsky, W.; Bullock, R. M., Diversion of Catalytic C-N Bond Formation to Catalytic Oxidation of NH3 through Modification of the Hydrogen Atom Abstractor. *J Am Chem Soc* **2020,** *142* (7), 3361-3365.

20. Zott, M. D.; Peters, J. C., Enhanced Ammonia Oxidation Catalysis by a Low-Spin Iron Complex Featuring Cis Coordination Sites. *J Am Chem Soc* **2021,** *143* (20), 7612-7616.

21. Toda, H.; Kuroki, K.; Kanega, R.; Kuriyama, S.; Nakajima, K.; Himeda, Y.; Sakata, K.; Nishibayashi, Y., Manganese-Catalyzed Ammonia Oxidation into Dinitrogen under Chemical or Electrochemical Conditions*. *Chempluschem* **2021**.

22. Holub, J.; Vereshchuk, N.; Sanchez-Baygual, F. J.; Gil-Sepulcre, M.; Benet-Buchholz, J.; Llobet, A., Synthesis, Structure, and Ammonia Oxidation Catalytic Activity of Ru-NH3 Complexes Containing Multidentate Polypyridyl Ligands. *Inorg Chem* **2021,** *60* (18), 13929-13940.

23. Pegis, M. L.; Roberts, J. A.; Wasylenko, D. J.; Mader, E. A.; Appel, A. M.; Mayer, J. M., Standard Reduction Potentials for Oxygen and Carbon Dioxide Couples in Acetonitrile and N,N-Dimethylformamide. *Inorg Chem* **2015,** *54* (24), 11883-8.

24. Pegis, M. L.; Wise, C. F.; Martin, D. J.; Mayer, J. M., Oxygen Reduction by Homogeneous Molecular Catalysts and Electrocatalysts. *Chem Rev* **2018,** *118* (5), 2340-2391.

25. Warren, J. J.; Tronic, T. A.; Mayer, J. M., Thermochemistry of proton-coupled electron transfer reagents and its implications. *Chem Rev* **2010,** *110* (12), 6961-7001.

26. Collier, A.; Wang, H.; Ziyuan, X.; Zhang, J.; Wilkinson, D., Degradation of polymer electrolyte membranes. *International Journal of Hydrogen Energy* **2006,** *31* (13), 1838-1854.

27. Cinti, G.; Discepoli, G.; Sisani, E.; Desideri, U., SOFC operating with ammonia: Stack test and system analysis. *International Journal of Hydrogen Energy* **2016,** *41* (31), 13583-13590.

28. Duan, L.; Bozoglian, F.; Mandal, S.; Stewart, B.; Privalov, T.; Llobet, A.; Sun, L., A molecular ruthenium catalyst with water-oxidation activity comparable to that of photosystem II. *Nat Chem* **2012,** *4* (5), 418-23.

29. Zhang, B.; Sun, L., Ru-bda: Unique Molecular Water-Oxidation Catalysts with Distortion Induced Open Site and Negatively Charged Ligands. *J Am Chem Soc* **2019,** *141* (14), 5565-5580.

30. Yang, J.; Wang, L.; Zhan, S.; Zou, H.; Chen, H.; Ahlquist, M. S. G.; Duan, L.; Sun, L., From Ru-bda to Ru-bds: a step forward to highly efficient molecular water oxidation electrocatalysts under acidic and neutral conditions. *Nat Commun* **2021,** *12* (1), 373.

31. Yi, J.; Zhan, S.; Chen, L.; Tian, Q.; Wang, N.; Li, J.; Xu, W.; Zhang, B.; Ahlquist, M. S. G., Electrostatic Interactions Accelerating Water Oxidation Catalysis via Intercatalyst O-O Coupling. *J Am Chem Soc* **2021,** *143* (6), 2484-2490.

32. Zhang, B.; Zhan, S.; Liu, T.; Wang, L.; Ken Inge, A.; Duan, L.; Timmer, B. J. J.; Kravchenko, O.; Li, F.; Ahlquist, M. S. G.; Sun, L., Switching O O bond formation mechanism between WNA and I2M pathways by modifying the Ru-bda backbone ligands of water-oxidation catalysts. *Journal of Energy Chemistry* **2021,** *54*, 815-821.

33. Gil-Sepulcre, M.; Lindner, J. O.; Schindler, D.; Velasco, L.; Moonshiram, D.; Rudiger, O.; DeBeer, S.; Stepanenko, V.; Solano, E.; Wurthner, F.; Llobet, A., Surface-Promoted Evolution of Ru-bda Coordination Oligomers Boosts the Efficiency of Water Oxidation Molecular Anodes. *J Am Chem Soc* **2021,** *143* (30), 11651-11661.

34. Timmer, B. J. J.; Kravchenko, O.; Zhang, B.; Liu, T.; Sun, L., Electronic Influence of the 2,2'-Bipyridine-6,6'-dicarboxylate Ligand in Ru-Based Molecular Water Oxidation Catalysts. *Inorg Chem* **2021,** *60* (2), 1202-1207.

35. Lee, K. J.; Elgrishi, N.; Kandemir, B.; Dempsey, J. L., Electrochemical and spectroscopic methods for evaluating molecular electrocatalysts. *Nature Reviews Chemistry* **2017,** *1* (5).

36. Okamura, M.; Kondo, M.; Kuga, R.; Kurashige, Y.; Yanai, T.; Hayami, S.; Praneeth, V. K.; Yoshida, M.; Yoneda, K.; Kawata, S.; Masaoka, S., A pentanuclear iron catalyst designed for water oxidation. *Nature* **2016,** *530* (7591), 465-8.

37. Rountree, E. S.; McCarthy, B. D.; Eisenhart, T. T.; Dempsey, J. L., Evaluation of homogeneous electrocatalysts by cyclic voltammetry. *Inorg Chem* **2014,** *53* (19), 9983-10002.

38. Costentin, C.; Drouet, S.; Robert, M.; Saveant, J. M., Turnover numbers, turnover frequencies, and overpotential in molecular catalysis of electrochemical reactions. Cyclic voltammetry and preparative-scale electrolysis. *J Am Chem Soc* **2012,** *134* (27), 11235-42.

39. Wang, V. C. C.; Johnson, B. A., Interpreting the Electrocatalytic Voltammetry of Homogeneous Catalysts by the Foot of the Wave Analysis and Its Wider Implications. *ACS Catalysis* **2019,** *9* (8), 7109-7123.

40. Matheu, R.; Neudeck, S.; Meyer, F.; Sala, X.; Llobet, A., Foot of the Wave Analysis for Mechanistic Elucidation and Benchmarking Applications in Molecular Water Oxidation Catalysis. *ChemSusChem* **2016,** *9* (23), 3361-3369.

41. Costentin, C.; Nocera, D. G.; Brodsky, C. N., Multielectron, multisubstrate molecular catalysis of electrochemical reactions: Formal kinetic analysis in the total catalysis regime. *Proc Natl Acad Sci U S A* **2017,** *114* (43), 11303-11308.

42. Costentin, C.; Savéant, J.-M., Multielectron, Multistep Molecular Catalysis of Electrochemical Reactions: Benchmarking of Homogeneous Catalysts. *ChemElectroChem* **2014,** *1* (7), 1226-1236.

43. Rountree, E. S.; Martin, D. J.; McCarthy, B. D.; Dempsey, J. L., Linear Free Energy Relationships in the Hydrogen Evolution Reaction: Kinetic Analysis of a Cobaloxime Catalyst. *ACS Catalysis* **2016,** *6* (5), 3326-3335.

44. Ruan, G.; Ghosh, P.; Fridman, N.; Maayan, G., A Di-Copper-Peptoid in a Noninnocent Borate Buffer as a Fast Electrocatalyst for Homogeneous Water Oxidation with Low Overpotential. *J Am Chem Soc* **2021,** *143* (28), 10614-10623.

45. Langerman, M.; Hetterscheid, D. G. H., Fast Oxygen Reduction Catalyzed by a Copper(II) Tris(2-pyridylmethyl)amine Complex through a Stepwise Mechanism. *Angew Chem Int Ed Engl* **2019,** *58* (37), 12974-12978.